Study of frequency tunability of a multiple passband Microwave Photonic Filter and its application to optoelectronic oscillators

by

Blaise Tshibangu Mbuebue

A Dissertation
Submitted to the Program in Electronic Science,
Electronics Department
In partial fulfillment of the requirements for the degree of

Ph.D. IN ELECTRONICS SCIENCE

at the

Instituto Nacional de Astrofísica, Óptica y Electrónica

January 2024

Tonantzintla, Puebla

Supervisors:

Dr. Ignacio Enrique Zaldívar Huerta (*INAOE*)

Dr. Min Won Lee (*Université Sorbonne Paris Nord*)

DEDICATION

To my lovely wife **Vanessa Tshiyoyi Kambola** and our beautiful son **Noah Mbuebue Tshibangu**.

In memory of my late dad **Moise Mbuebue Mukandila** and to my mother **Bernadette Bamue Kabasu**.

INSTITUTIONAL ACKNOWLEDGEMENTS

- Our gratitude to the INAOE and CONHACyT for the for the Ph.D. scholarship (846218).

- Our gratitude to different university laboratories that collaborate in this research and publications: laboratorio de comunicaciones ópticas (Instituto Nacional de Astrofísica, Óptica y Electrónica), laboratoire de physique des lasers (Universite Sorbonne Paris Nord), laboratorio de communicaciones (Universidad de las Americas de Puebl), laboratorio de óptica (Universidad de Guanajuato/ DICIS)

- Our thankfulness are addressed to **Dr. Ignacio Enrique Zaldívar Huerta** and **Dr. Min Won Lee** for supervising this thesis project, and to all the professors for their important contribution in our training.

- Finally, our great gratefulness is dedicated to all the INAOE community for integrating us and for all their supports.

ACKNOWLEDGEMENTS

Giving honor where honor is due, firstly I give thanks to **God** who has allowed the development of this thesis project by His grace and mercy. From age to age, let His name be praised forever.

I wish to thank my modest family, my wife Vanessa Tshiyoyi Kambola, my mother Bernadette Bamue Kabasu; my brothers and sisters Joe Mukandila Mbuebue, Mizou Mbuyi Mbuebue, Doctor Tommy Betukumesu Mbuebue, and Joujou Nseya Mbuebue; my cousins; my uncles and aunts; and my nephews and nieces. Despite the distance and years away from them, they have not stopped supporting and believing in me, their love and encouragement have been and will always be a success asset to me.

My thoughts and thanks to my mother in law Godelive Badibeni, to my lovely brothers and sister in law, Eric Kambola, Jean-Paul Kambola, Marcello Kambola and Marie-Claire Kambola for their love and support.

I am grateful to my collegues José Roberto Warnes Lora, Pedro Pancóatl Bortolotti, Rodrigo Cuevas Terrones, Itzel Sinai Castillo, for their support and remarkable contribution to this project.

Furthermore I also wish to thank my friends Edgard Tshishimbi Kanyinda, Jean Claude Muamba, Jean Paul Kashila, Enya Flores, July Mutombo, Boloko Freemay, Clo Kashila and Saint Pierre Ntumba. To the family of Jean- Fulbert and Rachelle Ituna, Elysée and Arlette Ilunga, Rene Oscar Carillo and Suhey Castillo, Enrique Pacio and Yazmin Esteban, Norberto Castillo and Lourdes Pineda, Roberto Carrazco and Cristi Cruz and Pedro,Wendy and the entire Castillo Vasquez family, for their love and support. Lastly I would like to thank my spiritual family of Iglesia Naciones. I am proud to share this success with all of you.

To all those who may not find their names in this dissertation, they deserve my gratitude for their precious help and friendship.

ABSTRACT

The area of Microwave Photonics (MWP) is considered on one aspect as the manner of using optoelectronic devices and systems to manipulate microwave systems and on the other aspect as the study of optoelectronic devices and systems that generate and process signals in the range of microwave frequencies. Among several applications from this last aspect, this work considers a simple and easy configuration of Microwave photonic filters (MPFs) and Optoelectronic oscillators (OEOs).

The MPFs are arrangements designed with the aim of carrying similar tasks to those of an electrical microwave filter within a radio frequency system, contributing supplementary advantages inherent to photonics such as low loss, high bandwidth, immunity to electromagnetic interference, reconfigurability, and tunability. Precisely, one of the goals of this thesis work is devoted to proposing alternatives of tunability for a particular bandpass MPF. In this way, the novelty of this work resides in the use and analysis of a Fabry-Perot filter to obtain in a dynamic way the tunability of microwave bandpass. Even more, another particular technique to achieve tunability is studied and implemented. In particular, a pair of Distributed Feedback (DFB) lasers, and a Semiconductor Optical Amplifier (SOA) are proposed for this goal.

The OEOs are other photonic arrangements that allow the generation of highly pure microwave signals. For our case, a particular OEO is designed by adding an optoelectronic loop to the basic configuration of the MPF previously mentioned. Like an MPF, frequency tunability for the OEOs is a topic of much interest too. Thus, this thesis work comprises a study to obtain the tunability of an OEO.

The tunability is achieved by modifying the intermodal separation ($\delta\lambda$) of the multimode source. The results from both proposal techniques are supported by a series of simulations, corroborated by values computed theoretically, and verified in an experimental way. The tunability of these MWP systems is successfully achieved. For the case of the OEO, this work presents for the first time, to our knowledge, a gradual tuning map demonstrating the system tunability. An analytical method to determine the phase noise (PN) is presented in order to evaluate the performance of the OEO. Compared to the theory, the obtained PN values show a good performance of our implemented OEO.

GLOSSARY

AR	Antireflection
CAD	Computer Assisted Design
Cir	Optical Circulator
CW	Continuous Wave
DDS	Direct Digital Synthesizer
DFB	Distributive Feedback
DSF	Dispersion Shifted Fibre
EDFA	Erbium-Doped Fibre Amplifier
ER	Extended Range
ESA	Electrical Spectrum Analyzer
FBC	Feedback Controller
FP	Fabry-Perot
FPF	Fabry-Perot Filter
FPOF	Fabry-Perot Optical Filter
FP-LD	Fabry-Perot Laser Diode
FSR	Free Spectral Range
FTTx	Fibre To The x
FWHM	Full-Width at Half-Maximum
FWM	Four Wave Mixing
GPIB	General-Purpose Instrumentation Bus
HDTV	High-Definition Television
ISO	Optical isolator
LR	Long Range
MLD	Multimode Laser Diode
MMF	Multimode Fibre
MPF	Microwave Photonic Filter

MSG	Microwave Signal Generator
MW	Microwave
MWP	Microwave Photonic
MZ-IM	Mach-Zehnder Intensity Modulator
OC	Optical Coupler
OEO	Optoelectronic Oscillator
OF	Optical Fibre
OSA	Optical Spectrum Analyzer
PC	Polarization Controler
PD	Photodetector
PMD	Polarization Mode Dispersion
PN	Phase Noise
POL	Passive Optical LAN
PS	Power Splitter
RBW	Resolution Bandwidth
RF	Radio Frequency
SM-SF	Single Mode-Standard Fibre
SNR	Signal-to-Noise-Ratio
SOA	Semiconductor Optical Amplifier
SR	Short Range
TFPF	Tunable Fabry-Perot Optical Filter
TLS	Tunable Laser Source
VOD	Voltage-Controlled Oscillator

INDEX

CHAPTER 1: GENERAL INTRODUCTION

1.1 Introduction and motivation

The world fascinated by technological advances in all fields, has been amazed by the information and telecommunication developments, known as the Digital or Third Industrial Revolution (Industry 3.0) and Fourth Industrial Revolution (Industry 4.0) [1-3]. Since the advent of Industry 4.0 in 2013, and the implementation of the 5G network in 2017 with its multiple applications nowadays (high-speed mobile network, entertainment and multimedia, internet of things, satellite internet…) [4,5], several essential processes such as amplification, filtering, modulation, demodulation, radio frequency (RF) signal generation, etc. are the subject of great research to improve the efficiency and the performance of communication systems. Moreover, according to the ephemeris that the world experienced due to the pandemic crisis of COVID-19, the high demand for bandwidth, and fast and reliable telecommunication platforms; has impacted the needs of all layers of the current society, and of course that will be for the future.

However, in the telecommunication field, the performances are limited by traditional RF components such as amplifiers and filters. Figure 1.1 shows an illustrative diagram of a traditional RF system where the information signal is processed in the electrical domain through electrical circuits. They present narrow bandwidth, low operating frequency, electromagnetic interferences, and difficulties in tuneability and reconfigurability [6]. There are various solutions to these limitations. For example, Microwave photonic filters (MPFs) have been developed for fast filtering effect. They can also be used for implementing optoelectronic oscillators (OEOs) [7-12]. Nevertheless, having the ability to control or tune the passband window and the Free Spectral Range (FSR) of filters, or the centre frequency of the signal generated by an oscillator, according to the need, the satisfaction of end users remains an asset [13,14].

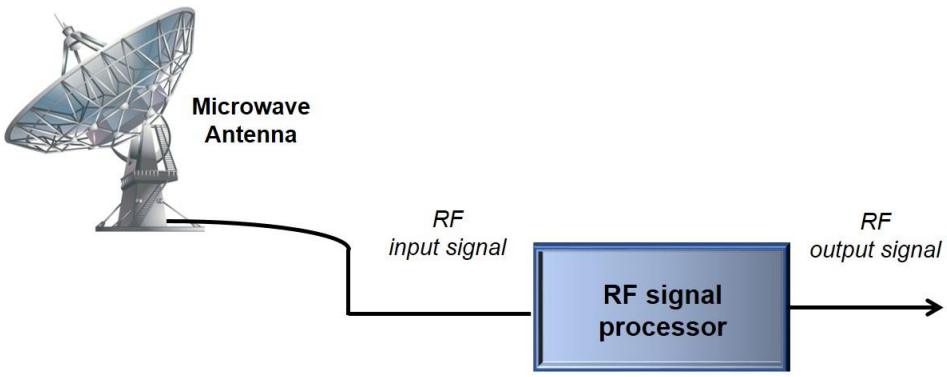

Figure 1.1 Schematic diagram of the RF signal process with RF circuits.

In Fig. 1.1, with traditional technology, RF signals received from the antenna are processed and delivered in the electrical domain by RF circuits. On the other hand, photonics technology can provide tremendous advantages such as very large bandwidth, high speed, immunity to electromagnetic interference, ultra-low losses, etc. [15]. Thus, high-frequency and broadband RF signals can be directly processed in the optical domain and converted back to the electrical domain before being delivered using an optical receiver [16]. Figure 1.2 shows an example of optical signal processing with RF signals using photonics technology.

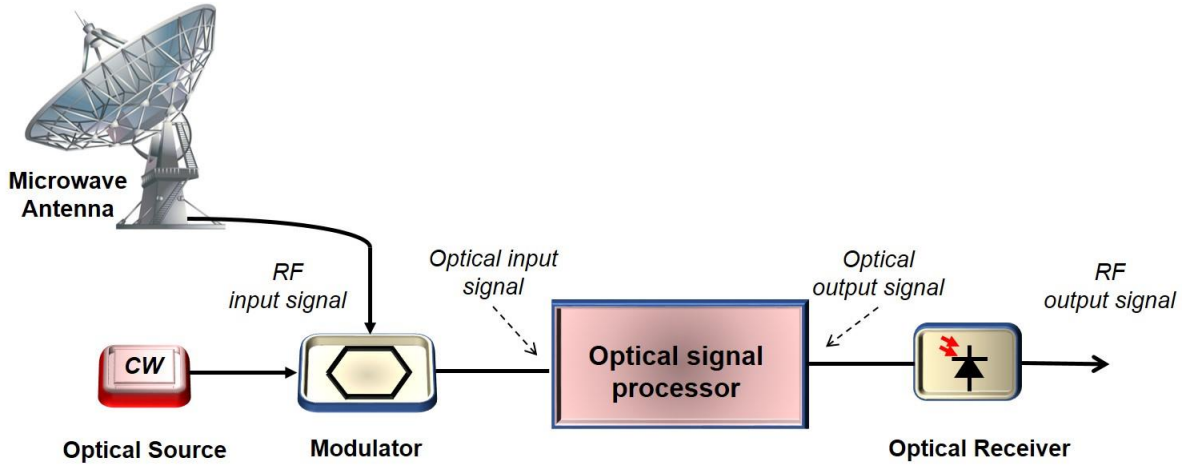

Figure 1.2 Schematic diagram of the RF signal process with an MPF.

Particularly, in the field of telecommunications, photonics technology has provided high-quality transmission of data, audio, and video signals [17]. Moreover, photonics technology allows optical networking through the Fibre To The x (FTTx) architecture [18]. This collective term FTTx is employed for different topologies of optical fibre (OF) in signal delivery. It refers to all possible

topologies of FOs used by telecom operators to transmit information from a designated point to the customer's point. Due to their tremendous advantages, FOs are used for long-distance delivery over traditional copper cabling. The FTTx is categorized according to where the optical fibre terminates and has different meanings such as:

- FTTA (Fibre-to-the-Antenna): the fibre connects a base station located at a remote radio-head (RRH) to a remote tower's RF antenna;
- FTTB (Fibre-to-the-building, -business, or -basement): the fibre reaches the boundary of the building;
- FTTC/ FTTK (Fibre-to-the-curb/kerb, -closet, or -cabinet): this topology is similar to FTTN; however, the street cabinet or pole is closer (typically 300 m) to the user's premises;

- FTTH (Fibre-to-the-home): the fibre reaches the living space, such as a box on the outside wall of a home;
- FTTN / FTTLA (Fibre-to-the-node, - neighbourhood, or -last-amplifier): the fibre link is terminated in a street cabinet, perhaps far away (kilometres) to the customer premises, with the final connections being copper;
- FTTO (Fibre-to-the-office): the fibre connection is done from the main computer room or core switch to the user's workstation mini-switch (called FTTO Switch) that provides Ethernet services to end-user devices via standard twisted pair patch cords; etc.

Optical networks allow quick data transfer within small areas (POL: Passive Optical LAN) or over long distances (Optical/WAN). Figure 1.3 shows an illustration of a generic FTTx network with length scale delimitation.

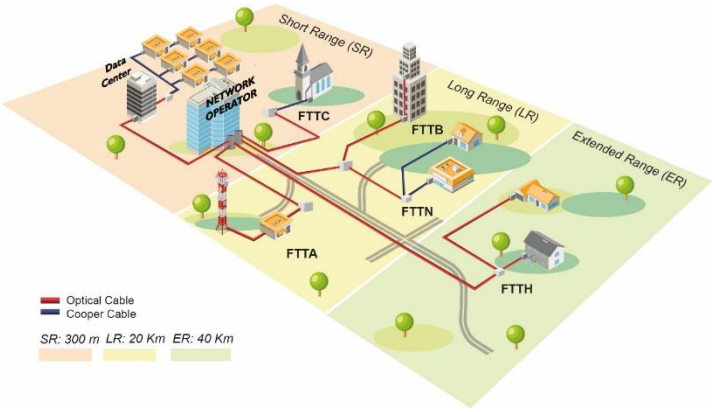

Figure 1.3 Illustration of length scale areas into the FTTx network.

At less than 300 m of length scale, the network performs Short Range (SR) communications. Whereas, when services reach length scales of 20 km and 40 km, the network carries out Long Range (LR) and Extended Range (ER) communications, respectively [19].

The more the number of users on data transmission, the narrower bands, leading to enlarging total signal bandwidth. In such networking schemes, MPFs may play an important role in high-speed communications and a high amount of data transmission. The tuneability of MPFs is a key factor in order to tune a narrow band from a large signal bandwidth.

In this work, we are going to show tuneable microwave photonic systems (MPFs and OEOs) with abilities to operate in a Long Range and Extended Range of optical communications. These promising systems are coveted in this area of technology thanks to the variety of essential applications that they provide. With capabilities of dynamic tuning and reconfigurability, OEOs and MPFs may provide applications in specialized areas such as radar, fibre-radio, radio astronomy, data transmission, analogue and high-definition TV transmission, photonic sensors, etc. [20,21].

1.2 Objectives

- *General objective:*

  In this thesis work, we are going to demonstrate a simple and dynamic multiple bandpass microwave photonic filter with frequency tuneable capabilities, as well as, a tuneable optoelectronic oscillator.

- *Particular objectives:*

  In order to achieve the general objective, we have set two specific objectives:

  - To modify the intermodal separation parameter of the multimode optical spectrum of laser sources;
  - To demonstrate the dynamic tuning of the microwave photonic filter and the optoelectronic oscillator.

1.3 Hypothesis

There already exist studies on the demonstration of tuneable photonic filters and optoelectronic oscillators. Further, details on these studies will be discussed later in the state-of-the-art section. From the results presented in these researches, some studies need physical replacement of key devices to achieve tuneability which is practically difficult to accomplish on implemented FTTx networks.

The proposal in this thesis work focuses on novel techniques that allow modifying dynamically, the optical source parameters for tuning the response frequencies of the multiple passband MPF and the OEO. Figure 1.4 presents a diagram of the principle of the system that has to be implemented to solve the mentioned issues.

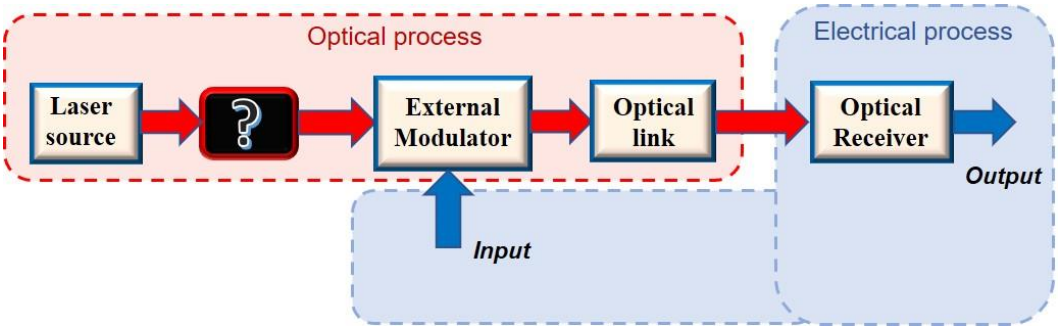

Figure 1.4 Principle diagram of the proposal study.

The block filled in black (?) represents a device or a set of devices that performs the modification of the optical parameters of the laser source in order to vary dynamically the frequency response of the photonic system.

1.4 Methodology

To achieve the objectives of this project, it is very important to understand the organization and technical aspects of the work in order to guarantee the efficiency of the expected results. Figure 1.5 presents a general block diagram that represents the synthesis of the methodology adopted for the realization of this work project, worded in these terms:

- The first step of this project is dedicated to the study and acquisition of fundamental knowledge related to the tuneability of MPF and OEO as well as theories of the

functionality of devices or optical effects that can contribute to the realization of this option.

- The second step focuses on the system design, its mathematical characteristics, and its modelling. It will also focus on carrying out a series of simulations that allow finding the ideal response of the system compared to the theoretical or mathematical prediction.
- After analysis, the third step is responsible for implementing in the laboratory the preconceived system with discrete devices and interpreting the obtained results, based on the ideal one.
- As it is often said "words fly away, and writings remain," strictly based on the previous, the fourth and last step is the crowning of the project by writing a doctoral thesis, producing the conference, congress, and journal articles, and the possibility of obtaining a patent if it is possible.

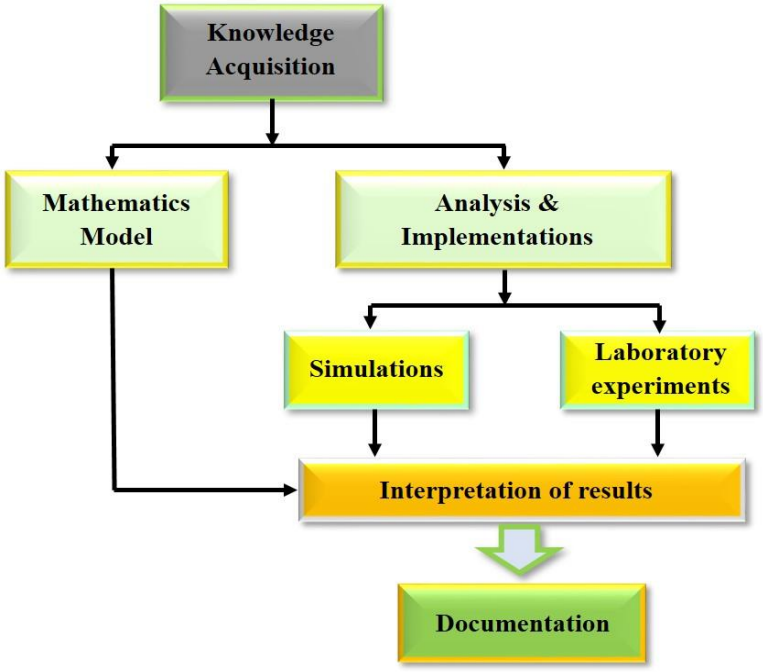

Figure 1.5 Methodology block diagram of the thesis project.

Apart from this objective methodology, the organization of the thesis work is presented in the following section.

1.5 Thesis organization

This thesis is composed of five chapters organized as follows. The first presents a general introduction that contains the motivation, objectives, problem to solve, methodology, and finally, this organization. The second explains the concept of microwave photonics and its applications for microwave photonic filters and optoelectronic oscillators. Moreover, it shows the state-of-the-art of these two applications. Then, the third presents the simulation of MPFs with tuneability capabilities and their results. The fourth shows the experimental setups and results of both implemented MPF and tuneable OEO. Finally, the fifth summarizes the main conclusions of this work and provides some ideas about future work.

CHAPTER 2: MICROWAVE PHOTONICS APPLICATIONS: MICROWAVE PHOTONIC FILTER AND OPTOELECTRONIC OSCILLATOR

2.1 Introduction

This chapter defines and presents particular applications of the Microwave Photonics (MWP) concept. Apart from this first section where the theory of conventional optical fibres is given, this part of the work has two more sections organized in the manner described below.

The second section describes and explains the basic concepts of microwave photonic filters (MPFs) and optoelectronic oscillators (OEOs). The way to achieve the tuneability of these systems is also explained.

The third section presents a brief state of the art of the MPF and OEO during the last five years and refers to the systems proposed in this thesis work.

There are two aspects that can define the area of study of MWP: (1) the manner of using optoelectronic devices and systems to manipulate microwave systems and, (2) the study of optoelectronic devices and systems that generate and process signals in the range of microwave frequencies [22]. The last definition is the one that fits in applications such as MPFs and OEOs in which microwave signals are generated, processed, controlled, and distributed [23]. However, optoelectronics is considered as a branch of both electronics and photonics. Its study concerns electronic components that emit or interact with light [24]. These components are also called photonic components and are used in electronic applications such as amplification, oscillation generation, modulation, demodulation, filtering, transmission, etc.

The MPF and OEO studied in this thesis work have another key element which is an optical fibre. Their characteristics are used for filtering effects with a length of more than 10 km. Optical fibre has received great interest and become the preferred transmission medium for communication systems [25,26]. The use of optical fibres as a medium of transmission gave birth to optical fibre communication systems.

2.1.1 Optical fibre

The Optical Fibre (OF) is a cylindrical waveguide made from a non-conductive material (dielectric) such as glass or plastic, which, has at least two different refractive indexes and transmits light as a signal [27]. Their advantages over copper wires are tremendous, particularly in terms of attenuation. Today, they replace copper wires in order to provide high-speed internet. Moreover, they are not subject to atmospheric disturbances and are immune to electromagnetic waves. According to the mode of propagation, there are two types of fibres: Single Mode Fibre (SMF) known as "conventional fibre," which allows the propagation of a single transverse mode at a time, and, Multimode Fibre (MMF) which enables several modes to propagate at a time [26,28]. Therefore, in telecommunication, for long-distance transmissions, the SMF is the one mostly used since it retains better fidelity of lights over several kilometres than MMF. Therefore, fibres refer to SMF in many cases. As seen in Fig. 2.1(a), optical fibres consist of four parts that are: (1) the core (8-10 µm) that has a refractive index n_1 and in which the light travels, (2) the cladding (125 µm) with a refractive index n_2 slightly lower than the core to facilitate the light containment, (3) the buffer (250 µm) which provides the flexibility and the mechanical protection, and (4) the jacket (900 µm) which is the protective outer coating [29]. Figure2.1 (b) presents the light propagation in an SMF. The core and cladding of the fibre are made of pure fused-silica with very low attenuation at 1550 nm.

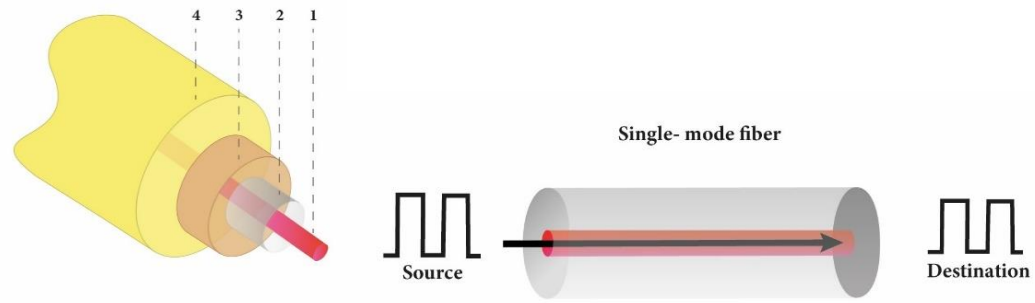

(a) (b)

Figure 2.1 Single Mode Fibre: (a) Constitution structure and, (b) light propagation.

The propagation of light is governed by Snell-Descartes law which states that an incident light ray on the interface of two media of different refractive indices n_1 and n_2, is split into two rays: a

transmitted one (or refracted) and a reflected one. Figures 2 (a) and (b) present the representative behaves of the incident and transmitted rays. The transmission ratio depends on the angle of incidence of the light ray and the refractive indices of the media expressed by [30]:

$$\frac{\sin\theta_1}{\sin\theta_2} = \frac{n_2}{n_1} \tag{2.1}$$

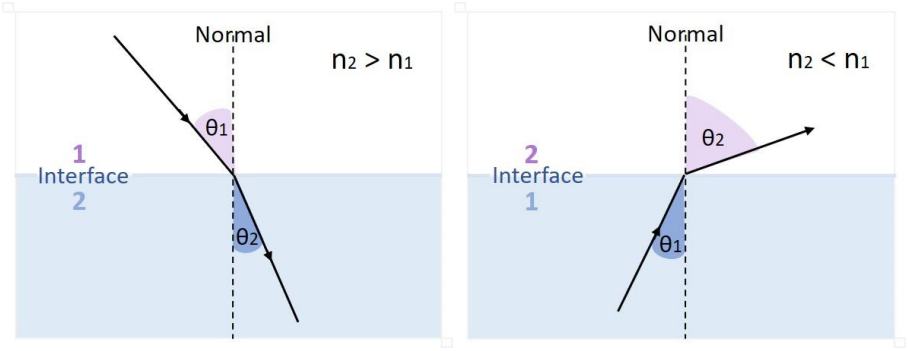

(a) (b)

Figure 2.2 Diagram of Snell-Descartes law: (a) $n_2 > n_1$, and (b) $n_2 < n_1$.

with Θ_1 and Θ_2 the incident and transmitted angles, respectively. For $n_2 < n_1$, we have $\Theta_2 > \Theta_1$; by increasing Θ_1, Θ_2 will reach 90˚ referring to the normal at the incident angle known as the critical angle Θ_c. The expression becomes $n_1 sin\theta_c = n_2 sin(\pi/2)$, which means a total reflection of the incident ray at the critical angle, and no transmitted light. Figure 2 (c) shows the diagram of this particular case.

$$\theta_c = sin^{-1}\left(\frac{n_2}{n_1}\right) \tag{2.2}$$

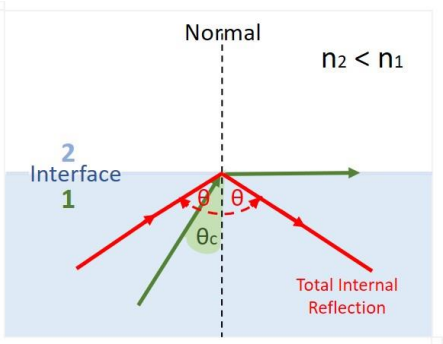

(c)

Figure 2.2 (c) Critical angle and total internal reflection.

Nowadays, the optical fibre communication medium is preferred because compared to other media like copper wire, it provides more advantages such as [31]:

- Long distance transmission: fused-silica fibres can transmit light with losses as small as 0.2 dB/km. With such a little loss, data can be sent at very long distance.

- Large information capacity: with its wider bandwidth a huge amount of information can be sent through a single physical link.

- Immunity to electrical and electromagnetic interference: The fibre is dielectric material and it does not interfere with surrounding electro-magnetic fields. Thereby it is immune to interference effects such as inductive pickup from adjacent signal-carrying wires or coupling of electrical noise from surrounding equipment.

- Small size and low weight: these characteristics provide easy handling.

- Enhanced safety: there is no worrying about ground loops, high voltage potential, or sparks, however, it is highly recommended to take precautions concerning the laser beams that can damage eyes.

- Eco-friendly: Silica which is the main material of optical fibres is abundant on Earth. It is cheap and energy-efficient in fabrication. Moreover, the signal transmission in fibre needs much less energy than that in copper wire.

In optical fibre communication, the light is used to carry the information (electronic data, long-distance telephone calls that are not conveyed by either, radio, terrestrial microwave, or satellite; analogue TV signal; digital HDMI video signal; etc.) to the end user throughout optical fibre.

Apart from these impressive characteristics and advantages such as the bandwidth, capacity, and low noise [32]. In long communication optical fibres suffer a lot, on the one hand, from linear effects such as attenuation and dispersion, and on the other hand, from nonlinear effects which are not trivial for high power and high bit rates transmission. The next points explain these uncomfortable parameters and effects within the fibre.

a) Attenuation

Usually expressed in *dB/km*, the attenuation (α) is the gradual loss of flux intensity through a medium and is responsible for the power loss of the signal. It is determined as [33]:

$$\alpha = -\frac{10}{L} log\left(\frac{P_{out}}{P_{in}}\right) \tag{2.3}$$

where L is the optical fibre length (km), P_{out} is the output optical power and P_{in} is the input optical power.

Distinctly, the attenuation is cumulative of *intrinsic mechanisms* which are due to the nature of the manufacturing material used (Ultraviolet absorption α_{uv}, Infrared absorption α_{ir}, Rayleigh Scattering α_{mono}, etc.), and *extrinsic mechanisms* which have originated from external factors to the fundamental fibre matter such as impurities into the fibre core introduced through the manufacturing process and fibre tension (Impurities absorption OH_1 and OH_2, Curve losses, etc.). Figure 2.3 shows the behaviour of the α_{TOTAL} parameter as a function of the wavelength, considering the parameters that affect it the most. Thanks to the fibre technology, today the attenuation for a typical SM-SF is less than 0.2 dB/km. As seen in this figure, the lowest attenuation is obtained as 0.18 dB/km at around 1550 nm. This is the main reason why optical telecommunications use that wavelength.

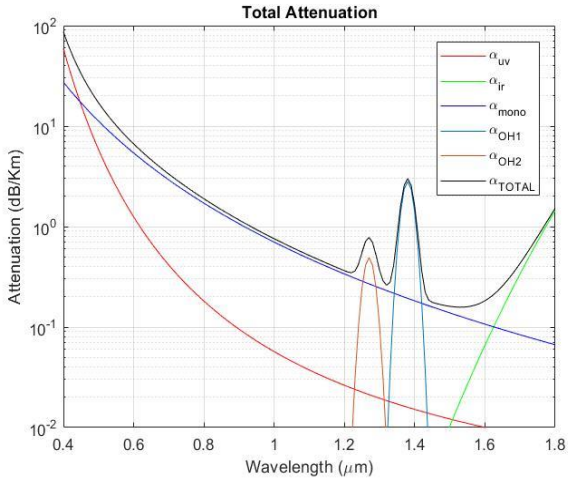

Figure 2.3 Total attenuation curve in single-mode fused-silica fibre.

b) Dispersion

The dispersion is the variation of the refractive index *n* as a function of the wavelength which is manifested by the spectrum broadening of light pulses, the difference in group velocity, and the amplitude diminution that distorts the signal.

Classified into different types: model or intermodal dispersion (appearing only in Multimode fibres), polarization mode dispersion (PMD), and chromatic dispersion; this work focuses on the latter because it is the most considered effect for long-haul communication systems. The chromatic dispersion originates from the wavelength dependence of the refractive index and is the sum of the material dispersion: $n = n(\lambda)$, and the waveguide dispersion: $n_1 \approx n_2$ [34]. Figures 2.4 (a) and (b) present the total dispersion constitution and its effect on signal propagation, respectively. For a light pulse with multiple wavelengths traveling through a material, it is stated that the longer wavelength typically moves faster than shorter wavelengths because of the wavelength-dependence of the group velocity.

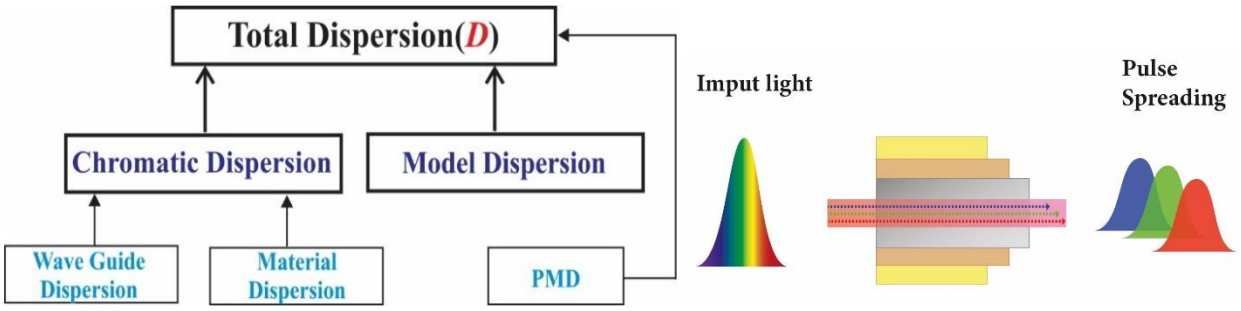

(a) (b)

Figure 2.4 (a) Total dispersion constitution; (b) Representation of the chromatic dispersion effect on light propagating into an optical fibre.

Material dispersion D_{mat} and waveguide dispersion D_{wg} are interdependent, but they can be calculated separately to see the signal distortion raised by each one [34]. In principle, the dispersion is determined by the derivative of the phase delay or phase velocity (τ) of the light propagating into an optical medium, relative to another parameter such as the wavelength (λ):

$$D(\lambda) = \frac{d\tau}{d\lambda} \tag{2.4}$$

and the broadening of the optical pulse σ over a fibre of length L by:

$$\sigma = D(\lambda).L.\sigma_\lambda \tag{2.5}$$

where σ_λ is the half-power spectral width of the optical source. It is enounced that the measured group delay τ_g is expressed as:

$$\frac{\tau_g}{L} = \frac{1}{V_g} = \frac{1}{c}\frac{d\beta}{dk} = -\frac{\lambda^2}{2\pi c}\frac{d\beta}{d\lambda} \tag{2.6}$$

$$\Leftrightarrow \tau_g = \frac{L}{V_g} = \frac{L}{c}\frac{d\beta}{dk} \tag{2.7}$$

where $k = 2\pi/\lambda$ is the wavenumber, L is the distance travelled by the pulse, β is the propagation constant along the fibre axis, and V_g is the group velocity.

The dispersion affects the properties of the light pulse depending on the medium where is travelling. The phase delay in a bulk material τ_{mat} is given by:

$$\tau_{mat} = \frac{L}{c}\left(n - \lambda\frac{dn}{d\lambda} \right) \tag{2.8}$$

$$\Longrightarrow D_{mat} = \frac{-\lambda}{c}\ \frac{d^2n}{d\lambda^2} \tag{2.9}$$

Whereas, the phase velocity in a waveguide τ_{wg} is expressed by:

$$\tau_{wg} = \frac{L}{c}\ [\, n_2 + n_2\Delta\ \frac{d(Vb)}{dV}] \tag{2.10}$$

$$\Longrightarrow D_{wg} = -\frac{n_2\Delta}{c\lambda}\ [\, V\frac{d^2\,(Vb)}{dV^2}] \tag{2.11}$$

V is the normalized frequency, $b \approx \frac{\beta/k - n_2}{n_1 - n_2}$, and $\Delta = (n_1 - n_2)/n_1$

Figure 2.5 shows the refractive index of a silicon oxide (SiO_2) fibre as a function of the wavelength, obtained from Eq. (2.12), which is known as *Sellmeier's equation*. The demonstration was done at 20°C for 60 wavelengths in the interval of [0.21, 3.71] µm [35].

$$n^2 - 1 = \frac{0.6961663\lambda^2}{\lambda^2 - (0.0684043)^2} + \frac{0.4079426\lambda^2}{\lambda^2 - (0.1162414)^2} + \frac{0.8974794\lambda^2}{\lambda^2 - (9.896161)^2} \tag{2.12}$$

$$\Leftrightarrow n = \left[1 + \frac{A\lambda^2}{\lambda^2 - B^2} + \frac{C\lambda^2}{\lambda^2 - D^2} + \frac{E\lambda^2}{\lambda^2 - F^2}\right]^{\frac{1}{2}} \tag{2.13}$$

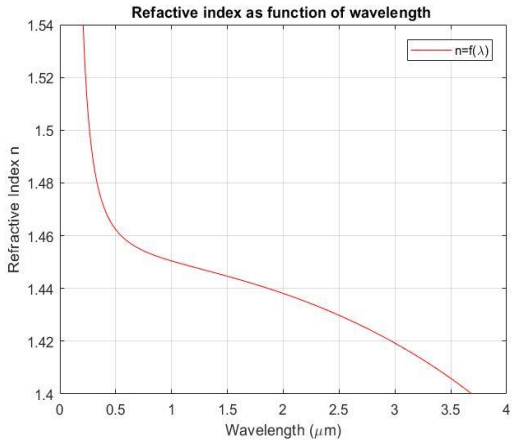

Figure 2.5 Refractive index of a SiO_2 fibre as a function of the wavelength.

For a *non-dispersion-shifted fibre (called a Class Iva fibre by the* EIA) most popular type of single-mode fibre deployed which is designed to have a *zero-dispersion* at 1270-1340 nm, the standards recommend fitting the measured group delay per unit length to the *three-term Sellmeier* equation noted as:

$$\tau = A + B\lambda^2 + C\lambda^{-3} \tag{2.14}$$

A = 0.6961663, B = 0.06844043, and C = 0.4079426 are known as the curve-fitting parameters; and D still calculated by:

$$D_{mat} = \frac{-\lambda}{c}\ \frac{d^2n}{d\lambda^2} \tag{2.15}$$

Figure 2.6 depicts both dispersion curve characteristics of a Single-Mode Standard Fibre (SM-SF), and a Dispersion Shifted Fibre (DSF) designed for zero-dispersion at around 1550 nm. The dispersion parameter D (λ) is expressed in ps/nm·km and is computed by this empiric function:

$$D(\lambda) = \frac{\lambda S_0}{4}\left[\lambda - \left(\frac{\lambda_0}{\lambda}\right)^4\right] \tag{2.16}$$

Where, λ_o is the centre wavelength and S_o is the dispersion slope, which is 0.092 ps/(nm^2·km) for standard non-dispersion-shifted fibres (or SM-SF) in the 1270 to 1340 nm region, and 0.06 to 0.08 ps /(nm^2·km) for DSF [34].

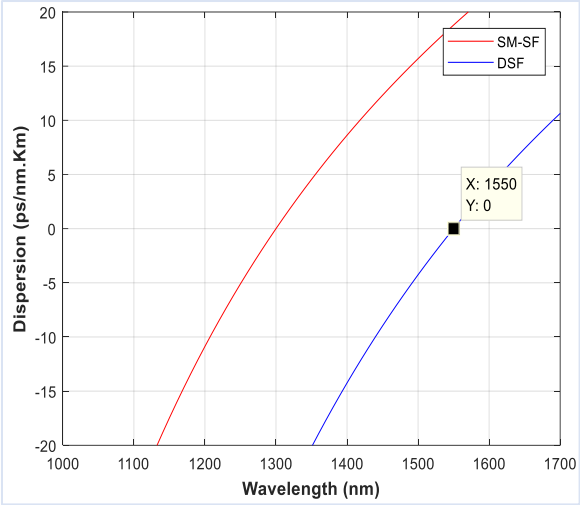

Figure 2.6 Characteristics curves of dispersion in SM-SF (red) and DSF (blue).

The dispersion can be minimized by using an SM-SF and DSF associated with a wavelength of 1300 nm and 1550 nm, respectively. For a typical SM-SF, the dispersion at 1550 nm is measured as 18 ps/nm/km. This means that if the light with wavelengths at 1550 nm and 1551 nm travels together over a distance of 100 km, the light of 1550 nm will lead the light of 1551 nm by 1.8 ns. This is the reason for which the dispersion is generally considered undesirable in long-haul communications. However, this undesirable phenomenon can be used advantageously in some applications such as microwave photonic filters (MPFs) and optoelectronic oscillators (OEOs). MPF and OEO belong to radio-frequency and optoelectronic branches, which makes them great choices in the communication domain.

c) Nonlinear effects

Deriving its name from the characteristics of the materials in which they appear like optical fibres, these effects have to be taken under consideration for light signals with high power field ($\geq$ 4 mW) and/or high bite rates ($\geq$ 10 Gb/s) [36]. In an optical fibre, the refractive index n is a relative permittivity ε_r dependent expressed as

$$n = \sqrt{\varepsilon_r} \tag{2.17}$$

For light signals with a low power field, the optical fibre acts like linear materials, ε_r is constant and the induced polarization P in the medium is determined by

$$P = \varepsilon_o(\varepsilon_r - 1)E = \varepsilon_o\chi^{(1)}E \tag{2.18}$$

which is a linear response, with ε_o = 8.854x10^{-12} F/m the permittivity of free space, $\chi^{(1)}$ the linear susceptibility, ε_r the relative permittivity, and E the applied field. For light signals with a high-power field, ε_r becomes field-dependent and the optical fibre reacts nonlinearly. By using a power series expansion in terms of E, the polarization expression becomes dependent on E, E^2, E^3, etc.

$$P = a_1E + a_2E^2 + a_3E^3 + \cdots = \varepsilon_o\left(\chi^{(1)}E + \chi^{(2)}E^2 + \chi^{(3)}E^2E + \cdots\right) \tag{2.19}$$

$\chi^{(1)}$, $\chi^{(2)}$, $\chi^{(3)}$ are the first, second, and third-order susceptibilities respectively; and a_1, a_2, a_3 are the polarization expansion coefficients. The higher-order terms of E can be neglected because their corresponding coefficient values are very small. In isotropic media such as fused-silica glasses, the coefficient a_2 is zero and, a_3 has a small finite value. Thus, Equation (2.19) becomes

$$P = a_1E + a_3E^3 = P_L + P_{NL} \tag{2.20}$$

In other words, the polarization is related to the material susceptibility of first-order χ (linear part P_L) and third-order $\chi^{(3)}$ (nonlinear part P_{NL}). Eq. (2.20) can be expressed as [37,38]

$$P = \varepsilon_o\left(\chi^{(1)}E + \frac{3}{4}\chi^{(3)}|E|^2E\right) \tag{2.21}$$

$$`P = \varepsilon_o\left(\chi^{(1)} + \frac{3}{4}\chi^{(3)}|E|^2\right)E \tag{2.22}$$

$$P = \varepsilon_o{\chi_{eff}}^{(3)}E \tag{2.23}$$

where ${\chi_{eff}}^{(3)} = \chi^{(1)} + \frac{3}{4}\chi^{(3)}|E|^2$ is the effective third-order susceptibility, and $|E|^2$ is a factor that is directly proportional to the intensity I of the electric field E applied to the material.

For some transmission systems such as wavelength-division multiplexing (WDM), the effects of nonlinearities are considerable no matter how much power injected and how much bit rate used. [39,40].

The nonlinear effects are grouped into two main categories. The effects in the first category arise from the interaction of the light with molecular vibrations (phonons) in a medium, among which the most important are the *stimulated Brillouin scattering* (SBS) and the *stimulated Raman scattering* (SRS). In these scattering effects, a light wave transfers energy to another one with low energy (longer wavelength), and the quantity of lost energy is absorbed in the matter by phonons. The light scattered by phonons is down-shifted in frequency and known as Stokes wave. For SBS and SRS, the phonons types involved in the corresponding energy transfer process are different.

In the case of SBS, the Stokes wave propagates in the backward direction of the pump wave, is down-shifted typically by around 11 GHz in an SM-SF. On the other hand, in the case of SRS, the Stokes wave is generated in both forward and backward directions and down-shifted by around 13 THz. [41].

The effects in the second category appear due to the nonlinear refractive index depending on the intensity *I* of the electric field *E* applied to the material. From Eq. (2.17) and (2.18), the refractive index is expressed as

$$n^2 = \varepsilon_r = \frac{P}{\varepsilon_o E} + 1 \tag{2.24}$$

Substituting Eq. (2.20) in Eq. (2.24), the refractive index expression becomes

$$n^2 = \frac{E(a_1 + a_3 E^2)}{\varepsilon_o E} + 1 = \left(\frac{a_1}{\varepsilon_o} + 1\right) + \left(\frac{a_3}{\varepsilon_o}\right) E^2 \tag{2.25}$$

In terms of susceptibilities the refractive index appears with linear and nonlinear parts expressed as, [16]

$$n^2 = 1 + {\chi_{eff}}^{(3)} = 1 + \chi^{(1)} + \frac{3}{4}\chi^{(3)}|E|^2 \tag{2.26}$$

The linear refractive index n_o is written as

$${n_o}^2 = 1 + \chi^{(1)} \tag{2.27}$$

Equation (2.26) becomes

$$n^2 = {n_o}^2 \left[1 + \frac{3}{4{n_o}^2}\chi^{(3)}|E|^2\right] \tag{2.28}$$

Knowing that the intensity *I* is directly proportional to the applied field $|E|^2$, with

$$I = \frac{1}{2}\varepsilon_o {n_o}^2 c|E|^2 \tag{2.29}$$

After development, the refractive index is written as

$$n = n_o + \frac{3\chi^{(3)}}{4\varepsilon_o {n_o}^2 c} I \tag{2.30}$$

$n_2 = 3\chi^{(3)}/4\varepsilon_o {n_o}^2 c$, is the nonlinear refractive index known also as the nonlinear index, with c the light velocity in the free space. This parameter quantifies the nonlinearity in a medium known as *Kerr nonlinearity* which is described as an incrementation value ($\Delta n = n_2 I$) of the refractive index proportionally to the intensity. Thus, its expression is written as [42]

$$n(I) = n_o + n_2 I \tag{2.31}$$

In this category, one of the most considered nonlinear effects is the *four-wave mixing* (FWM) [43]. For instance, considering the field E constituted by various components such as $E = E_1 + E_2 + E_3$, the nonlinear part in Eq. (2.20) can be developed as sums of different products. $E^3 = (E_1 + E_2 + E_3)^3$. After the development, the cross-product term $E_1E_2E_3$ that is proportional to cosines product $[\cos(2\pi\nu_1 t) \times \cos(2\pi\nu_2 t) \times \cos(2\pi\nu_3 t)]$, can be transformed in sums of cosines. The frequencies that correspond to $[\nu_4 = \nu_1 + \nu_2 + \nu_3]$ and $[\nu_5 = \nu_1 + \nu_2 - \nu_3]$ sums, represent the FWM.

This nonlinear effect occurs when two conditions are satisfied: energy conservation and phase matching. Generally, they are considered undesirable for communication systems. Nevertheless, they are useful in many other applications.

2.2 Basic concept of microwave photonic filter and optoelectronic oscillator

2.2.1 Microwave photonic filter

The MPF is one of the useful elements in MWP and is defined as a photonic subsystem designed to carry equivalent tasks to those of an ordinary microwave filter within an RF system or link, bringing supplementary advantages inherent to photonics such as low loss, high bandwidth, immunity to electromagnetic interference, and also providing features which are difficult or even impossible to achieve with traditional technologies, such as fast tuneability and reconfigurability [44].

Via an FTTx architecture, MPFs may be used for the distribution of services such as the internet, Video-On-Demand (VOD), High-Definition Television (HDTV), radar systems, 5G Network, etc. Figure 2.7 presents the structure of a particular MPF constituted by a continuous wave (CW) optical source, an external Mach-Zehnder modulator (MZM), an optical fibre link, and a photo-detector (PD). The MZM plays the preponderant role of controlling the amplitude of a light wave through a Mach-Zehnder interferometer made into a high electro-optic material such as a lithium niobate (LiNbO3). The light from the input waveguide is split into two interferometric arms and

then recombined at the output waveguide. When a voltage is applied to one of the arms, its optical path is modified, a phase shift is induced and that results in a phase modulation at the output.

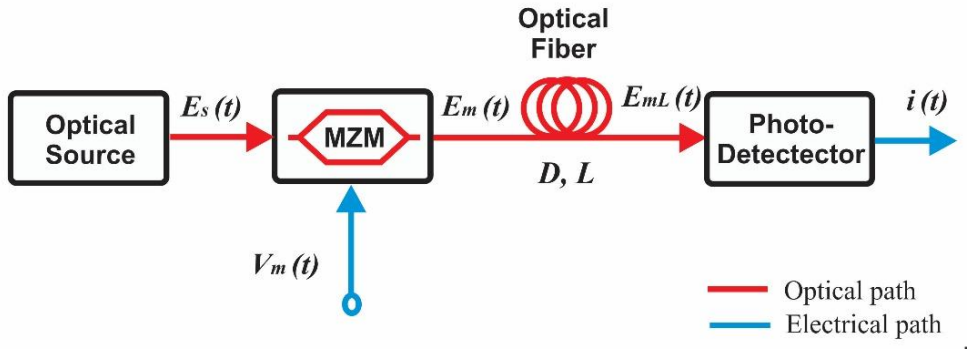

Figure 2.7 Basic structure of a microwave photonic filter.

The optical source signal $E_s(t)$ is modulated externally by the RF signal $V_m(t)$, at the output the modulator provides a modulated light-wave $E_m(t)$ which is launched through the optical fibre characterized by a dispersion parameter D and length L for being detected as $E_{mL}(t)$ and, finally recovered or converted into electrical signal $i(t)$ by the photo-detector. The MPF frequency response can be obtained in different ways such as simulations with software reproducing experiments and behaviours of devices, experimental performance measurements with a spectrum analyser, and mathematical analysis with an appropriate model and parameters. The frequency response of MPFs mainly depends on the spectral characteristics of the optical source as it is detailed and demonstrated by the mathematical model in [45].

a) MPF frequency response using a single-mode source

The normalized frequency response $C(v_m)$ of the microwave photonic filter using a monochromatic optical source is expressed as:

$$C(\mathcal{V}_m) = cos\left(\frac{\pi \mathcal{V}_m^2 \lambda^2 DL}{c}\right) \tag{2.32}$$

with v_m the frequency of the modulating signal. The graphical representation of this function is similar to the classic "notch filter," thus familiarity denomination of "Microwave Photonic notch Filter". An important characteristic of all optical fibres is that there is zero dispersion at certain wavelengths. As mentioned above, the zero dispersion for an SM-SF is located at around 1300 nm.

Thus, Eq. (2.32) becomes zero at some values of λ that correspond to frequency values denoted f_{zi}, and are determined by:

$$f_{zi} = \frac{1}{\lambda}\sqrt{\frac{1}{2}\frac{(2i-1)c}{DL}} \tag{2.33}$$

where f_{zi} is in Hz, c is in nm/s, D in ps/nm·km, λ in nm, L in km and i an integer (i = 1, 2, 3…).

Figure 2.8 exhibits an illustration of the frequency response of an MPF simulated with 15.81 ps/nm·km of dispersion parameter at 25 km, 50 km, and 150 km of optical fibre.

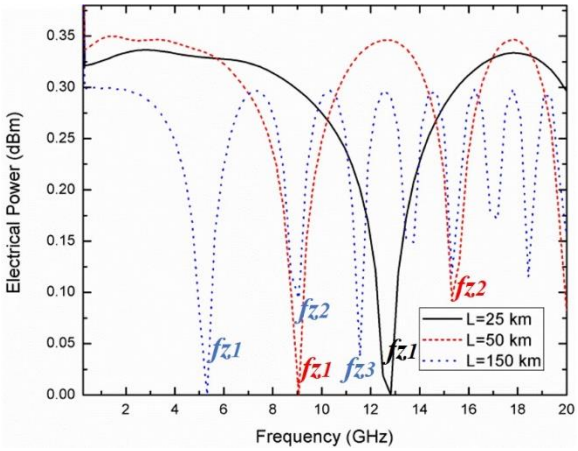

Figure 2.8 Frequency response of an MPF simulated with a single-mode source.

In summary, the use of Eq. (2.33) allows the determination of frequency values where the MW generated lobes are strangled when the length (L) of the optical link is varied.

b) MPF frequency response using a multimode source

Figure 2.9 shows an illustration of a multimode laser diode FPL1009P optical spectrum registered in the laboratory, with delimitations of the intermodal separation δλ (the separation between two successive modes) and the spectral width Δλ (Full Width at Half-Maximum, FWHM). Further, this laser is used in the experimental setup of an MPF. The inset in this Fig. 2.9 corresponds to a zoom-in of two successive modes.

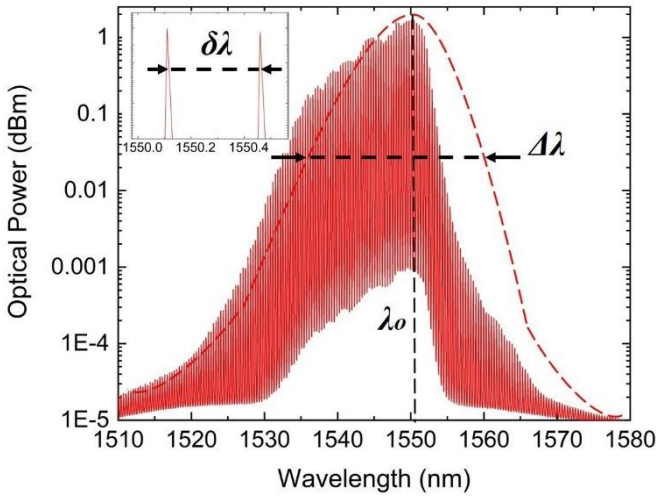

Figure 2.9 Multimode optical spectrum.

If the single-mode optical source is replaced by a multimode laser source, then the electrical response shapes band-pass windows are located at f_i.

$$f_i = i\frac{1}{DL\delta\lambda}, \tag{2.34}$$

where f_i is in Hz, D in ps/nm·km, $\delta\lambda$ in nm, L in km, and i an integer (i = 1, 2, 3…).

The bandwidth of band-pass windows denoted Δf_{bp} is determined by the envelope of Gaussian spectrum $\Delta\lambda$ (FWHM), and expressed by:

$$\Delta f_{bp} \propto C\frac{4\sqrt{ln\,2}}{\pi DL\Delta\lambda}\ \text{Hz}, \tag{2.35}$$

where C is a proportionality constant, and it can empirically be determined (like $0.5 \leq C \leq 1$).

Figure 2.10 exhibits an illustration of a frequency response of an MPF simulated showing different f_n corresponding values. The simulation was achieved with a multimode source of $\delta\lambda$ = 0.72 nm and $\Delta\lambda$ = 8.37 nm, using a standard fibre length of 25 km with a dispersion parameter of 15.81 ps/nm·km.

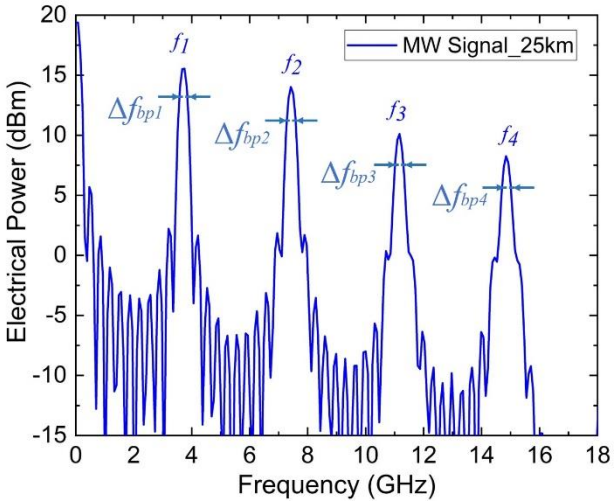

Figure 2.10 Frequency response of an MPF simulated with a multimode source.

The spectrum pattern of this electrical response is a periodic series of band-pass windows that have a centre frequency f_i and a bandwidth Δf_{bpi}.

2.2.2 Optoelectronic oscillator

The OEO is an MWP subsystem that provides a direct self-sustained microwave signal with pure spectra that have high power, low phase noises, and frequencies reaching tens of GHz. Classical technologies use devices such as a direct digital synthesizer (DDS) or a voltage-controlled oscillator (VCO) to generate multi-carrier broadband signals but are limited in performance due to the intrinsic electronic bottleneck [46]. The interesting feature of a signal generated by the OEO is that the phase noise is not affected when the frequency increases [47]. This device provides a high-frequency microwave signal with a constant phase noise achieving a high-quality factor that is independent of the frequency thanks to the low transmission loss through optical fibre [48]. These attractive characteristics present a tremendous advantage over conventional oscillators which require frequency multiplier stages to reach a few GHz [49].

Figure 2.11 shows the basic structure of an OEO constituted of a microwave photonic filter (MPF) driven by a multimode laser diode (MLD) with an electrical feedback loop [50,51].

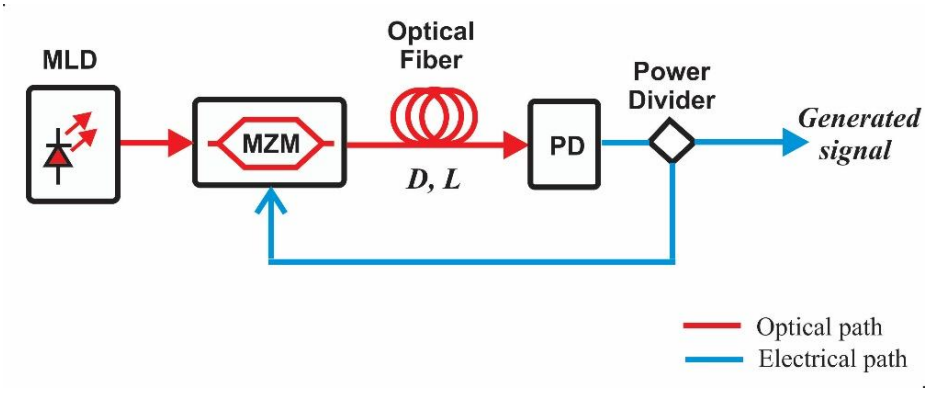

Figure 2.11 Basic structure of an optoelectronic oscillator.

In fact, the performance of the OEO depends on the MPF performances [52]. The spectrum of its electrical response is formed by microwave peaks located at the same frequencies as those determined for the bandpass windows of the MPF by Eq. (2.34). The OEO performances are evaluated by determining various elements such as the phase noise (PN), the quality factor (Q), the signal-to-noise ratio (SNR), etc. We will take a look at the first and show the process of how it is determined in this work.

2.2.3 Phase Noise measurement

Among the characteristics of an OEO, short-term stability (good phase noise) is crucial in different applications such as modern radar technology, aerospace engineering, satellite communication links, navigation systems, etc. The PN is measured using instruments such as a phase noise analyser or a spectrum analyser. Using an Electrical Spectrum Analyser (ESA), the PN value $\mathscr{L}(f)$ could be determined automatically by a PN measurement function or analytically by a traditional method known as the "spectrum analyser method". This method is described in the following lines and it is used further in this work to evaluate the performance of the OEO [53]. Figure 2.12 presents the key parameters of this method on the spectrum of a frequency peak.

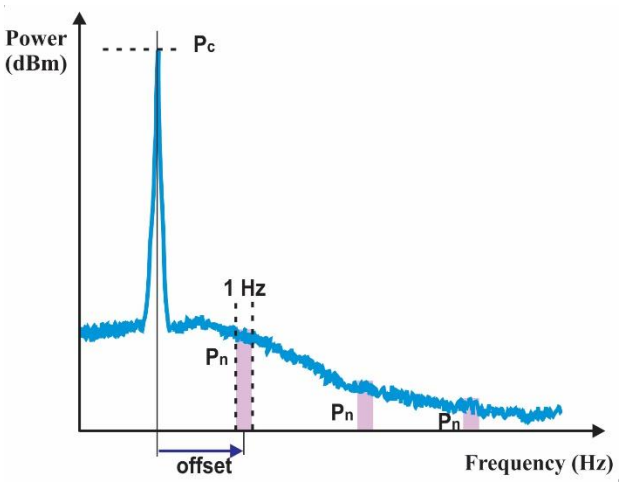

Figure 2.12 Oscillation key parameters for the spectrum analyser method.

To determine the phase noise by the spectrum analyser method a series of parameter measurements is necessary:

- To Measure the carrier power *Pc* which is the oscillation peak value in dBm.
- To Select an offset frequency (spot noise) which is a reference spot within a 1-Hz bandwidth.
- To Measure the noise power P_{offset} in dBm/Hz which is the maximum power over the 1-Hz bandwidth of a considered offset spot. In practice, many spectrum analysers cannot measure spectra with a resolution bandwidth of 1 Hz. Therefore, the noise power P_{offset} is measured with a higher resolution bandwidth and divided by the resolution bandwidth. But in the logarithmic scale like dBm/Hz, the division becomes a subtraction.
- To Compute the normalized parameter *N* in dB depending on the Resolution Bandwidth (RBW) of the analyser and determined by

  $$N = 10 \log RBW(Hz) \tag{2.36}$$

- Determine the phase noise power *Pn* in dBm/Hz which is the normalized maximum power of noise computed as

  $$P_n = P_{offset} - N \tag{2.37}$$

- Determine the phase noise $\mathscr{L}(f)$ in dBc/Hz expressed by

  $$\mathcal{L}(f) = P_n - P_c \tag{2.38}$$

E.g.: Let the carrier power be measured as 0 dBm. A spectrum analyser measures a spectrum with a resolution bandwidth of 1 kHz. Let the noise power be measured as -70 dBm at 100-kHz offset frequency. In this case, the normalized parameter *N* is obtained as 30 dB from Eq. 2.36 and the noise power *Pn* is obtained as -100 dBm/Hz from Eq. 2.37. As the carrier power is 0 dBm, the phase noise is obtained as -100 dBc/Hz.

The $\mathscr{L}(f)$ changes at different offset frequencies and generally decreases as the selected offset frequency increases. Dedicated phase noise analysers use a method known as the "cross-correlation" and generally provide greater accuracy, speed, and sensitivity than the previous method. A lower value of PN indicates a better system performance.

2.2.4 Tuneability of the microwave photonic filter and the optoelectronic oscillator

Theoretically, based on expressions of Eq. (2.34) and Eq. (2.35) the frequency response can be modified by varying various parameters. Apart from the dispersion parameter *D* which is a constant given by the manufacturer, the variation of *L* modifies both centre frequencies and bandwidth of passband, whereas the variation of $\delta\lambda$ acts on central frequencies and the variation of $\Delta\lambda$ influences the bandwidth.

Considering an optical communication system in an FTTx architecture, replacing the fibre length is not practical. The spacing mode or intermodal separation ($\delta\lambda$) remains the only way to tune centre frequencies of MPF and OEO. Therefore, if this parameter can be varied readily, tuning can be performed dynamically. These systems need a multimode emission as an optical source. In this thesis work, we are going to investigate dynamical tuning using two different methods: one using an MLD with a tuneable Fabry-Perot optical filter, and the other one using two Distributed Feedback (DFB) sources with an SOA.

a) Distributed Feedback Laser Diode

A Distributed Feedback laser (DFB laser) is a laser with one side of the resonator formed by a periodic structure acting as a distributed Bragg reflector in the active region. The other side of the cavity has a high-reflectivity material. The longitudinal grating with its periodic change of the refractive index, causes reflections of light back into the resonator cavity [54]. If these reflected light waves are any small multiple of the incident wavelength then, there is a constructive

interference of them that characterizes the operation wavelength of the device. Considering the refractive index change of n_1 and n_2, the reflected wavelength (λ_B) is computed from the Bragg condition expressed as

$$\lambda_B = 2n_{eff}\Lambda \tag{2.39}$$

where $n_{eff} = (n_1 - n_2) / (n_1 + n_2)$ is the effective refractive index, and Λ the grating period.

However, the collected modes in a DFB are not exactly λ_B but lateral wavelengths (λ_m) located symmetrically around the Bragg wavelength and computed by [40]

$$\lambda_m = \lambda_B \pm \frac{{\lambda_B}^2}{2n_{eff}L}(m+1) \tag{2.40}$$

Here, L is the effective length of the grating, and m (1, 2, 3…) is an integer representing a specific mode. For higher modes the threshold gain is larger, thus, only the mode corresponding to $m = 0$ lases as the DFB operating wavelength (λ_o). Figure 2.13 shows, as an illustration, a DFB optical spectrum registered in the laboratory.

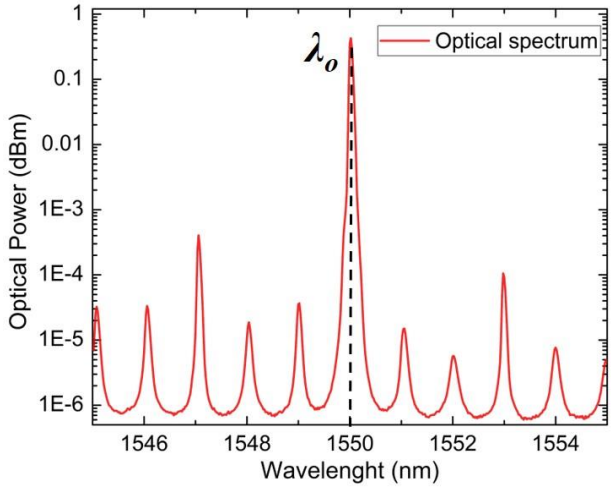

Figure 2.13 Optical spectrum of a DFB.

Technically, its wavelength peak shifts with temperature changes ($d\lambda_o/dT$) since both n_{eff} and Λ are temperature-dependent parameters. Typically, if the temperature increases by 1˚C, then the wavelength λ_o increases on the order of 0.1 nm. Thus, a temperature controller is needed to stabilize or to adjust the wavelength value. Indeed, DFB laser diode manufacturers take advantage of this

$d\lambda_o/dT$ feature to make tuneable DFBs. Further in this work, such tuneability of DFBs will be exploited for the implementation of a tuneable multimode source.

b) Multimode Laser Diode

As shown in Fig 2.9, essentially a Multimode Laser Diode (MLD) is different from a single-mode laser by its output beam. For single-mode Laser, the beam has only one mode, while there are several modes for the MLD. The radiation comes from the crystal edge and for that, it is usually denominated as an edge-emitting laser diode, commonly known as Fabry-Perot (FP) laser diode by having an FP cavity. Both facets of the laser diode serve as the mirrors where light reflections (Fresnel reflections) occur. The light sent front and back to the facets is amplified by a semiconductor gain medium into the cavity. By reducing the reflection losses of the mirrors, the efficiency of the FP cavity as well as the finesse is improved [40,55]. As mentioned for the previous device, the wavelength of a multimode laser source is also a temperature-dependent parameter ($d\lambda/dT$). In the following chapter, the multimode source associated with a tuneable Fabry-Perot filter to achieve the tuneability of an MPF is shown at the simulation level.

c) Tuneable Fabry-Perot Optical Filter

A Fabry–Perot resonator (or interferometer) is an optical cavity of refractive index n, formed by two parallel partially reflecting mirrors separated by a distance d. Optical waves are transmitted through the resonator when incoming waves interfere constructively with circulating waves inside the cavity, whereas the transmission is minimal in destructive interferences [56].

Figure 2.14 details the multiple reflections and transmissions of the light wave. Assuming the unity refractive index ($n = 1$) in all regions of the analysis, when the incident beam with energy E_0 meets the first surface *S1*, an energy portion E_0r is reflected whereas the remaining is transmitted. The transmitted energy E_0t continues its trajectory until reaching the second surface *S2*, then again, a part is reflected E_0tr and another part E_0t^2 is transmitted [57]. This cycle will continue indefinitely when considering infinitely long surfaces without losses.

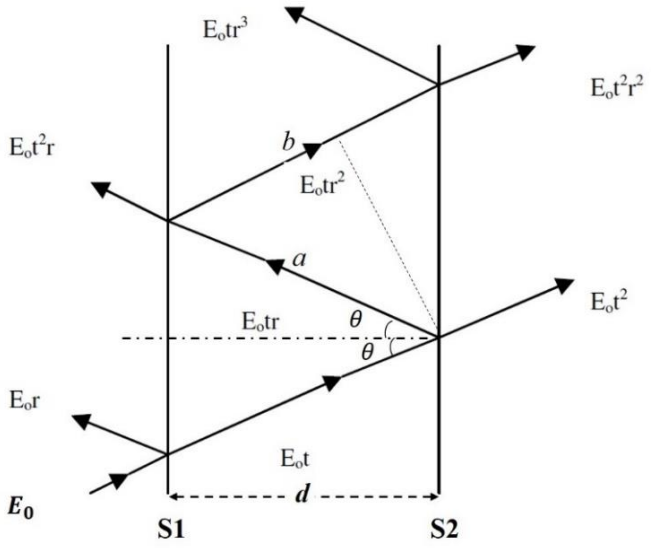

Figure 2.14 Reflections and transmissions of a Fabry-Perot resonator.

The light beam that infiltrates the FP cavity is transmitted only with wavelengths satisfying constructive interferences. The wavelengths in interferences through the cavity are written:

$$2nd\cos\theta = N\lambda \tag{2.41}$$

where N is a positive integer (N = 1, 2, 3, …), n is the refractive index, d is the cavity thickness and Θ is the radiation incident angle. This is the transmission condition of the light with a wavelength λ.

Such characteristics of the FP interferometer can be used as an optical filter. The transfer function of a Fabry-Perot Optical Filter (FPF or FPOF) has periodic peaks which are a sequence of maximum resonances that satisfy the transmission condition [58]. Figure 2.15 shows an example of an FPF transfer function.

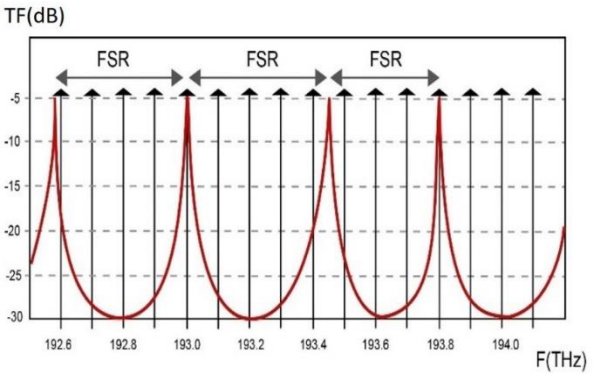

Figure 2.15 Periodic transmittance of an FPF.

The distance between two successive peaks is known as the Free Spectral Range (FSR), also called axial mode spacing. Varying the *FSR* of the FPF allows the selection of specific modes of an optical spectrum. The transfer function of the FPF in terms of optical power is given as [40]:

$$T(f) = \frac{(1-A-R)^2}{(1-R)^2+4R_s \sin^2\left(\frac{\pi f}{FSR}\right)} \tag{2.42}$$

where *A* represents the signal loss within each mirror, *R* is the optical power reflectivity, *FSR = 1/2* τ, with $\tau = nd/c$. τ is the propagation time from one cavity mirror to another, and *c* is the speed of light in the vacuum.

The FWHM of the peaks decreases when the reflectivity increases and thus, the filter becomes more selective.

$$FWHM = \frac{c}{2\pi nd} \sin^{-1}\left(\frac{1-R}{2\sqrt{R}}\right) = \frac{1}{2\pi\tau} \sin^{-1}\left(\frac{1-R}{2\sqrt{R}}\right) \tag{2.43}$$

The fineness (*F*) is the other parameter for determining the filter selectivity. A high finesse value produces sharper mode peaks.

$$F = \frac{FSR}{FWHM} = \frac{\pi}{2} \frac{1}{\sin^{-1}\left(\frac{1-R}{2\sqrt{R}}\right)} \approx \left.\frac{\pi\sqrt{R}}{1-R}\right|_{if\ R\approx 1} \tag{2.44}$$

With periodic responses in the frequency of optical filters, the tuneability of optical filters is very important in wave division multiplexing systems (WDM) and channel monitoring applications. They can handle the high demand in bitrate and number of channels in a WDM system since the filter can be tuned to various bands. The tunning can be done by varying the distance between mirrors manually and/or electro-mechanically. A lot of work has been done to demonstrate different tuneable filters based on the Fabry-Perot interferometer [59,60].

In Tuneable Fabry-Perot Optical Filters (TFPF or TFPOP) the distance between two mirrors can be varied using a piezoelectric crystal attached to the mirrors. It changes the distance by a voltage command. Piezoelectric crystals have the advantage of being controlled even by movement displacement in the order of an atom's diameter. It also provides very fast tunning.

The system illustrated in Fig. 2.16, shows a TFPF mounted on two piezo-electric crystals, using two pieces of fibres (input and output light waveguides) polished and silvered at their ends.

A voltage across the crystals varies the distance between the fibre ends, leading to modifying their resonance wavelengths. Moving physically the mirrors or perhaps changing the refractive index of the material inside the cavity also allows tuning the wavelengths of the filter. For example, liquid crystals can be introduced into the gap for tunning purposes in a TFPF. Applying a voltage to the liquid crystals will change quickly the refractive index of the liquid crystals.

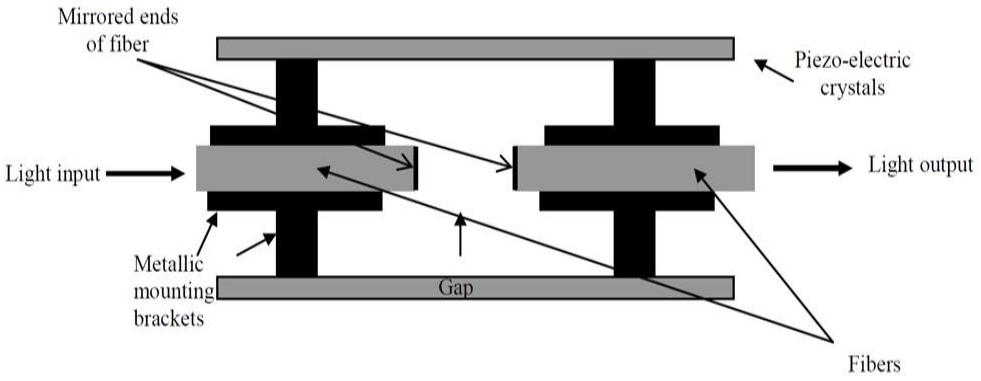

Figure 2.16 TFPF mounted on two piezoelectric crystals.

In this thesis work, the available possibility of setting the FSR of the TFPF is used at the simulation level to modify the intermodal separation $\delta\lambda$ by selecting specific modes from a multimode source.

d) Semiconductor Optical Amplifier

A Semiconductor Optical Amplifier (SOA) is a composed semiconductor device that amplifies the light travelling through, thanks to the emission stimulated by the gain medium. Similar to a laser diode, it has an optical gain medium and an optical waveguide with antireflection (AR) coatings instead of an optical cavity in laser diodes [61]. The inversion of the free carrier population in the active medium is led by pumping electrically the waveguide. By its characteristics, this device is of great interest because it can provide several functionalities such as tuneable lasers, wavelength selectors, all-optical integrated converters, all-optical switches, etc. [62,63].

Depending on the gain spectrum, there are two types of SOA: Traveling Wave SOA (TW SOA) in which light travels the gain medium once, and Fabry-Perot SOA (FP SOA) in which multiple reflections occur [62]. Further in this work, the SOA acronym refers to TW SOA and is used to implement a multimode source.

An SOA can be constructed with a laser diode on which the cavity is annihilated by minimizing the reflectivity (R = 0, for an ideal SOA) of the two facets. Considering now, two neighbouring wavelengths λ_1 and λ_2, whose respective frequencies are ν_1 and ν_2, co-propagate in an SOA in which the gain medium is nonlinear. These wave signals are subject to the FWM which is a mixing of the previous two frequencies and the effect induces the generation of lateral waves of frequencies ν_n determined as [64]:

$$\begin{cases} \nu_3 = 2\nu_1 - \nu_2 \\ \nu_4 = 2\nu_2 - \nu_1 \end{cases} \tag{2.45}$$

Figure 2.17 shows the two input waves injected into an SOA and the output emission formed by multiple modes generated thanks to the FWM.

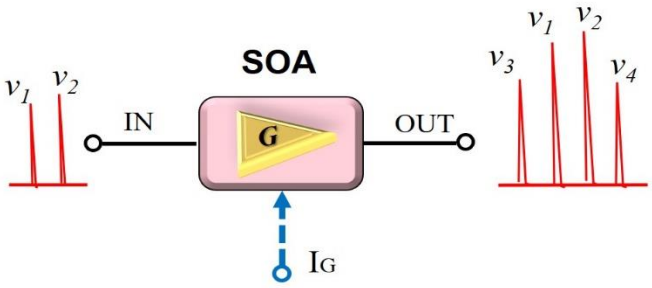

Figure 2.17 Waves generation in the SOA.

More than these two new frequencies can be generated, thus, the more the pump current (I_G) increases, the higher the gain level (G) becomes, and the more appears new frequencies (ν_n). Generally, the FWM process adds noise to the transmission of signals and has to be avoided in this kind of system. However, in this work, it is useful in the SOA for generating a multimode emission. On the other hand, by varying $\Delta\nu$, the value of $\delta\lambda$ is modified too. This results in behaviour similar to a tuneable multimode source. Further, this technique is proposed for the implementation of MW photonic systems.

2.3 State of the Art

This section refers to interesting techniques of some works among others, that oriented the research in the area of MPF and OEO tuneability, in the last five years. The first group addresses tuneable MPFs and the second is about tuneable OEOs.

- *Tuneable MPFs:*

In 2018, W. Zhang et al. demonstrated an on-chip frequency-tuneable bandpass microwave photonic filter (MPF) implemented on a silicon photonic platform [65]. Figures 2.18 (a) and (b) present respectively the experimental setup and the frequency response of the MPF. The filtering function of the MPF was realized based on the phase modulation and its conversion to intensity modulation, the Micro-Disk Resonator (MDR) translates its optical response to the frequency response of the MPF. The MPF tuneability was achieved by tuning the MDR thermally, which led to the generation of a microwave signal with 1.93 GHz of passband and tuneable from 3 GHz to 10 GHz as shown in Fig. 2.18 (b).

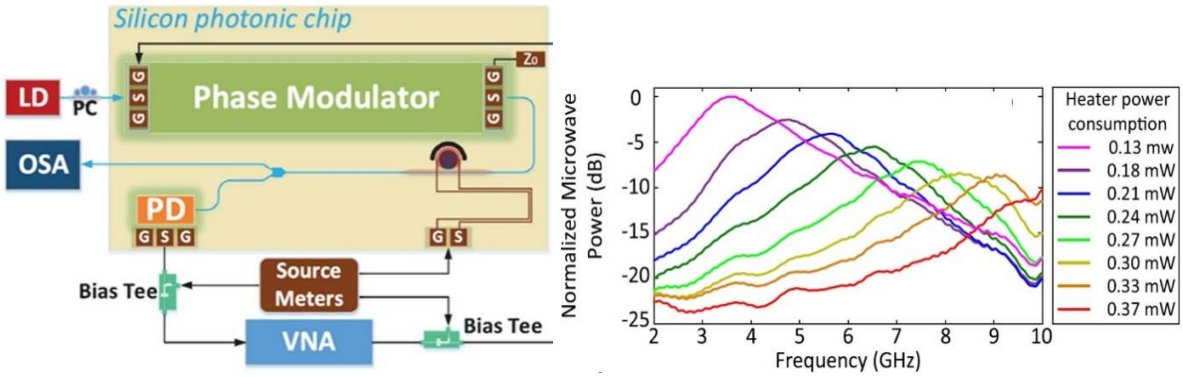

(a) (b)

Figure 2. 18 (a) Schematic of the MPF (PC: Polarisation controller, OSA: Optical Spectrum Analyser, VNA: Vectorial Network Analyser, G: Ground, S: Signal); (b) measured frequency responses of the filter with the centre frequency tuned from 3 GHz to 10 GHz (Image source: W. Zhang et al. Opt. Lett., 43, pp. 3622, 2018 [65]).

In the same year, Hua Shun et al. proposed and experimentally demonstrated an ultrahigh-Q and single passband tuneable MPF [66]. The implementation was based on the stimulated Brillouin scattering (SBS) in an optical fibre as seen in Fig. 2.19 (a). The passband is obtained with the sideband amplification of the Single-Sideband (SSB) modulated signal using SBS. By compressing the generated SBS bandwidth, the Fibre Ring Resonator (FRR) characterized by an ultra-narrow resonant linewidth, allowed the realization of the ultrahigh-Q MPF. The tuneability was achieved by adjusting the optical carrier frequency f_c and it generated a corresponding resonant

mode through the FRR. Figure 2.19 (b) shows the 3D frequency response of the MPF. It obtained a narrow single band of 825 ± 125 KHz with a wide tuneability from 2 GHz to 16 GHz.

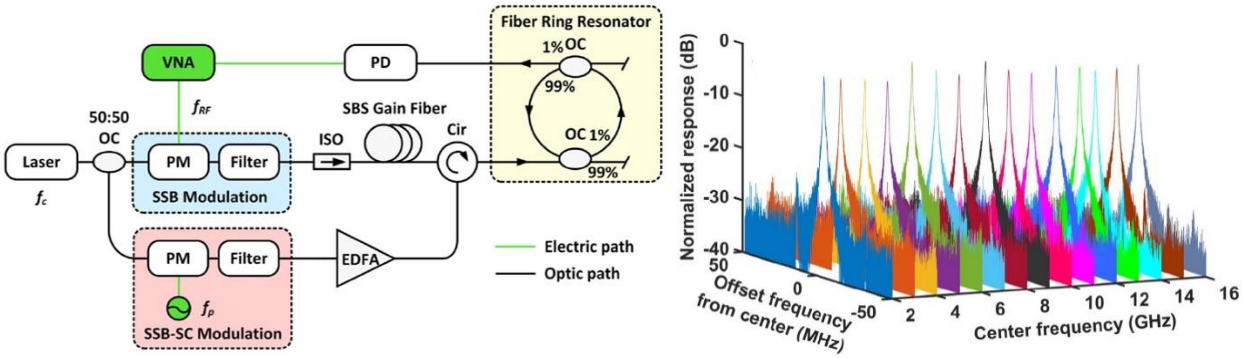

(a) (b)

Figures 2.19 (a) Setup of the ultrahigh-Q and single passband tuneable MPF (PM: Phase Modulator, OC: optical coupler, Cir: Optical Circulator, ISO: Optical isolator, EDFA: Erbium-dopped fibre amplifier), and (b) Zoomed-in view frequency response of the passbands at different centre frequencies (Image source: Hua Shun Wen et al. Opt. Lett. 43, pp. 4659, 2018 [66]).

Liang Huo et al. demonstrated an improving performance by generating multiple bandpasses of a reconfigurable MPF using Multicore Fibres (MCFs) and a Terahertz Optical Asymmetric Demultiplexer (TOAD) switch [67]. Figure 2.20 presents the implementation scheme where the TOAD is a kind of Nonlinear Optical Loop Mirror (NOLM) with a Semiconductor Optical Amplifier (SOA) inserted in the loop. The reconfigurability of the proposed two-tap MPF was validated by two different normalized amplitude-frequency responses at a high ratio of rejection.

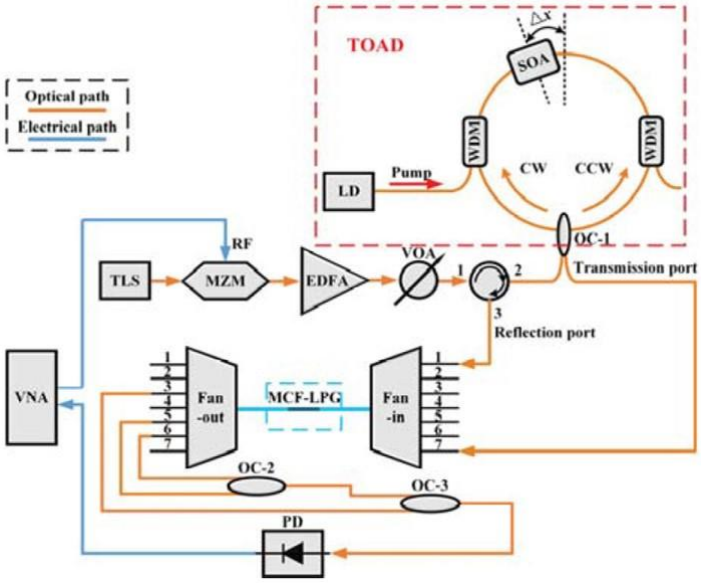

Figure 2.20 Experimental setup of a reconfigurable MPF with inserted TOAD switch (Image source: Liang Huo et al. Asia Communications and Photonics Conference 2020 [67]). VOA: Variable Optical Attenuator, LPG: Long Period Grating, TLS: Tuneable Laser Source, OC: Optical Coupler.

Without the LD pump, both clockwise (CW) and counter-clockwise (CCW) signal propagation, recombine interferometrically and are reflected through the OC. The presence of the pump signal saturates the SOA, and generates nonlinear effects that create a phase shift in these propagation paths thus, are transmitted through the OC. Figures 2.21 (a) and (b) show the obtained frequency responses of the two-tap MPF.

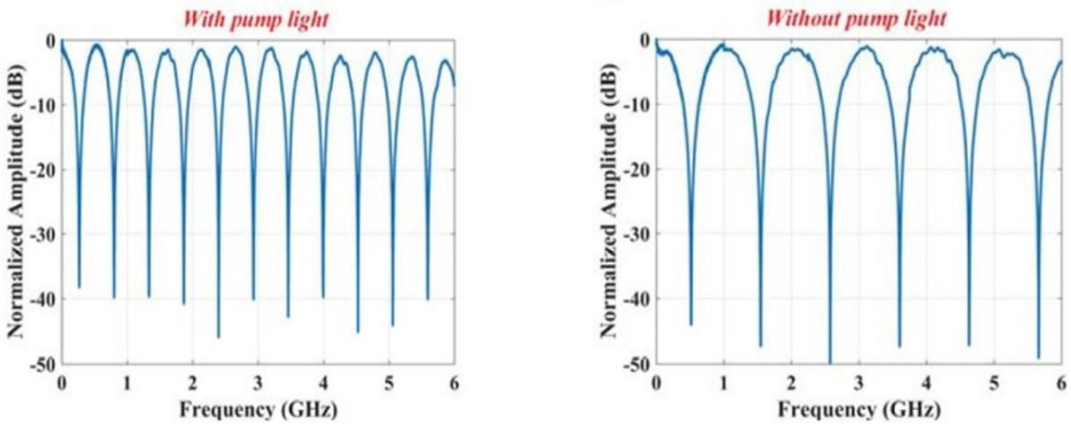

(a) (b)

Figure 2.21 Frequency responses of the MPF: (a) with the pump, (b) without the pump (Image source: Liang Huo et al. Asia Communications and Photonics Conference 2020 [67]).

In 2021, Daniel Nuño et al. presented a model of Multiwavelength (MW) MPF with a direct and simple signal process [68]. The general case is depicted in Figure 2.22 (a), where *N* lasers are coupled into a Phase Modulator (PM) followed by an optical filter. Figure 2.22 (b) shows the MPF bandpass signal results obtained from beatings between sidebands and the carrier of the used lasers. The amplitude and wavelength of the laser constituted input tuning parameters. In particular, the third laser amplitude parameter L_3 was used to achieve the tuneability of the MPF. Using many lasers allowed for optimizing the MPF response.

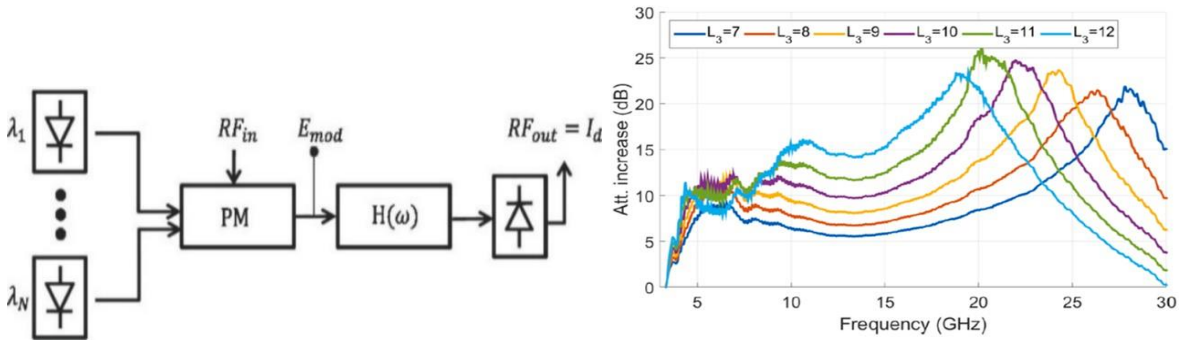

(a) (b)

Figure 2.22 (a) General MW-MPF setup, and (b) MPF response with L_3 tuned from 7 (dark blue) to 12 (light blue) (Image source: Daniel Nuño et al. Optics & Laser Technology 143, 2021 [68]).

Zhi-yong et al. by a modeling study and at the simulation level, demonstrated an MPF based on Brillouin Raman fibre laser (BRFL) [69]. The control of the BRFL optical channel numbers and wavelength spacing allowed for achieving the tuneability of the simulated microwave signals in a wide range. The main advantage of this work is the possibility of changing no matter how the parameters to see the system behaviour for eventual experimental implementations. Figures 2.23 (a) and (b) present respectively the basic structure of a multi-wavelength BRFL MPF, and its frequency response.

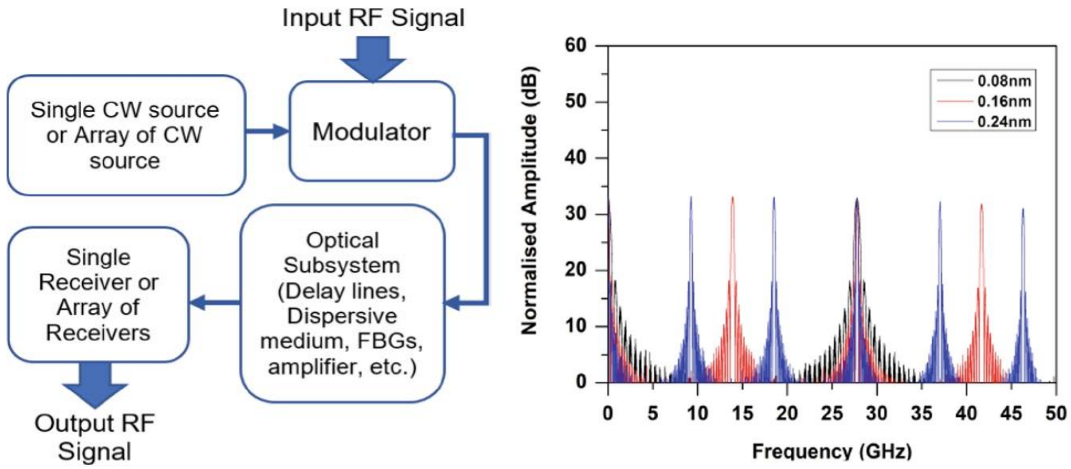

(a) (b)

Figure 2.23 (a) basic architecture of the BRFL MPF, and (b) simulated response of the filter (Image source: Zhi-yong et al. MECON 2022, pp. 174, 2022 [69]). CW: Continues Wave, FBG: Fibre Bragg Grating.

- *Tuneable OEOs:*

As mentioned above, OEOs can be built from the MPF system. Therefore, many tuneable OEOs have been demonstrated based on tuneable MPFs.

W. Zhang and J. Yao demonstrated the generation of a frequency-tuneable microwave signal of a silicon photonic integrated OEO [70]. This proposal is based on the tuneable MPF studied in their previous work [65]. Figure 2.24 presents the scheme of the silicon photonic OEO with the MDR between the Phase Modulator and the PD, which was implemented with the passband MPF realized based on phase modulation and phase-modulation to intensity-modulation (PM-IM) conversion.

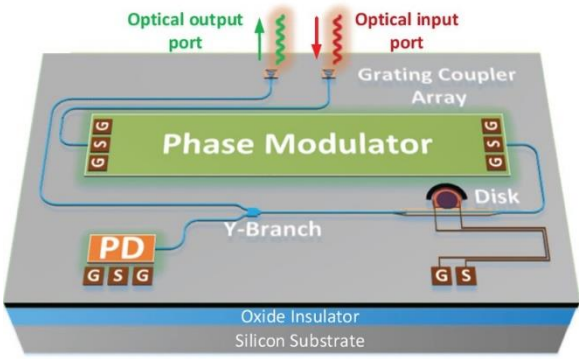

Figure 2.24 Perspective view of the OEO integrated on a silicon-photonic chip. (Image source: W. Zhang et al. J. Lightw. Technol., 36, no. 19, pp. 4655, Oct. 2018 [70]).

The tuneability of the generated microwave signal was achieved by a thermally-controlled resonance frequency MDR. Figures 2.25 (a) and (b) show the electrical spectrums of the OEO at different frequencies controlled with a top-placed micro-heater. The frequency tuning range was obtained from 3 GHz to 7.4 GHz with phase noise around -80 dBc/Hz@10 KHz in the first case, and from 3 GHz to 6.8 GHz with phase noise around -78 dBc/Hz@10 KHz in the second case.

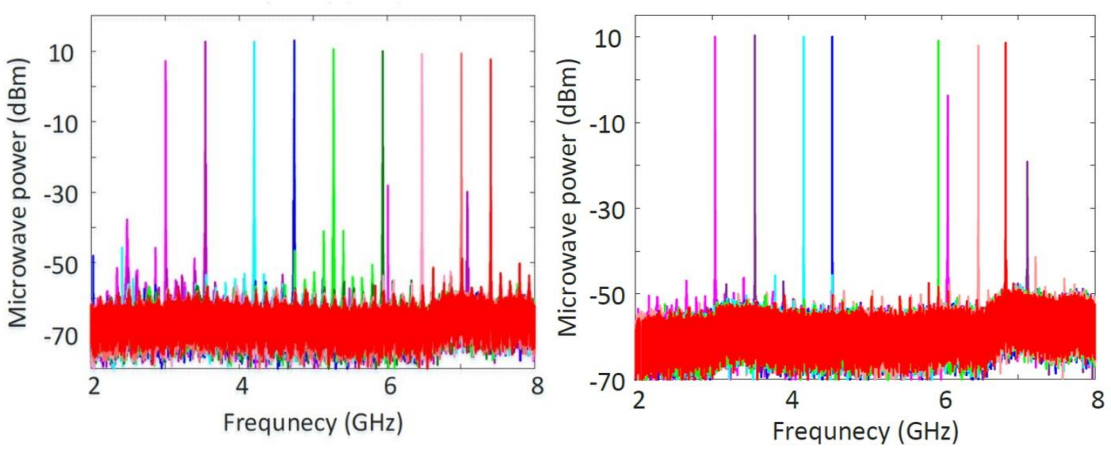

(a) (b)

Figure 2.25 Measured electrical spectrums with (a) a top-placed micro-heater and (b) a p-type doped silicon heater (Image source: W. Zhang et al. J. Lightw. Technol., 36, no. 19, pp. 4655, Oct. 2018 [70])

Z. Fan et al. proposed an OEO using an integrated MDR as like their MPF for the implementation of a parity-time (PT) symmetry as well as frequency tuning as exhibited in Fig. 2.26 (a) [71]. The

propagation reciprocity of light in the MDR allowed feeding mutually two identical geometry feedback loops, one with a gain coefficient and the other with a loss coefficient. Figure 2.24 (b) shows the frequency responses using a loop length of 74.39 m. Again, the tuneability was achieved by tuning thermally the MDR. The thermal tunning of the MDR resulted in a microwave signal tuneable range from 2 GHz to 12 GHz. The phase noise at a frequency of 11.5 GHz was measured as -102 dBc/Hz@10 KHz.

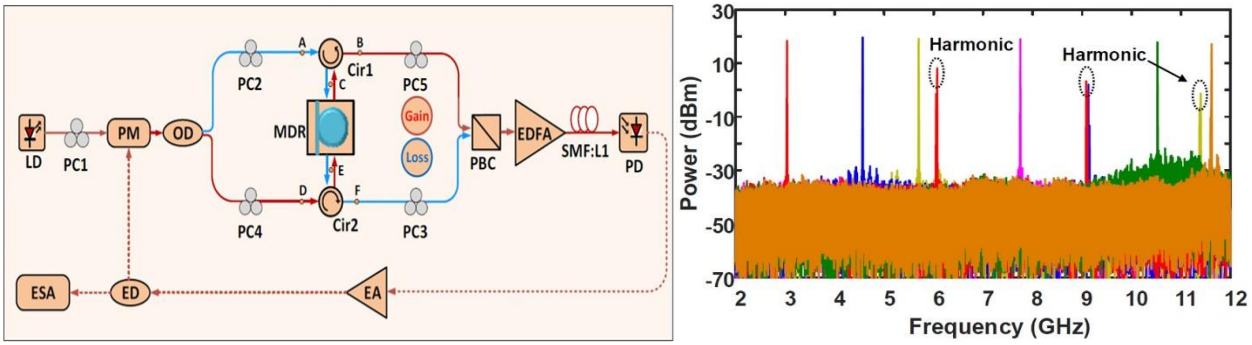

(a) (b)

Figure 2.26 The proposed highly tuneable PT-symmetric OEO based on an integrated MDR (a) schematic diagram (SMF: Single-Mode Fibre, EA: Electrical Amplifier); (b) Frequency tuneability (Image source: Z. Fan et al. J. Lightw. Technol., 38, no. 8, pp. 2127, 2020 [71]).

In 2021, Zerong Jia et al. presented theoretically and experimentally a high-tuneable OEO based on SiO_2 Optical Waveguide Ring Resonator (OWRR) with a frequency locking technology as shown in Fig.2.27 (a) [72]. A stable single-mode oscillation was obtained when the frequency of the laser was locked on the SiO_2 OWRR resonant frequency. The fine tuneability of the OEO was achieved with the adjustment of the laser frequency locking with a tuning step of 20 KHz. In particular, a microwave signal with frequency tuneability from 2.13745 GHz to 2.13771 GHz was generated with a phase noise of -89.18 dBc/Hz@10 KHz. This configuration provided a remarkable fine tuning allowing the OEO to be used in very selective system applications. Figure 2.27 (b) shows tuning oscillations.

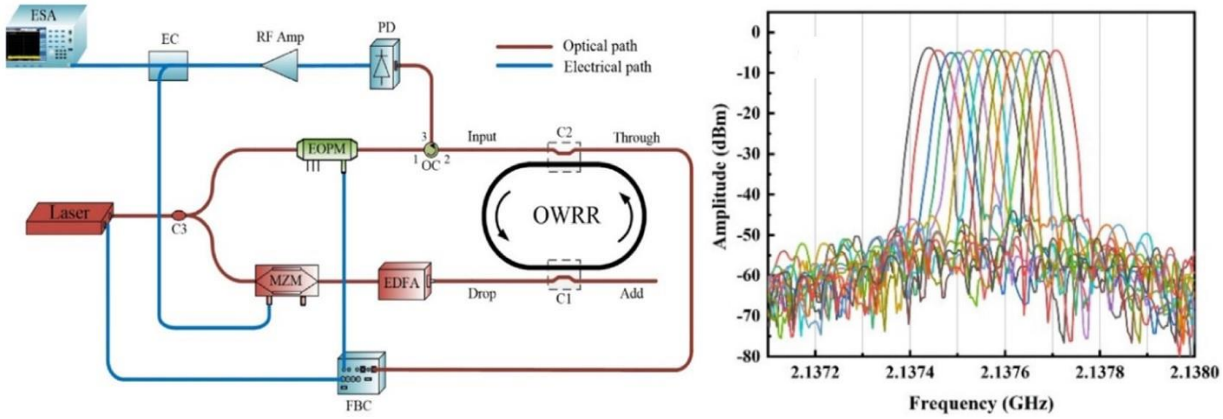

(a) (b)

Figures 2.27 (a) The schematic diagram of the OEO based on SiO_2 OWRR (EOPM: Electro-Optic Phase Modulator, FBC: Feedback Controller, EC: Electrical Coupler); (b) the oscillation spectra under different frequency locking parameters (Image source: Zerong Jia et al. Optics Communications, 498, 2021 [72]).

Tian Cui et al. have recently proposed and demonstrated a tuneable OEO based on a silicon nitride high-Q Microring Resonator (MRR) as depicted in Fig. 2.28 (a) [73]. A wide tuneable MPF was obtained with the insertion of this on-chip all-pass MRR ($Q = 4.36 \times 10^5$), into a phase-modulated link. The phase-to-amplitude modulation was achieved when one of the sidebands matched with the MRR resonance and then, a microwave signal was generated throughout the photodetector. In Fig. 2.28 (b), it is shown that the tuneable OEO generates microwave signals in the range of 14.60 GHz to 25.65 GHz. The phase noise at the oscillation frequency of 25.65 GHz was measured as -88 dBc/Hz@10 kHz.

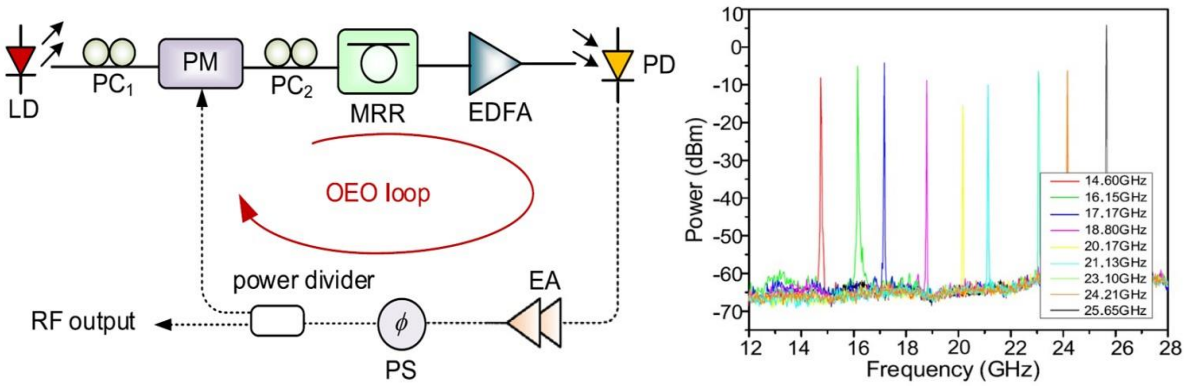

(a) (b)

Figures 2.28 (a) Schematic diagram of the MRR-based OEO. PS: Power Splitter (b) Frequency response tuning range (Image source: Tian Cui et al. Optics Communications, Volume 536, 2023 [73]).

L. J. Quintero-Rodríguez et al. presented an OEO with high-quality phase noise in [74]. A Birefringent Fibre (BF) of a few meters with two polarization controllers was inserted between the MLD and MZ-IM in order to build an optical filter as illustrated in Fig.2.29. The constructed tuneable multiple bandpass MPF was used for realizing the OEO.

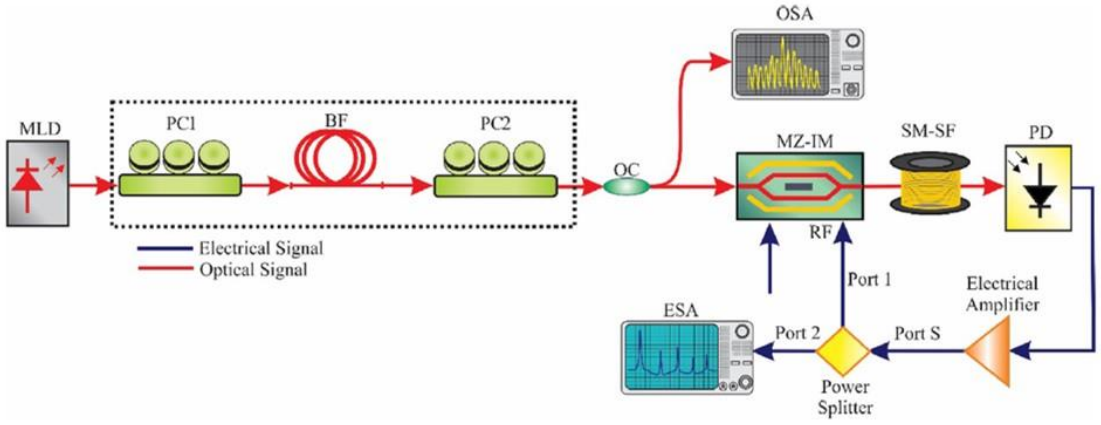

Figure 2.29 OEO based on band-pass MPF and an optical filter (Image source: L. J. Quintero-Rodríguez et al. Optics and Laser Technology 128, 2020 [74]).

The tuneability was achieved by using the optical filter that allowed the modification of the FSR of the MLD spectrum. Two different fibres BF1 and BF2 with their respective lengths L_{BF1} = 2.53 m and L_{BF2} = 2.00 m were used. Figures 2.30 (a) and (b) show the corresponding generated microwave oscillations with the FSR of 2.92 and 3.55 GHz. Their measured phase noise was

−118.06 and −113.56 dBc/Hz@10 KHz, respectively, which shows the generation of a high-quality microwave signal. In this thesis work, the study is based on this setup in order to demonstrate the dynamic tuneability of our MPF and OEO.

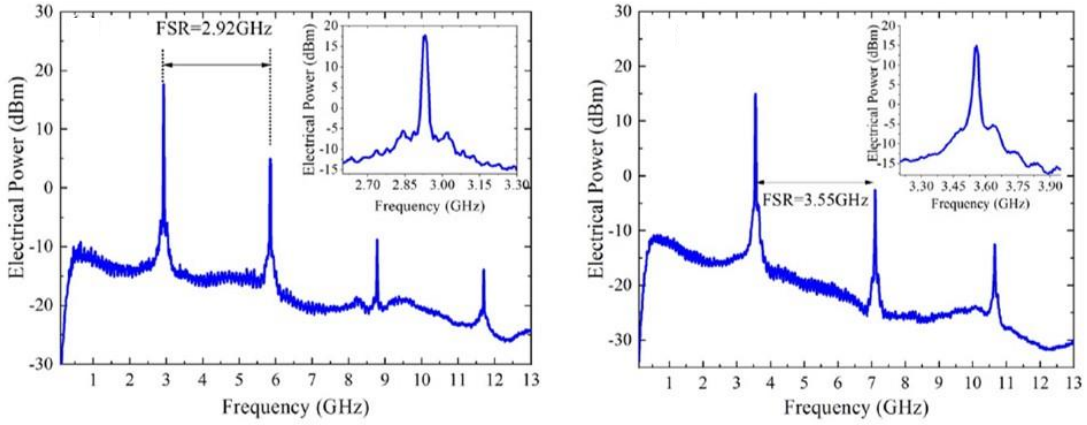

(a) (b)

Figures 2.30 Measured oscillation frequency signals with (a) BF1, and (b) BF2 (Image source: L. J. Quintero-Rodríguez et al. Optics and Laser Technology 128, 2020 [74]).

These remarkable results show the frequency tuneability of the proposed OEO. However, it is a static tuneability achieved by changing manually the piece of BF by another one with different length values. Therefore, for several desired frequency values, this type of manoeuvre becomes arduous, and tiring and at the same time reduces the efficiency of the system. The implemented optical filter should have another alternative. From these inconvenient, our work proposes the use of other devices to implement the MPF and the OEO where the tuneability is achieved simply, elegantly and dynamically.

Table 2.1 presents a summary of the works presented in the section. Typically, they show excellent results in terms of tunning rage and phase noise.

Table 2.1 Summary of different implemented OEOs.

Authors	Ref.	Year	Featured devices	Frequency (GHz)	Phase noise (dBc/Hz)@10 KHz
W. Zhang and J.Yao	[70]	2018	MDR	3 to 7.4; 3 to 6.8	-80@3 GHz; -78@3 GHz
Z. Fan et al.	[71]	2019	MDR	2 to 12	-102@11.5 GHz
L. J. Quintero-Rodríguez et al.	[74]	2020	BF	2.93; 3.55	-118.06@2.93 GHz; -113.56@3.55 GHz
Zerong Jia et al.	[72]	2021	OWRR	2.13745 to 2.13771	-89.18@2.13745 GHz
Tian Cui et al.	[73]	2023	MRR	14.60 to 25.65	-88@25.65 GHz

However, despite their excellent performance, their systems have some drawbacks such as complex architecture, no dynamical frequency tuning, and non-commercial components. In this thesis work, we are going to propose new tunning approaches for MPF and OEO. The approaches use a Fabry-Perot optical filter (FPF) or a semiconductor optical amplifier (SOA) and allow simple configurations for dynamic frequency tunning.

In the case of MPF, our configuration is simple and can easily be implemented for multiple passbands MPFs with dynamic tuneability. The works reported in Refs. [65,66,68] presented the tuneability of a single passband whilst our MPF generates a multiple passband that can be used as transmission channels simultaneously which is a great advantage in microwave communication systems. Moreover, the tunning of multiple passbands can be done dynamically and gradually compared to the work in Ref. [67].

The tuneable OEOs demonstrated in this thesis work are based on the tuneable MPF and will show performances as good as the ones presented by other techniques in Refs. [70-73]. Our systems have simple configurations with commercially-available components. As such, they can readily be implemented and cost-efficient. The tunning is also done dynamically and gradually using an FPF or an SOA.

2.4 Summary

In this chapter, the concept of MWP was defined and the general theory of fibre optics used for long-distance optical communications was given. Then, it was explained the composition and the

working principle of MPFs and OEOs. It was shown that the realization of the OEO is based on the MPF structure with an inserted optoelectronic feedback. For the OEO evaluation performance, an analytical method of phase noise determination was described. Moreover, the way to achieve tuneability for these two MWP systems was theoretically described. The key parameter for frequency tunning is the intermodal separation (mode spacing) $\delta\lambda$ that can be varied. It was explained also, that the working principle of devices such as tuneable FPF, tuneable DFB, and SOA, added to the structures of MPF and OEO could allow to achieve system tuneability.

A brief state of the art over the last five years was presented, to show the novelty and performances of the systems reported in the literature.

Finally, our new configurations of MPF and OEO were presented. In these systems, frequency tunning will be achieved using either an FPF with an MLD, or an SOA with two DFBs.

The next chapter will present the theory and simulations of frequency tuning of our systems.

CHAPTER 3: SIMULATIONS ON A TUNEABLE MULTI-BAND-PASS MICROWAVE PHOTONIC FILTER

3.1 Introduction

Most academics and students use specialized simulation software for research and work, assuring in this manner a high percentage of success in their experiments. This tendency has given rise to Computer Assisted Design (CAD) widely extended in the field of engineering. In the field of electronics, software such as Spice [75], Multisim [76], and, Proteus [77] are the most used among others. Whereas in the field of photonics, Optisystem [78] and VPIphotonics [79] are the most utilized. The main advantage of both Software is the user-friendly interface that allows users to manipulate easily their virtual devices, however, sometimes a particular device is not available therefore, is necessary to develop skills to solve the limitation.

Keeping in mind that simulation is defined as "the process of designing a model of a real system and conducting experiments with this model for the purpose either of understanding the behavior of the system or of evaluating various strategies for the operation of the system" [80]. In this regard, this chapter is focused on how to build multimode optical sources on VPIphotonics software and then simulations of multiple bandpass MPFs with the capabilities of tuneability. It is important to mention that simulation parameters are adjusted according to the availability of devices and components in our laboratory, considering the possibility of carrying out experiments.

In this sense, this part of the work is divided into three sections.

Firstly, we are going to investigate multimode optical sources. In order to simulate the tuneable MPF, a multimode source will be implemented on VPIphotonics software. For this purpose, two different approaches will be used on the software: (1) a combination of multiple single-mode sources and (2) two single-mode sources associated with a semiconductor optical amplifier (SOA). We will also study the way of modifying their intermodal separation ($\delta\lambda$) parameter.

Secondly, simulations of MPF on the software will be performed using these two different configurations and we will investigate and compare their RF output spectra for each configuration.

Finally, the feasibility of tuning the multiple bandpass MPF by modifying δλ of designed multimode sources will be shown. The frequency responses corresponding to different δλ parameters will be presented and their result values will be compared to those computed theoretically.

3.2 Principle and implementation of a multimode source

3.2.1 Principle of a multimode optical source

A multimode optical source is a particular case of a light source in which the spectrum is formed by the main mode symmetrically surrounded by multiple lateral modes enveloped by a Gaussian, Lorentzian, or Cos^2 line shape [81]. In this thesis work, our multimode optical source is considered to have a Gaussian envelope. A multimode optical spectrum of power P_s, centred at an optical frequency ω_o can be mathematically modelled as [72]

$$P_s(\omega-\omega_o)=\frac{2P_{max}}{\Delta\omega\sqrt{\pi}}exp\left(-\frac{4(\omega-\omega_o)}{\Delta\omega^2}\right)\cdot\left[\frac{2}{\sigma_\omega\sqrt{\pi}}exp\left(-\frac{4(\omega-\omega_o)^2}{\sigma_\omega^2}\right)*\sum_{n_m=-\infty}^{n_m=+\infty}\delta(\omega-n_m\delta\omega)\right] \tag{3.1}$$

Here, the term outside of the square bracket corresponds to the Gaussian envelope, P_{max} is the maximum power, $\Delta\omega$ is the Full-Width at Half-Maximum (FWHM) of the Gaussian envelope. Inside the brackets, σ_ω is the FWHM of the modes, $\delta\omega$ is the intermodal separation, $\sum_{n_m=-\infty}^{n_m=+\infty}\delta(\omega-n_m\delta\omega)$ is a Dirac comb function with a period $\delta\omega$, and n_m is the number of modes at FWHM. Indeed, the expression of Eq. (3.1) can be written in terms of wavelength λ by using the following set of expressions:

$$\omega=\frac{2\pi c}{\lambda},\qquad \omega_0=\frac{2\pi c}{\lambda_0},\qquad \Delta\omega=-\frac{2\pi c}{\lambda^2}\Delta\lambda,\qquad \delta\omega=-\frac{2\pi c}{\lambda^2}\delta\lambda \tag{3.2}$$

This means that the optical spectrum is composed of a centre wavelength (λ_0), a spectral width ($\Delta\lambda$), and an intermodal separation ($\delta\lambda$). Here, c ($3x10^8$ m/s) is the speed of the light in the vacuum. Eq. (3.1) is numerically simulated in MATLAB considering typical values for this type of optical source as λ_0 = 1550 nm, $\Delta\lambda$ = 10 nm, and $\delta\lambda$ = 0.36 nm. Figure 3.1 depicts the resulting multimode

optical spectrum. The inset corresponds to a zoom-in of the central zone showing in detail the δλ value.

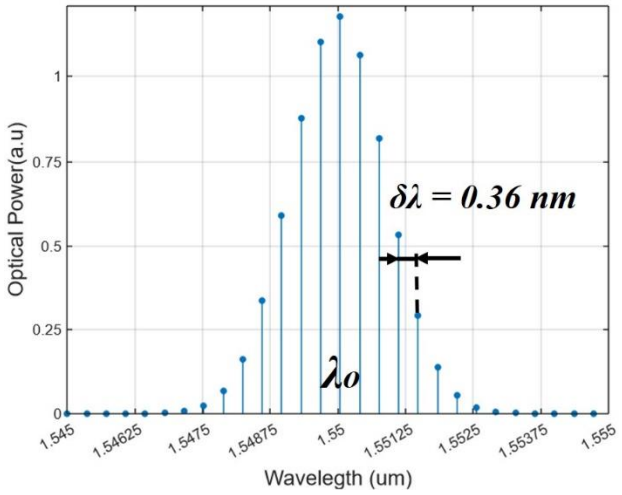

Figure 3.1 Optical spectrum generated by the use of Eq. (3.1).

3.2.2 Generation of a multimode optical spectrum using multiple single-mode sources

In order to simulate the MPF using a multimode source on VPIphotonics, it is necessary to design a multimode source for VPIphotonics. In fact, there is no library available for multimode optical sources on the Software (Version 11.4). Figure 3.2 depicts the VPIphotonics design of a multimode optical source composed of 21 modes. In this design, one continuous wave (CW) single-mode optical source is determined to be the centre wavelength at 1.55 µm (f = 193.41 THz computed from $\lambda = c/f$). From there, 20 other single-mode optical sources are added in order to generate side modes around the centre wavelength, shaping a Gaussian envelope. Their wavelengths are spaced by 0.36 nm which corresponds to the intermodal separation of the MLD used in this work. Then, all modes, whose linewidth is 10^6 Hz each, are assembled by using an optical combiner (Power N). Finally, the output of the combiner is connected to a signal analyser which in this case acts as an Optical Spectrum Analyser (OSA).

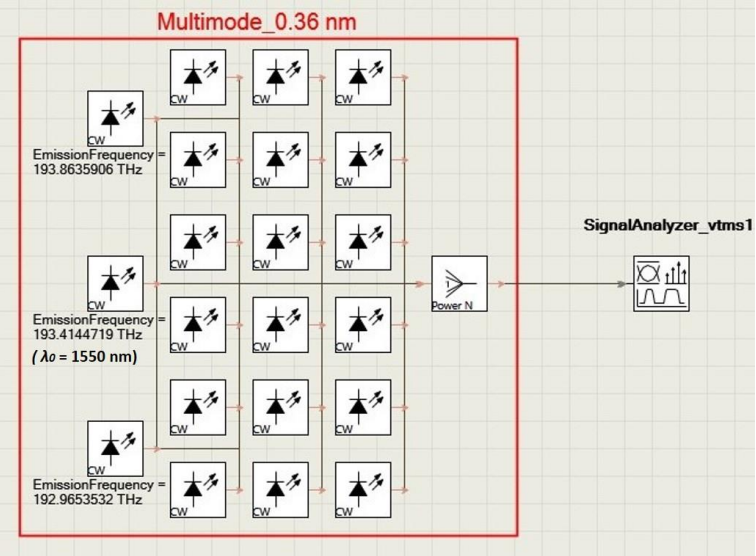

Figure 3.2 VPIphotonics layout of a multimode optical source using multiple single-mode sources.

Figure 3.3 exhibits the corresponding multimode optical spectrum obtained on VPIphotonics. The intermodal separation is observed as $\delta\lambda$ = 0.36 nm. The FWHM is determined from where it is assumed that the spectral line shape envelops whole the modes (see discontinuous red curve), which is $\Delta\lambda$ = 8.37 nm (black dashed line). The first mode is situated at 1546.47 nm (193.86 THz) and the last at 1553.83 nm (192.97 THz), forming a multimode spectrum with a limited number of 21 modes.

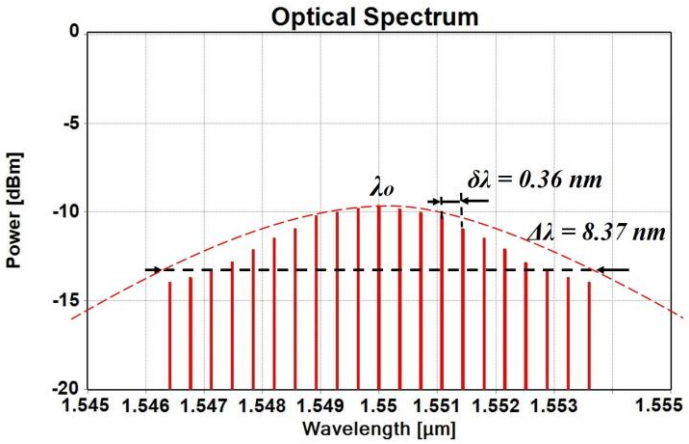

Figure 3.3 Multimode optical spectrum obtained with the VPIphotonics software.

The similitude between Figs. 3.1 and 3.3 is noticeable in terms of centre wavelength and intermodal separation. Due to the absence of a multimode optical source in the VPIphotonics

software library, the combination of multiple single-mode sources for generating a multimode spectrum can be used as a multimode source on the software. The resulting multimode spectrum was composed of several modes well-formed and separated. The next subsection presents another alternative for generating a multimode spectrum with this software.

3.2.3 Generation of a multimode optical spectrum using two single-mode sources and a semiconductor optical amplifier

Figure 3.4 shows another arrangement of VPIphotonics to obtain a multimode spectrum. This disposal consists of a couple of single-mode sources DFB1 and DFB2 emitting at wavelengths λ_1 and λ_2, respectively.

The main point of this design is that DFB1 is considered a discrete source whereas DFB2 is tuneable in frequency ($f = c/\lambda$). In fact, DFB laser diodes are sensitive to the laser temperature. Their wavelengths increase when the laser temperature increases. This is due to the thermal dilatation of the DFB cavity. This is the reason why DFB lasers must be stabilized in temperature by a good temperature controller. In our work, we are going to exploit this property for the tuning purpose. By changing the temperature, the wavelength of DFB2 is modified, leading to the wavelength tuning. However, the efficient tuning range is limited to less than or equal 1 nm using this method which corresponds to a temperature variation range of 10°C. The DFBs shown in Fig. 3.4 are connected to an optical coupler (OC) where one of the outputs is connected to a signal analyser vtms1 for monitoring the combined spectrum. While another output is sent to an SOA. The output of the SOA is connected to another signal analyser vtms2 for registering the optical spectrum generated by the SOA. The operation principle of this arrangement is explained below.

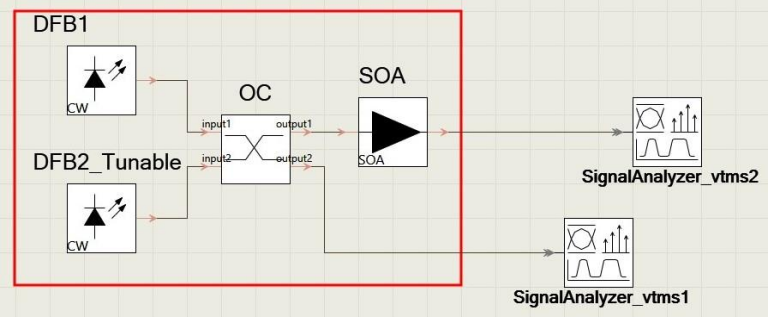

Figure 3.4 VPIphotonics layout of a multimode optical source using two single-mode optical sources and an SOA.

In particular λ_1 and λ_2 are established with $5x10^4$ Hz of linewidth. The light wave from the OC is injected into the SOA. The latter amplifies the optical power and at the same time, generates lateral wavelengths because of the Four Wave Mixing (FWM) nonlinear effect [62,82]. DFB1 is maintained at the emission frequency f_1 = 193.34 THz (λ_1 = 1550.60 nm). Whereas DFB2 is settled by directly changing its frequency parameter to different values, modifying the wavelength difference ($|\lambda_1 - \lambda_2|$). For instance, when DFB2 is set to the operating frequency f_2 = 193.45 THz (λ_2 = 1549.70 nm) the wavelength difference is 0.90 nm. When f_2 = 193.39 THz (λ_2 = 1550.20 nm) it provides 0.40 nm of difference. Figures 3.5 (a) and (b) show the generated optical spectra registered at different wavelengths. This wavelength difference corresponds to the intermodal separation $\delta\lambda$ of the generated multimode optical spectrum. Therefore, varying this difference allows for modifying the intermodal separation.

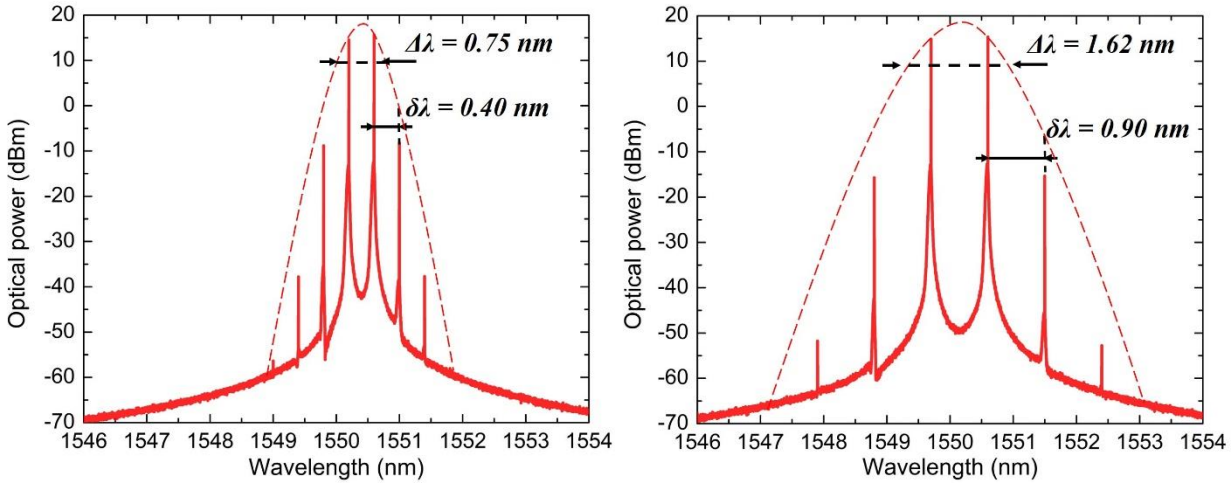

(a) (b)

Figure 3.5 Multimode optical spectra obtained on VPIphotonics with (a) $\delta\lambda$ = 0.40 nm, and (b) $\delta\lambda$ = 0.90 nm.

Figure 3.5 clearly shows the modification of the intermodal separation by setting DFB2 frequency. The spectrum width (FWHM) also changes. The spectrum width (see discontinuous red curve) $\Delta\lambda$ is 0.75 nm when $\delta\lambda$ = 0.40 nm and 1.62 nm when $\delta\lambda$ = 0.90 nm.

3.3 Multiple band-pass microwave photonic filter

Now, multiple passband microwave photonic filters will be simulated on VPIphotonics. For this purpose, multimode optical sources will be used in the simulation using the two different approaches studied above.

3.3.1 Multiple band-pass microwave photonic filter using the multiple single-mode sources

In order to demonstrate the MPF, first, we are going to use a multimode optical source composed of multiple single-mode sources. As stated in subsection 2.2.1, an MPF is composed basically of a continuous light source, a Mach-Zehnder Intensity Modulator (MZ-IM), an optical fibre (dispersive to the wavelength used), and a photodetector [83]. In particular, the use of a multimode optical source allows to obtain a microwave band-pass filter. Figure 3.6 shows the VPIphotonics layout to implement an MPF using multiple single-mode sources. The set of optical sources enclosed in the filled red box corresponds to the multimode optical source simulated in subsection 3.2.2. The operation principle of this configuration and simulation conditions are given below.

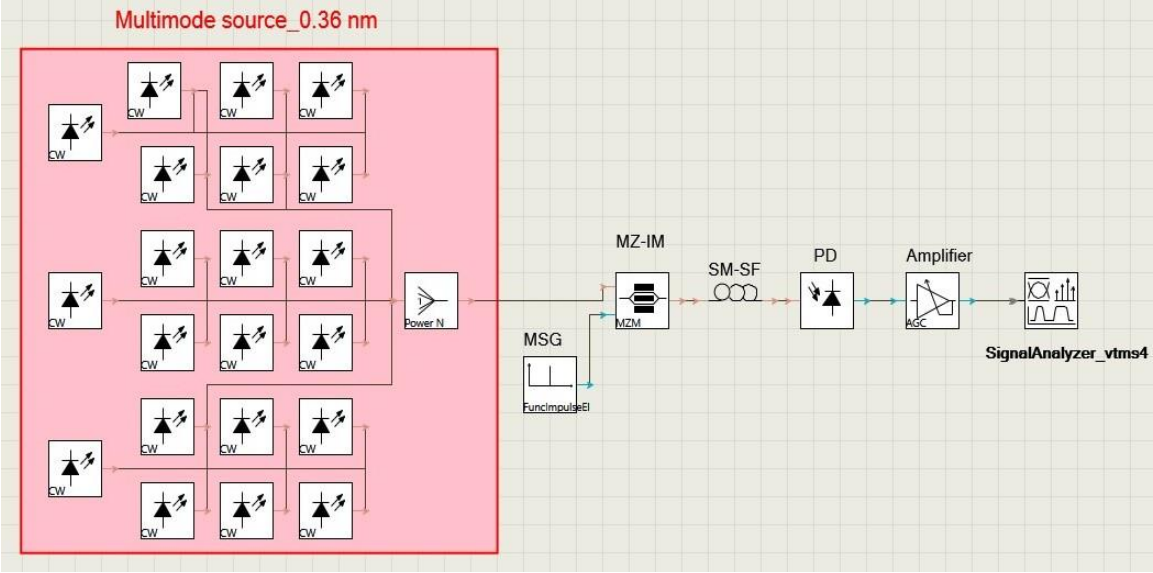

Figure 3.6 VPI photonics layout of the MPF using multiple single-mode optical sources.

The virtual Microwave Signal Generator (MSG) provides a sweep in frequency in the range of 0-16 GHz. The light of the multimode optical source is modulated in intensity by the electrical signal into the MZ-IM. The modulated light passes through the Single Mode-Standard Fibre (SM-SF) and is converted into an electrical current by the photodetector (PD). Finally, this electrical signal passes through the amplifier to get the needed level. A virtual instrument Signal Analyser is used to visualize the output RF spectrum like an Electrical Spectrum Analyser (ESA). Figures 3.7 (a) and (b) show the obtained microwave band-pass spectra for the cases of fibre lengths: L = 13 km and L = 50.28 km, respectively.

For L = 13 km, it appears in Fig. 3.7(a) a single band-pass peak centered at f = 13.83 GHz whose bandwidth at -3dB is Δf_{bp} = 597.33 MHz. For L = 50.28 km, there are in Fig. 3.7(b) four passbands, located at f_1 = 3.57 GHz, f_2 = 7.16 GHz, f_3 = 10.72 GHz, and f_4 = 14.36 GHz with their respective bandwidth at -3dB of Δf_{bp1} = 151.62 MHz, Δf_{bp2} = 175.16 MHz, Δf_{bp3} = 309.06 MHz, and Δf_{bp4} = 517.37 MHz.

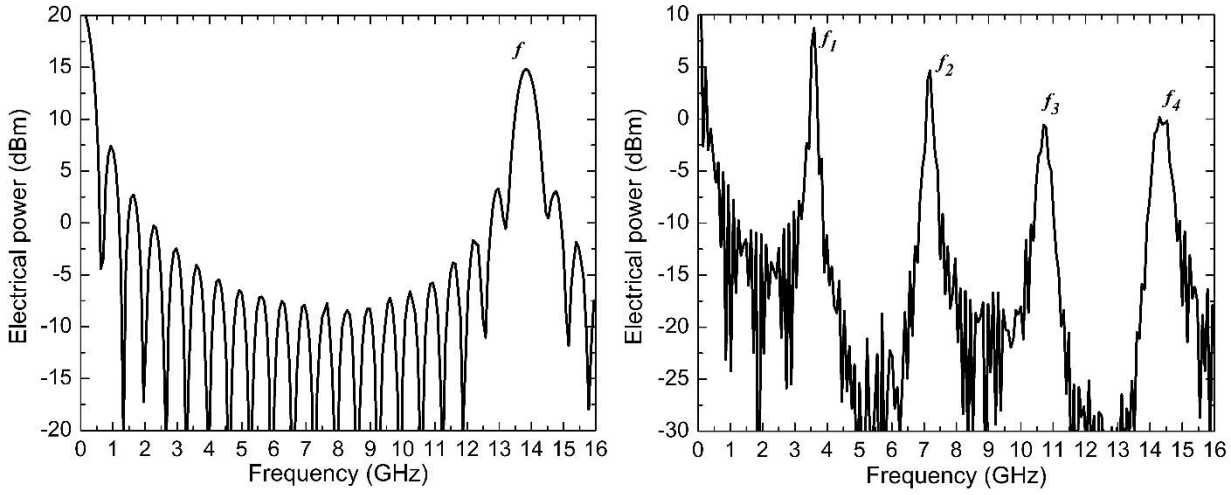

(a) (b)

Figure 3.7 Frequency response of the MPF driven by the combined multiple single-mode sources, using fibres of (a) L = 13 km and (b) L = 50.28 km.

The frequency response of the MPF is a single passband for L =13 km and a multiple passband for L = 50.28 km in the range of 0 – 16 GHz. In order to corroborate these simulated results, Equations (2.34) and (2.35) are used. The optical spectrum is characterized by $\delta\lambda$ = 0.36 nm and $\Delta\lambda$ = 8.37 nm and the frequency values of the bandpass peak registered at the output of the MPF are validated by computed values [83, 84].

In this sense, all the parameters previously indicated as well as a chromatic dispersion of D = 16.29 ps/nm·km, are substituted in the equations to compute theoretical values. Thus, is obtained f = 13.11 GHz and Δfbp = 695.57MHz for L =13 km whereas, multiple frequency values of f_1 = 3.39 GHz, f_2 = 6.78 GHz, f_3 = 10.17 GHz and f_4 = 13.56 GHz with their respective bandwidth Δfbp_1 = Δfbp_2 = Δfbp_3 = Δfbp_4 = 179.84 MHz are obtained for L = 50.28 km.

Table 3.1 summarizes the values of central frequencies as well as their respective bandwidths for theoretical and simulated results considering the two fibre lengths.

Table 3.1 Summary of theoretical and simulated values of the MPF driven by the combined multiple single-mode sources.

L = 13 km, D = 16.29 ps/nm·km, $\delta\lambda$ = 0.36 nm, $\Delta\lambda$ = 8.37 nm						
	Theoretical		**Simulated**		**Error**	
	f (GHz)	Δfbp (MHz)	f (GHz)	Δfbp (MHz)	εf (%)	$\varepsilon\Delta fbp$ (%)
	13.11	598.34	13.84	597.33	5.56	0.16
L = 50.28 km, D = 16.29 ps/nm·km, $\delta\lambda$ = 0.36 nm, $\Delta\lambda$ = 7.20 nm						
	Theoretical		**Simulated**		**Error**	
n	f_n (GHz)	Δfbp_n (MHz)	f_n (GHz)	Δfbp_n (MHz)	εf_n (%)	$\varepsilon\Delta fbp_n$ (%)
1	3.39	154.70	3.57	148.88	5.30	3.76
2	6.78	154.70	7.16	152.83	5.60	1.20
3	10.17	154.70	10.72	184.12	5.40	19.01
4	13.56	154.70	14.36	311.22	5.89	101.17

Compared to computed values, the simulated results are acceptable. That means the considered multimode source performed well in an MPF setup. The differences between their Δfbp_n are introduced since Δλ manually determined from the spectrum, does not coincide exactly with the value that the software considers. However, Δfbp_4 is wider than others (even Δfbp_3 gets a little broadening) seeing that the narrow shape part to the peak of the bandpass is not well-formed (carved out by the transmittance of the MPF).

3.3.2 Multiple band-pass microwave photonic filter using two single-mode sources and an SOA

The multimode optical spectrum obtained from the set implemented in subsection 3.2.3, exhibited interesting and essential characteristics for some applications. In particular, thanks to the adjustability of δλ and Δλ parameters, it provides a tuneability to an MPF. The operation principle of the MPF remains the same as the one explained above. Figure 3.8 shows the VPI photonics layout of the MPF driven by a multimode that consists of two single-mode sources associated with

an SOA (shown in the enclosed coloured box). Signal analysers vtms1 and vtms3 are used as OSAs for monitoring optical spectra at the output of the OC and the SOA, respectively. Whereas vtms4 acts as an ESA for registering RF spectra of the system. The simulation conditions are given, and the corresponding frequency responses are shown below.

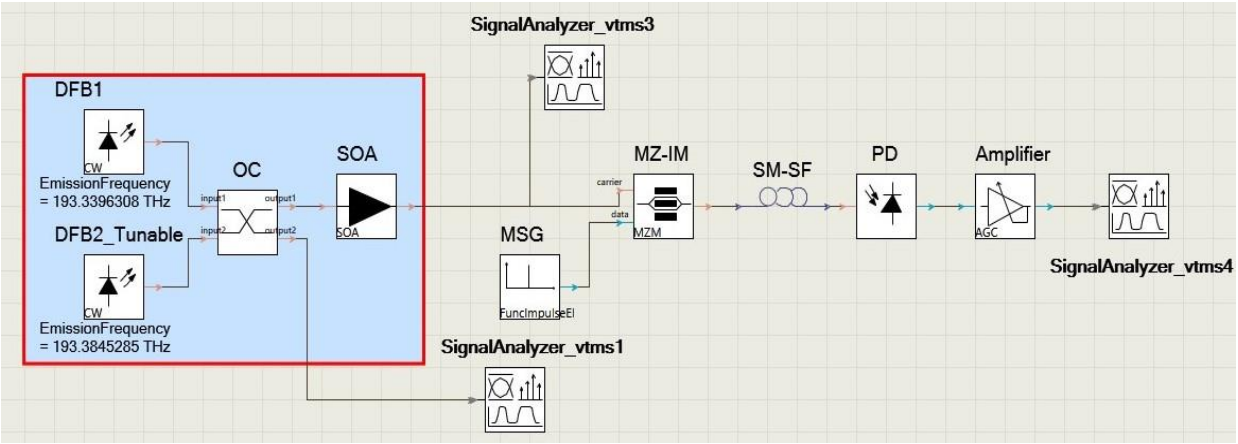

Figure 3.8 VPI photonics layout of the MPF using a multimode source implemented with two single-mode sources and an SOA.

In this case, DFB1 emits at 193.34 THz (1550.60 nm) and DFB2 at 193.38 THz (1550.24 nm). Thus, the combined wave at output2 of the OC is displayed by vtms1 exhibiting a wavelength difference $|\lambda_1 - \lambda_2|$ = 0.36 nm as shown in Fig. 3.9 (a). The other combined wave signal from output1 is injected into the SOA, generating a multimode spectrum at its output. Figure 3.9 (b) shows the optical spectrum registered at the output of the SOA, where the intermodal separation and FWHM are measured as $\delta\lambda$ = 0.36 nm and $\Delta\lambda$ = 0.74 nm, respectively.

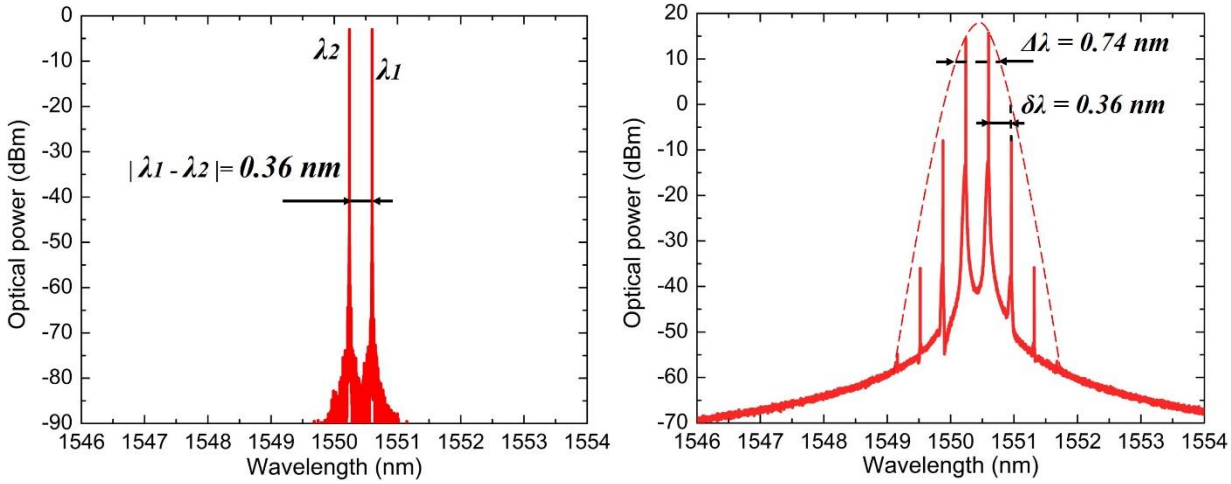

(a) (b)

Figure 3.9 (a) Bimode spectrum at the output of the OC, (b) Multimode spectrum at the output of the SOA.

The multimode emission generated by this approach goes through the MZ-IM, the optical fibre, and the PD like the MPF using multiple optical sources as mentioned above. The frequency response of the system is observed by vtms4. As it was demonstrated in the previous section, here again, the two fibre lengths of 13 km and 50.28 km are considered. Figures 3.10 (a) and (b) show the registered frequency responses with each optical fibre.

For L = 13 km, it appears a single and wide passband located at f = 13.85 GHz with a bandwidth of Δf_{bp} = 6.75 GHz. In this case, the frequency response is displayed in the range of 0 to 20 GHz in order to observe the entire passband. On the other hand, for L = 50.28 km, there are four passbands centred at f_1 = 3.29 GHz, f_2 = 6.98 GHz, f_3 = 10.34 GHz, and f_4 = 13.86 GHz with their respective bandwidths at -3dB of Δf_{bp1} = 151.62 MHz, Δf_{bp2} = 175.16 MHz, Δf_{bp3} = 309.06 MHz, and Δf_{bp4} = 517.37 MHz.

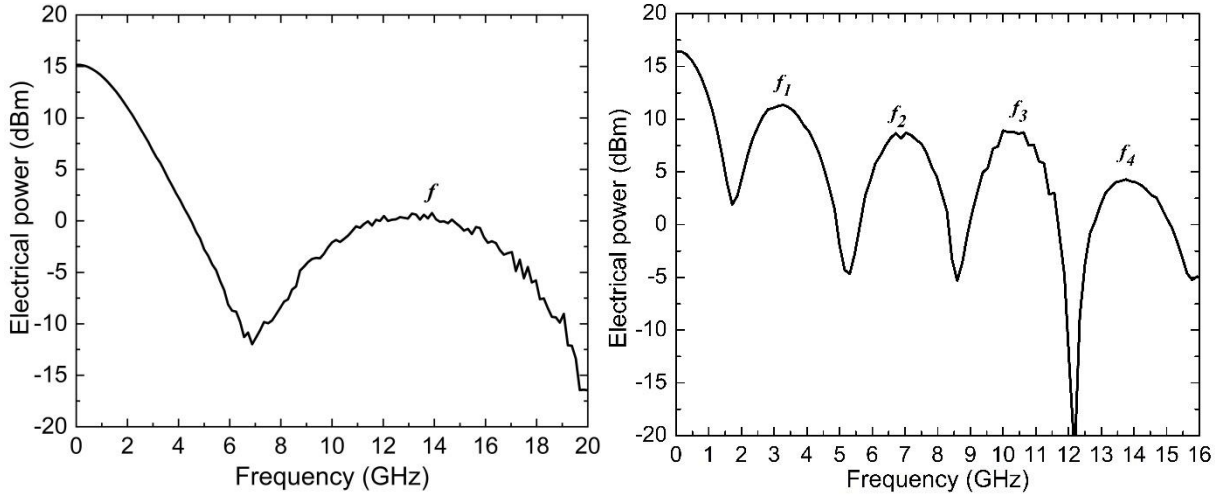

(a) (b)

Figures 3.10 Frequency responses of the MPF driven by two single-mode sources and an SOA, using fibres of (a) L =13 km and (b) L = 50.28 km.

It is seen here that the passbands of the MPF are much wider than those of the MPF using multiple optical sources presented in the previous section. This is justified by the fact that the used multimode signal has a smaller Δλ than the other (see Eq. (2.35)).

Theoretical results are computed by Eqs. (2.34) and (2.35), substituting all optical parameters depicted by this system. Therefore, using a fibre of L = 13 km the centre frequency of the MPF is obtained as f = 13.11 GHz with a bandwidth of Δf_{bp} = 4.63 GHz. On the other hand, using a fibre of L = 50.28 km four frequencies are obtained as f_1 = 3.39 GHz, f_2 = 6.78 GHz, f_3 = 10.17 GHz, and f_4 = 13.56 GHz with a bandwidth of $\Delta fbp_1 = \Delta fbp_2 = \Delta fbp_3 = \Delta fbp_4$ = 1.19 MHz for each passband.

Table 3.2 summarizes the results values obtained theoretically and by simulation for this MPF configuration using fibres of L = 13 km and L = 50.28 km.

Table 3.2 Summary of theoretical and simulated results of the MPF driven by two single-mode sources and an SOA.

L = 13 km, D = 16.29 ps/nm·km, $\delta\lambda$ = 0.36 nm, $\Delta\lambda$ = 0.74 nm						
	Theoretical		**Simulated**		**Error**	
	f (GHz)	Δfbp (GHz)	f (GHz)	Δfbp (GHz)	εf (%)	$\varepsilon\Delta fbp$ (%)
	13.11	6.76	13.85	6.75	5.64	0.14
L = 50.28 km, D = 16.29 ps/nm·km, $\delta\lambda$ = 0.36 nm, $\Delta\lambda$ = 0.74 nm						
	Theoretical		**Simulated**		**Error**	
n	f_n (GHz)	Δfbp_n (GHz)	f_n (GHz)	Δfbp_n (GHz)	εf_n (%)	$\varepsilon\Delta fbp_n$ (%)
1	3.39	1.74	3.29	1.84	2.94	5.74
2	6.78	1.74	6.98	1.84	2.94	5.74
3	10.17	1.74	10.34	1.75	1.67	0.57
4	13.56	1.74	13.86	1.98	2.21	13.79

As seen in the table, the centre frequencies of simulated results are in good agreement with the theoretical values. The difference between the respective bandwidth values is due to the response curve of the MZ-IM and another element linked to the length of the fibre, which affect the uniform formation of passbands. Longer fibres produce large gaps between bandwidth values.

3.4 Tuneable multiple band-pass microwave photonic filter

In this section, we are going to investigate the tuneability of the multiple band-pass MPFs presented previously using two methods: one with a Fabry-Perot optical filter and another one with a tuneable DFB laser diode. With these methods, the intermodal separation δλ is modified, leading to tuning the frequency passband of the MPFs.

3.4.1 Tuneability using a Fabry-Perot optical filter

The theory in section 2.2.3 explained the principle of operation of a Fabry-Perot Filter (FPF). Indeed, the transmittance of the FPF device in VPIphotonics software is variable by the setting of

its FSR value. Figure 3.11 shows an implemented MPF where the FPF is inserted in the setup presented in Fig. 3.6 between the multimode optical source and the MZ-IM. The FPF has a specific aim to modify the δλ parameter of the light source spectrum and thus, achieve tuneability of the MPF.

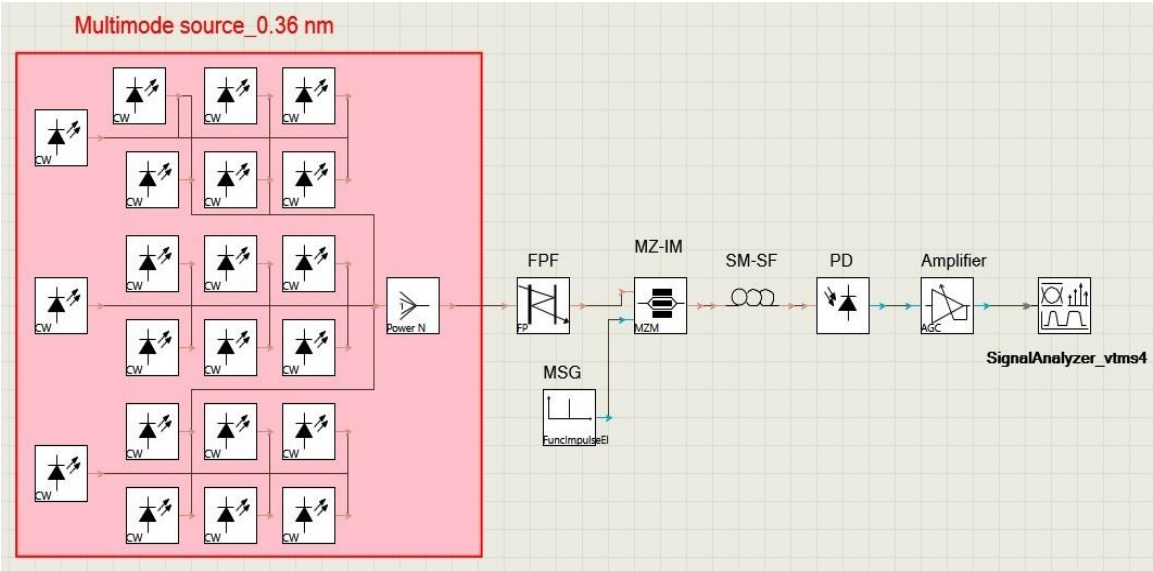

Figure 3.11 Layout of the simulated MPF using an FPF to achieve MPF tuneability.

By changing the FSR parameter of the FPF, δλ of the initial multimode spectrum is modified. The $\delta\lambda$-modified light is exploited in the MPF process. Again, two fibre optic lengths (L = 13 km and L = 50.28 km) are considered. Figures 3.12 (a) and (b) exhibit the filtered spectra at the output of the FPF. The results are obtained using two FSR values: FSR = 90 GHz, modifying to $\delta\lambda$ = 0.72 nm, and FSR = 135 GHz changing to $\delta\lambda$ = 1.08 nm.

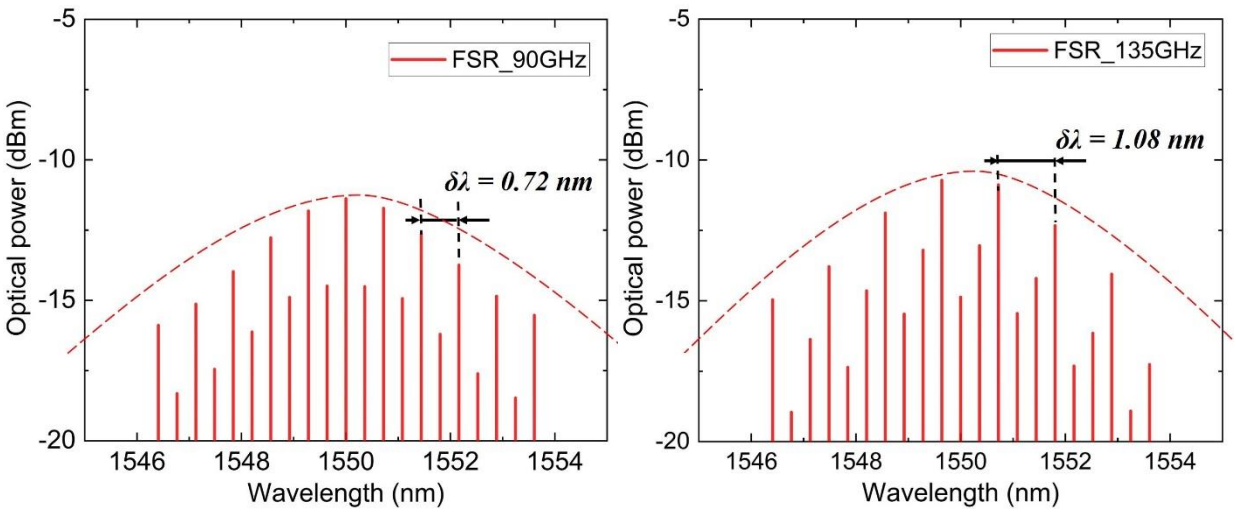

(a) (b)

Figures 3.12 Optical spectrum at the output of the FPF (a) *FSR*= 90 GHz and (b) *FSR*= 135 GHz.

With the fibre length of L = 13 km, simulations are done for $\delta\lambda$ = 0.72 nm (*FSR*= 90 GHz) and $\delta\lambda$ = 1.08 nm (*FSR*= 135 GHz). Figure 3.13 exhibits the frequency response of the MPF with $\delta\lambda$ = 0.72 nm in the blue curve and $\delta\lambda$ = 1.08 nm in the red curve.

In the case of $\delta\lambda$ = 0.72 nm (blue curve), two passbands are observed in the same spectrum range compared to the one shown in Fig. 3.7. The centre frequencies of two passbands are located at f_1 = 6.92 GHz, and f_2 = 13.84. The second passband at f_2 matches the frequency passband f shown in Fig.3.7. The first passband at f_1 appears at the half of the one at f_2. From Eq. (2.34) if δλ is n-times multiple of another one, then the MW signal appears constituted of n-passbands including initial one(s).

In the case of $\delta\lambda$ = 1.08 nm (red curve), three passbands are observed at f_1 = 4.59 GHz, f_2 = 9.26 GHz, and f_3 = 13.84. It is seen from Fig. 3.13 that the centre frequencies of these new passbands are submultiple of the initial passband located at 13.84 GHz.

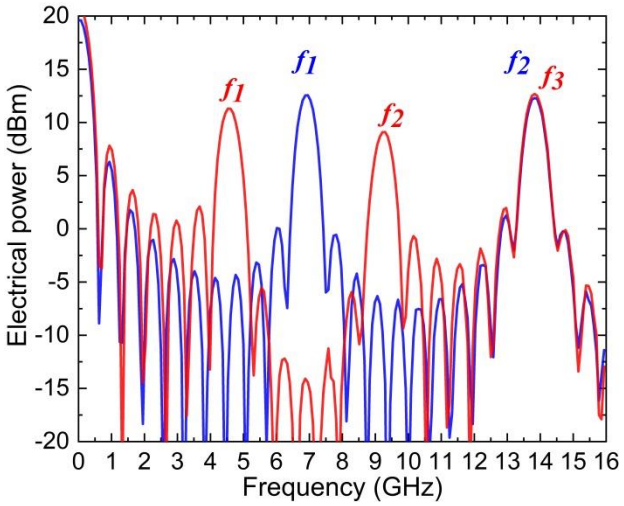

Figure 3.13 Frequency responses of the MPF driven by multiple single-mode sources with $\delta\lambda$ = 0.72 nm (blue curve) and $\delta\lambda$ = 1.08 nm (red curve).

As δλ increases, the first passband frequency decreases as expected from Eq. (2.34). On the other hand, the bandwidth of passbands remains almost unchanged as it depends on the fibre length or the optical spectrum width (See Eq. (2.35)).

Now, the length of the optical fibre is set to L = 50.28 km, and simulations are done with the considered two FSR values: $\delta\lambda$ = 0.72 nm and $\delta\lambda$ = 1.08 nm. Figure 3.14 shows the frequency responses of the MPF with *FSR*= 90 GHz ($\delta\lambda$ = 0.72 nm) and *FSR*= 135 GHz ($\delta\lambda$ = 1.08 nm). In the case of $\delta\lambda$ = 0.72 nm. The registered result consists of eight microwave passbands observed while 13 passbands are obtained in the case of $\delta\lambda$ = 1.08 nm.

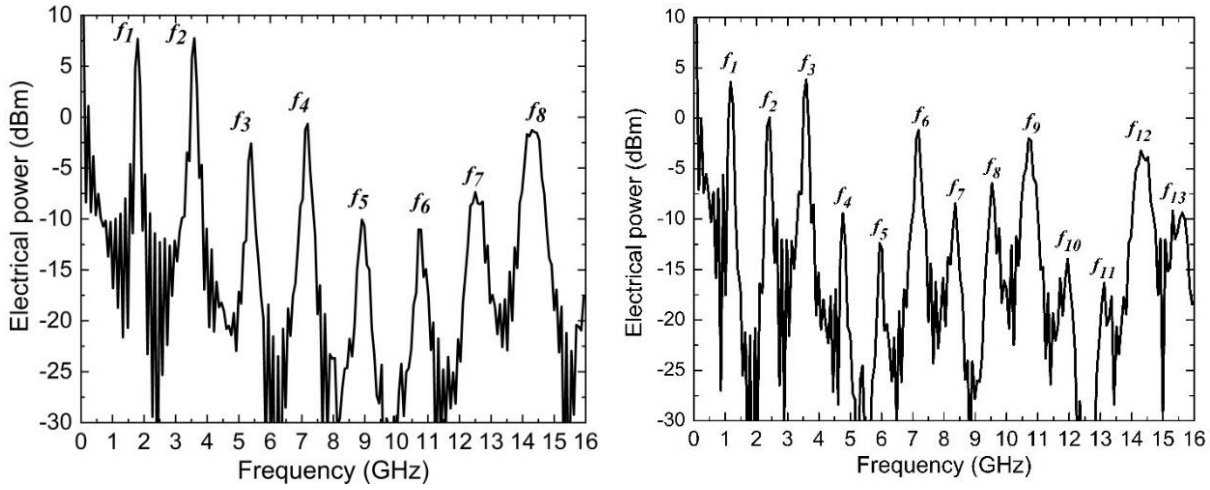

(a) (b)

Figure 3.14 Frequency responses of the MPF driven by multiple single-mode sources with (a) $\delta\lambda$ = 0.72 nm and (b) $\delta\lambda$ = 1.08 nm.

The frequencies of the first passbands are summarised for each case with the theory and simulation values in Table 3.3. The frequencies obtained from the simulations are in good agreement with the theoretical ones.

Table 3.3 Summary of results for the MPF driven by multiple single-mode sources.

		D = 16.29 ps/nm·km	
		L = 13 km	**L = 50.28 km**
		f_1 (GHz)	f_1 (GHz)
$\delta\lambda$ = 0.36 nm	*Simulated*	13.83	3.57
	From Eq. (2.34)	13.11	3.39
$\delta\lambda$ = 0.72 nm	*Simulated*	6.92	1.81
	From Eq. (2.34)	6.55	1.69
$\delta\lambda$ = 1.08 nm	*Simulated*	4.56	1.16
	From Eq. (2.34)	4.37	1.13

It is shown from Eq. (2.34) that the frequencies vary as $\delta\lambda$ is modified by the FPF and also, as the fibre length is changed. The results show that the tuneability of the MPF can potentially be achieved using a Fabry-Perot filter and a multimode laser diode.

3.4.2 Tuneability using a tuneable DFB

In section 3.3.2, we have seen that the set of two single-mode sources and an SOA can generate a tuneable multimode emission and be used for implementing a bandpass MPF.

As mentioned in section 3.3.2, tuneability is an intrinsic characteristic of DFB lasers using the laser temperature. In our work, the wavelength of DFB2 is settled at different values to show the tuning feasibility of a bandpass MPF. On the other hand, the wavelength of DFB1 is fixed and emits at 1550.60 nm (193.34 THz). In order to generate spectra of δλ = 0.72 nm and δλ=1.08 nm, the wavelength of DFB2 is tuned to1549.88 nm (193.43 THz) and 1549.52 nm (193.47 THz), respectively. Again, two fibre lengths (L = 13 km and L = 50.28 km) are considered in this implementation of the MPF.

Figure 3.15 shows the result of simulations considering $\delta\lambda$ = 0.72 nm (blue curve) and $\delta\lambda$ = 1.08 nm (red curve) for the MPF implemented with L = 13 km. The frequency responses exhibit two passbands for $\delta\lambda$ = 0.72 nm and three passbands for $\delta\lambda$ = 1.08 nm. The number of passbands is matched to the one exhibited in Fig. 3.13. However, their bandwidths are much wider than the ones in Fig. 3.13. This is because the bandwidth depends on the FWHM Δλ of the multimode source as expected from Eq. (2.35). For instance, as seen in Fig. 3.9 (b), the multimode spectrum is narrower than the one in Fig. 3.3 with multiple single-mode sources. In fact, the spectrum FWHM in Fig. 3.9 (b) is $\Delta\lambda$ = 0.74 nm whilst the one in Fig. 3.3 is $\Delta\lambda$ = 8.37 nm.

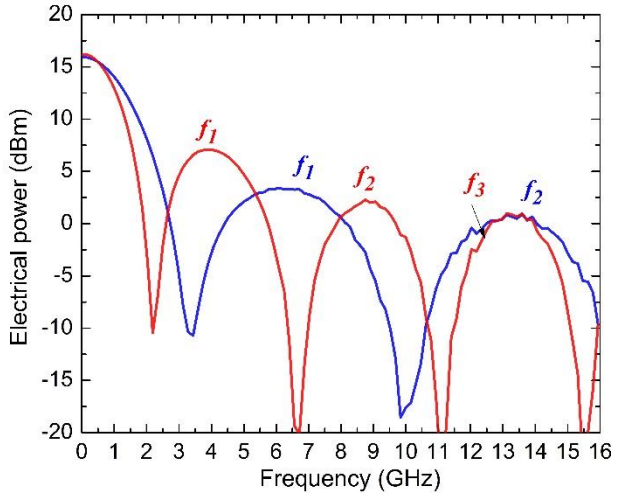

Figure 3.15 Frequency responses of the MPF driven by two single-mode sources with an SOA for $\delta\lambda$ = 0.72 nm (blue curve) and $\delta\lambda$ = 1.08 nm (red curve).

Now, the length of the optical fibre is set to L = 50.28 km, and simulations are done again with the same parameters. Figure 3.16 shows the results for $\delta\lambda$ = 0.72 nm and $\delta\lambda$ = 1.08 nm. In the figure, eight passbands are observed for $\delta\lambda$ = 0.72 nm and thirteen passbands for $\delta\lambda$ = 1.08 nm.

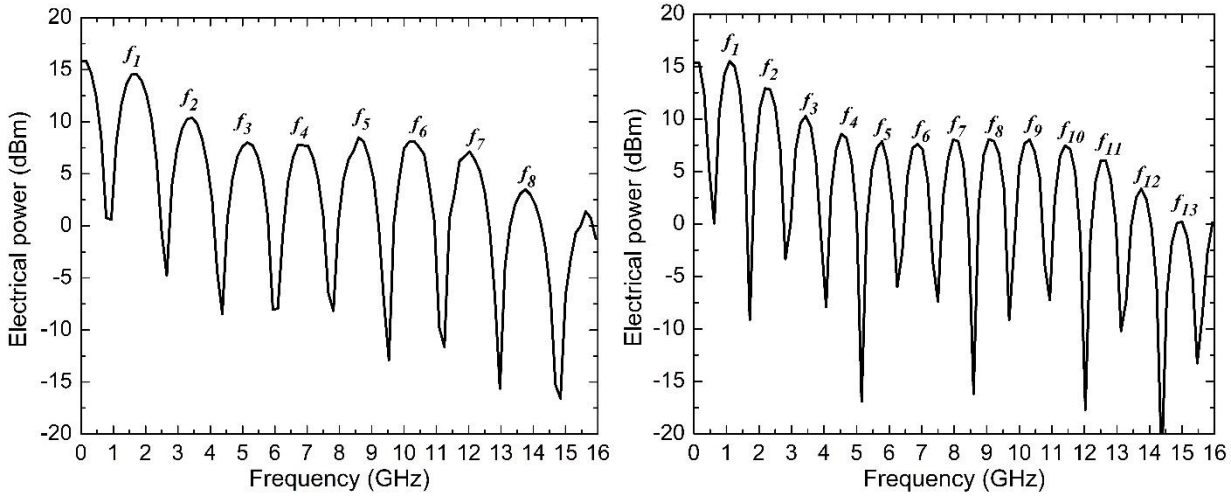

(a) (b)

Figure 3.16 Frequency responses of the MPF driven by two single-mode sources and an SOA for (a) $\delta\lambda$ = 0.72 nm and (a) $\delta\lambda$ = 1.08 nm.

The central frequencies of the first passbands for simulated results are listed together with the ones calculated by Eq. (2.34) in Table 3.4. It is clearly shown in the table that the numerical and theoretical values are in good agreement between them.

As seen from the results, the passband frequencies vary by modifying the intermodal separation. Unlike the method with the FPF, in this case, the tuneability of the MPF can be achieved by changing the frequency value of one of the DFB laser diodes in the setup. The fibre length also plays a role in tuning frequencies, but in practice, there is no way to vary the fibre length.

Table 3.4 Summary of results for the MPF driven by two single-mode sources and an SOA.

		D = 16.29 ps/nm·km	
		L = 13 km	**L = 50.28 km**
		f_1 (GHz)	f_1 (GHz)
$\delta\lambda$ = 0.36 nm	*Simulated*	13.85	3.29
	From Eq. (2.34)	13.11	3.39
$\delta\lambda$ = 0.72 nm	*Simulated*	6.79	1.68
	From Eq. (2.34)	6.55	1.69
$\delta\lambda$ = 1.08 nm	*Simulated*	4.17	1.13
	From Eq. (2.34)	4.37	1.13

It is noticeable that tuning capabilities of the MPF are feasible with the adjustment of δλ and its reconfigurability property is achievable with the variation of the fibre length.

3.5 Summary

In this chapter, we have performed simulations on multiple band-pass microwave photonic filters (MPF) using multimode optical sources on the VPIphotonics software. In order to carry out simulations on the software, libraries for all optical components are needed. In particular, multimode optical sources are essential for simulations. However, VPIphotonics does not propose libraries for multimode sources. For obtaining a multimode spectrum on the software we have proposed two different approaches: a combination of multiple single-mode sources and a set of two single-mode sources and an SOA. The software has generated successfully optical spectra with an intermodal separation of $\delta\lambda$ = 0.36 nm using these two methods. They can be used as multimode optical source libraries on the software for other purposes.

The multi-bandpass MPF using the multimode spectra has been performed numerically on VPIphotonics. Simulations have also been carried out with two different fibre lengths: L = 13 km and L = 50.28 km. The frequencies of the MPF passbands are in good agreement with the theoretical ones.

Finally, it has been shown numerically on VPIphotonics that adjusting the δλ parameter of the multimode source allows tuning frequencies of passband MPFs. For this purpose, an FPF has been used to change δλ together with the combination of multiple single-mode sources. By modifying

the FSR parameter of the FPF to 90 GHz and 135 GHz, δλ has been obtained as $\delta\lambda$ = 0.72 nm and $\delta\lambda$ = 1.08 nm, respectively. Adjusting δλ can also be achieved using a set of two single-mode sources and an SOA. The wavelength of one of the lasers varies, by setting its emitted frequency at different values. The SOA produces a multimode spectrum from two different wavelengths by the four-wave mixing nonlinear effect. By doing so, $\delta\lambda$ of the multimode spectrum is adjusted to $\delta\lambda$ = 0.72 nm and $\delta\lambda$ = 1.08 nm. Simulations have been undertaken with these two $\delta\lambda$ and two fibre lengths of L = 13 km and L = 50.28 km. The frequencies of MPF passbands obtained in theory and simulations are in good agreement. The results show that the tuneability can be achieved using a multimode laser diode and an FPF or using a set of two single-mode laser diodes and an SOA. In the next chapter, we will see how the MPF is implemented using the two different methods and how tuneability is achieved in the experiment.

CHAPTER 4: EXPERIMENTAL SETUPS AND RESULTS

4.1 Introduction

Beyond the theoretical basis as well as the simulations presented previously, this chapter addresses the experimental part of this thesis work. Firstly, it describes a microwave photonic filter (MPF) and an optoelectronic oscillator (OEO) using a discrete multimode laser diode (MLD) characterized by its intermodal separation. Secondly, it demonstrates an OEO with tuneable capabilities. This OEO is driven by a set of two distributed feedback (DFB) laser diodes and a semiconductor optical amplifier (SOA) that allows a multimode emission. An MPF structure using such a multimode source found a novel OEO architecture. The microwave signals generated by means of the variation of the intermodal separation of the newly implemented multimode source are also presented.

4.2 Microwave Photonic Filter Setup

In our conventional MPF, a commercial Multimode Laser Diode (MLD, Covega FPL1009P) is used for a multimode emission. Its spectrum is measured using an Optical Spectrum Analyser (OSA, Anritsu MS9740A) over 20 nm of span. Figure 4.1 shows the optical spectrum obtained with 5001 sample points and 0.07 nm of resolution. From the spectrum, the optical characteristics are measured: a centre wavelength of λ_0 = 1550.48 nm, an intermodal separation of $\delta\lambda$ = 0.36 nm, and a spectral width of $\Delta\lambda$ = 4.19 nm. To avoid optical fluctuations, the MLD is driven by very stable current and temperature controllers and set to 450 mA and 18°C, respectively.

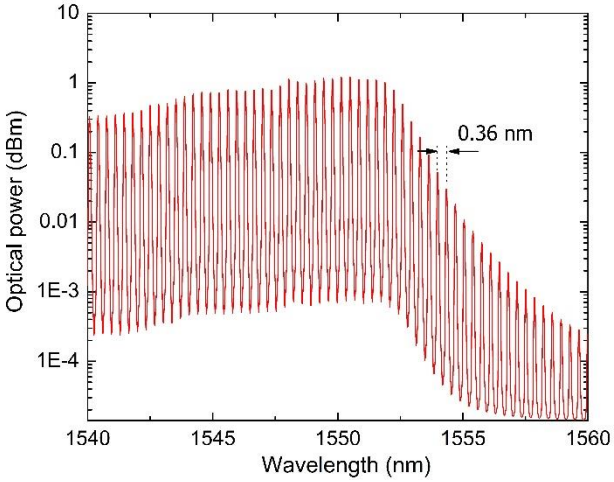

Figure 4.1 Optical spectrum of the MLD Covega FPL1009P.

4.2.1 Multiple passband microwave photonic filter

Figure 4.2 depicts the experimental scheme where the red dotted box represents a multiple passband MPF. The Microwave Signal Generator (MSG) provides microwave signals and the Electrical Spectrum Analyser (ESA) records the frequency response of the MPF. The principle of operation of the MPF is explained below in detail.

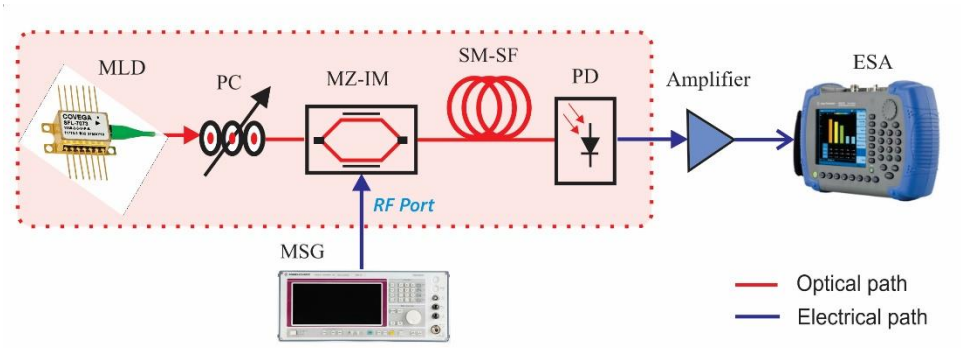

Figure 4.2 Experimental setup of the multiple passband MPF.

The emitted light from the multimode laser diode (MLD) passes through a fibre polarization controller (PC) for light polarization adjustment and then enters the Mach-Zehnder intensity modulator (MZ-IM) which modulates the light (Photline, MXAN-LN-20-bandwidth-20 GHz, insertion loss of 2.7 dB, $V\pi$ = 3.2 V, operating wavelength 1530-1580 nm) by a continuous RF signal provided by the MSG (Anritsu MG3692C) in the frequency range of 0-16 GHz at a power of 15 dBm. The modulated light is injected into a given 50.28 km long Single Mode-Standard

Fibre (SM-SF) with an optical loss of α = 0.20 dB/km and a chromatic dispersion of D = 16.29 ps/nm·km @1550 nm. At the output of the SM-SF, the light wave is received and converted into an electrical signal by the photodiode (PD, Miteq, Bandwidth-13 GHz). This electrical signal is amplified by an RF amplifier (Minicircuits, ZVA-183-S+ 700-18000 MHz, a gain of 26 dB) and plugged into the ESA (Agilent, N9344C) to display the system frequency response. Figure 4.3a shows the registered frequency response where four passband signals are observed at f_1 = 3.47 GHz, f_2 = 6.96 GHz, f_3 = 10.46 GHz, and f_4 = 13.76 GHz. Their electrical bandwidths at -3dB are Δfbp_1 = 291.09 GHz, Δfbp_2 = 322.92 GHz, Δfbp_3 = 425.89 GHz, and Δfbp_4 = 263.34 GHz, respectively.

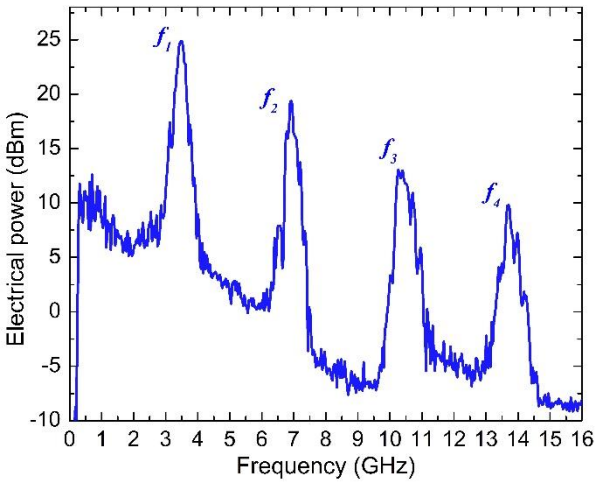

Figure 4.3 (a) Experimental spectrum measured at the output of the multiple bandpass MPF.

According to Ref. [85], the theoretical centre frequency and bandwidth of these passbands are computed by the equations: $f_n = n/DL\delta\lambda$ and $\Delta fbp_n = 4\sqrt{ln2}/\pi DL\Delta\lambda$, respectively. Thus, by substituting the parameters previously indicated, the centre frequencies and bandwidths are obtained as f_1 = 3.46 GHz, f_2 = 6.93 GHz, f_3 = 10.40 GHz, and f_4 = 13.87 GHz, and $\Delta fbp_1 = \Delta fbp_2 = \Delta fbp_3 = \Delta fbp_4$ = 308.67 MHz, respectively. Table 4.1 summarizes the theoretical and experimental values corresponding to the centre frequencies fn and bandwidth Δfbp_n of the passband windows, as well as, the error rate percentage between these values.

Table 4.1 Summary of theoretical and experimental values of the multiple bandpass MPF.

	Theoretical		**Experimental**		**Error**	
n	f_n (GHz)	Δfbp_n (MHz)	f_n (GHz)	Δfbp_n (MHz)	εf_n (%)	$\varepsilon \Delta fbp_n$ (%)
1	3.46	308.67	3.47	291.09	0.28	5.69
2	6.93	308.67	6.96	322.92	0.43	4.61
3	10.40	308.67	10.46	365.89	0.57	18.53
4	13.87	308.67	13.76	273.34	0.79	11.44
Average		308.67		313.33		1.50

The small difference between the theoretical and experimental values is justified by the inequality between the labelled and the real values of the fibre length, as well as the real value of the chromatic dispersion parameter. Another way to corroborate the efficiency of this experimental setup is to compare the similarities of its result and the one obtained at the simulation level using the same parameters. Figure 4.3b shows both experimental (black curve) and simulated (red curve) frequency responses of the multiple bandpass MPF.

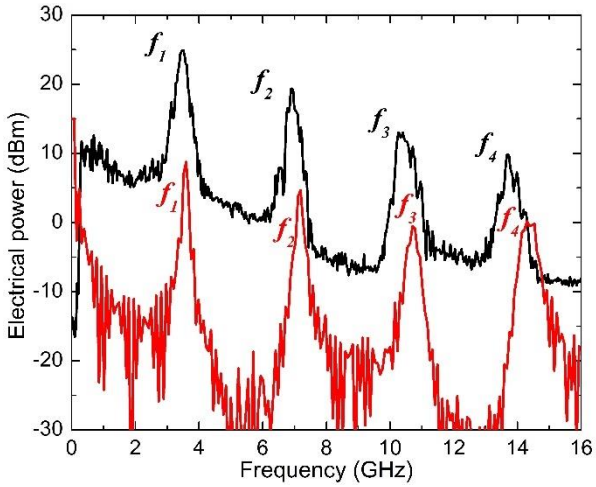

Figure 4.3 (b) Experimental and simulated frequency response of the multiple bandpass MPF.

The experimental and simulated curve shapes are similar and their centre frequency values are almost equal for all the passbands. In summary, the passband filter of which the centre frequency

depends mainly on the intermodal separation ($\delta\lambda$) of the MLD and the fibre length (L), has been successfully demonstrated.

4.2.2 Optoelectronic oscillator using a discrete MLD

The implementation setup of the OEO is similar to the one shown in Fig. 4.2 except that now after the fibre a recovered electrical signal is fed back to the RF port of the MZ-IM. Depending on the availability of devices various arrangements are realizable to deliver adequately the RF signal to the modulator. In this way, two feedback alternatives, using a direct RF signal and an optoelectronic converted signal, are presented in the following lines.

a) OEO with direct RF feedback

Figure 4.4 shows the implemented arrangement using an electrical power splitter and where the signal in the whole feedback is electric. Its principle of operation is described below.

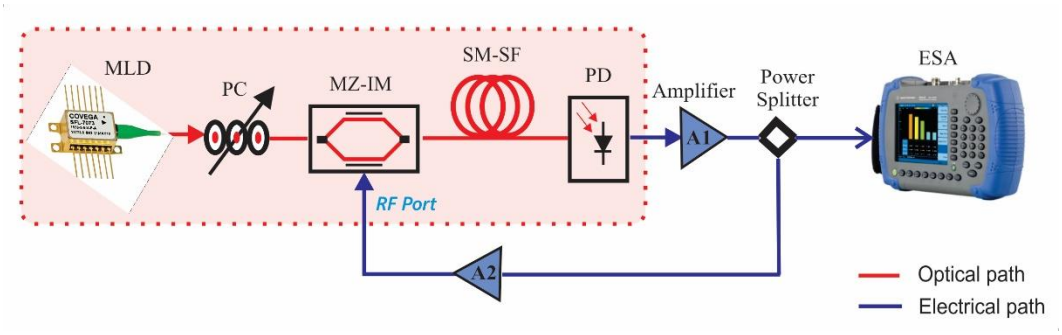

Figure 4.4 Experimental setup of the optoelectronic oscillator.

The electrical signal delivered by the amplifier A1 is divided using a power splitter, part of this signal is sent to the ESA, and the rest is fed back to the RF port of the MZ-IM, forming a closed-loop. By doing so, the output signal of the electro-optical system starts oscillating. Another amplifier A2 is used to increase the gain in the loop to start the oscillation. Figure 4.5 depicts the OEO output spectrum. Compared to the results of the previous experiment, it is noticed from the spectrum that the oscillation frequencies are situated at the same values of the passband windows as the ones of the MPF. The microwave signals are generated at 3.51 GHz (20.44 dBm, *SNR* = 31.57 dB), 6.99 GHz (9.04 dBm, *SNR* = 18.19 dB), 10.50 GHz (5.84 dBm, *SNR* = 15.63 dB) and 13.98 GHz (-0.24 dBm, *SNR* = 6.56 dB). They are separated by a Free Spectral Range (FSR) of 3.48 GHz.

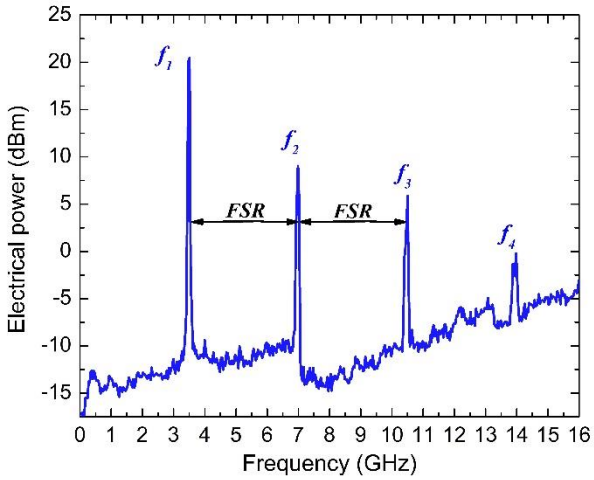

Figure 4.5 Experimental RF spectrum of the OEO.

The generated microwave signals exhibit good stability and SNR values. These oscillations frequencies are in good agreement with the theoretical values computed by Eq. (2.34) obtaining f_1 = 3.46 GHz, f_2 = 6.93 GHz, f_3 = 10.40 GHz, and f_4 = 13.87 GHz. Thus, *FSR* = 3.47 GHz. In the spectrum, the fourth oscillation peak is not shown because the system bandwidth is limited to 12 GHz. Table 4.2 summarizes the theoretical and experimental results.

Table 4.2 Summary of theoretical and experimental oscillation frequencies of the OEO with direct RF feedback.

n	**Theoretical**	**Experimental**		**Error**
	f_n (GHz)	f_n (GHz)	*SNR* (dB)	εf_n (%)
1	3.46	3.51	31.57	1.44
2	6.93	6.99	18.19	0.86
3	10.40	10.50	15.63	0.96
4	13.87	13.98	6.56	0.79

A metric to qualify the performance of an OEO is phase noise (PN) measurements. Generally, the measurement is carried out directly using an ESA with a function of PN measurement. The PN can also be measured analytically, computing it as explained in section 2.2.3.

First, the power of the oscillation frequency at f_1 = 3.51 GHz is obtained as *Pc* = 20.44 dBm in Fig 4.5. Then, the phase noise powers (P_{offset}) at different frequency offsets are normalised with the normalization parameter *N*. In particular, is indicated on the ESA screen a frequency span of 225

MHz, *RBW* = 1 KHz, and *VBW* = 1 KHz. Five offset points with decade frequency are chosen (10 KHz, 100 KHz, 1 MHz, 10 MHz, and 100 MHz). Figure 4.6 (a) shows the captured screen of the generated oscillations and Figure 4.6 (b) shows the ESA screen captured for phase noise power measurements at different offset points.

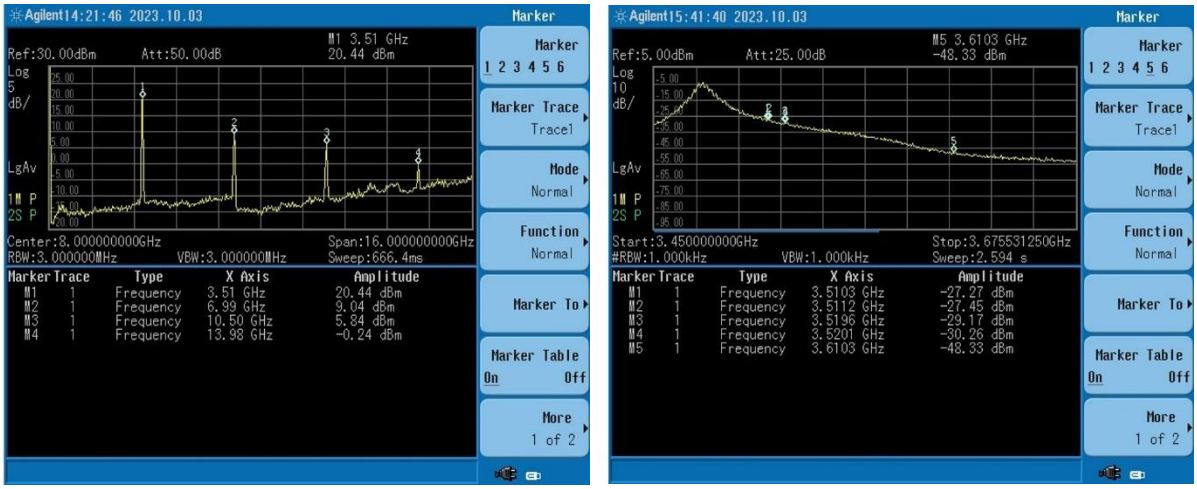

(a) (b)

Figure 4.6 Captured screens of (a) the generated signal of the OEO, and (b) the phase noise power measurements.

The markers in Fig. 4.6 (a) indicate the corresponding centre frequencies and powers of oscillations, whereas, in Fig. 4.6 (b) they show approximately offset point frequencies with their respective phase noise powers.

Considering that the shape correction is negligible, only the normalization parameter is taken into account in this analytical procedure and is determined as [86]

$$N = 10 \log RBW\,(Hz) = 10 \log(1000) = 30 \text{ dB}$$

The corresponding normalized 1 Hz noise power is computed as $Pn = P_{offset} - N$

Thus,

$Pn\_{10\,KHz} = -57.27$ dBm/Hz,

$Pn\_{100KHz} = -57.45$ dBm/Hz,

$Pn\_{1MHz} = -59.17$ dBm/Hz,

$Pn\_{10MHz} = -60.26$ dBm/Hz,

$Pn\_{100MHz} = -78.33$ dBm/Hz.

Finally, the OEO phase noise at each frequency offset is computed by [86,87]

$$\mathscr{L}(f) = Pn - Pc$$

Therefore,

$\mathscr{L}(f)_{\_10\ KHz}$ = -77.71 dBc/Hz,

$\mathscr{L}(f)_{\_100KHz}$ = -77.89 dBc/Hz,

$\mathscr{L}(f)_{\_1MHz}$ = -79.61 dBc/Hz,

$\mathscr{L}(f)_{\_10MHz}$ = -80.70 dBc/Hz,

$\mathscr{L}(f)_{\_100MHz}$ = -98.77 dBc/Hz.

These phase noise values are higher than the ones reported in the literature [49,50,52,88,89]. However, they are acceptable since this simple design of the OEO offers several possibilities for improving its performance with complemented devices or techniques [89].

b) OEO with an optoelectronic feedback

The OEO is implemented using a discrete multimode Fabry-Perot laser diode (MU951001A, FP-LD, 2.32 mW) which is not the same as the one used in the MPF setup. Its centre wavelength and intermodal separation are measured as λ_o = 1553.84 nm and $\delta\lambda$ = 0.58 nm, respectively (see Fig. 4.8 (a)). Figure 4.7 shows the implemented OEO where the feedback line is constituted of a photodetector followed by an RF amplifier.

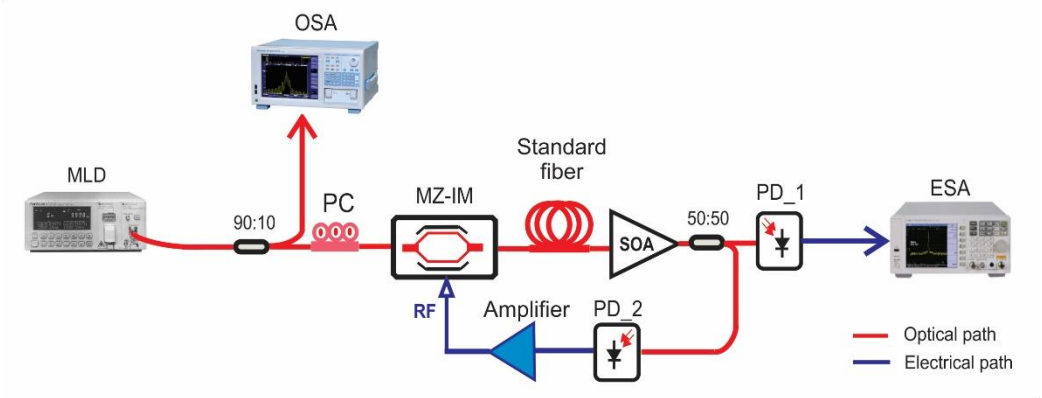

Figure 4.7 Experimental setup of the OEO with optoelectronic feedback.

The light wave at the output of the multimode source is divided by an optical coupler (90:10) where 10% of the light is sent to an optical spectrum analyser (OSA) and, the other 90% is injected to an MZ-IM (Hittite Microwave Corporation, 10 MHz-20 GHz). The light is modulated by the

MZ-IM and injected into a dispersive standard optical fibre of L = 15.95 km. The light at the output of the fibre is amplified by an SOA (Alcatel 1901) operating at a current of 100 mA and, then divided by an optical coupler (50:50). The output ports of the coupler are connected to two PDs. The signal from PD_1 is used for monitoring the frequency response on the ESA (Agilent E4407), whereas PD_2 is used for establishing a feedback loop by injecting the converted electrical signal into the MZ-IM through an electrical amplifier. Figures 4.8 (a) and (b) depict the spectrum of the MLD and the corresponding RF spectrum of the OEO. The FSR is obtained from the RF spectrum as 6.5 GHz which corresponds to the intermodal separation of 0.58 nm. It can be seen from the results and Eq. (2.35) that the intermodal separation is the key parameter for adjusting the FSR.

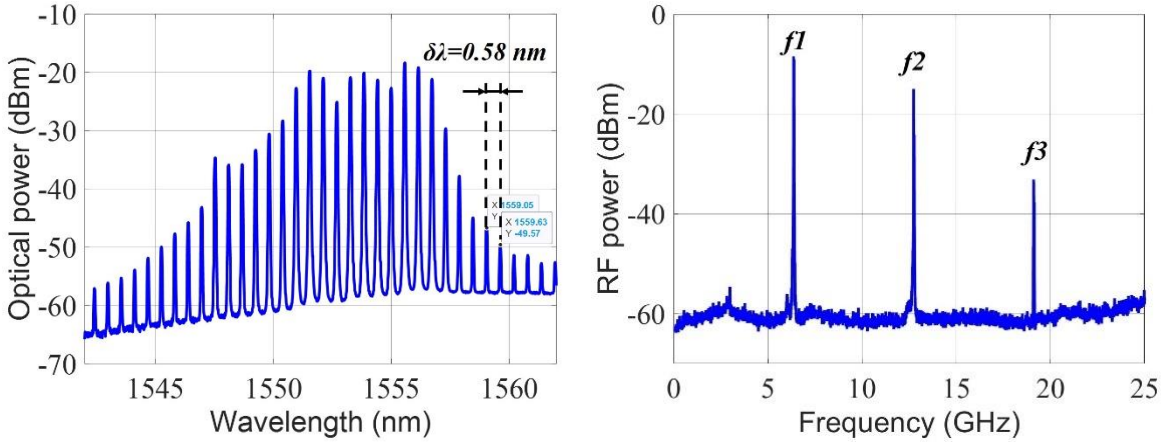

(a) (b)

Figure 4.8 (a) Spectrum of the Fabry-Perot laser diode. (b) Generated RF spectrum of the OEO.

In summary, the generation of a series of stable and highly pure microwave signals through an OEO using a discrete MLD has been successfully demonstrated. Two alternatives of the OEO loop arrangement using direct RF and optoelectronic feedback were presented. In both arrangements, the aim for generating oscillations was excellently achieved.

4.3 Tuneable optoelectronic oscillator

In this section, the OEO using a tuneable multimode source is demonstrated. Firstly, the operation principle and the result in the implementation of a multimode source with capabilities of tuneability are shown. Secondly, this multimode source is used in an OEO setup to achieve the tuneability of the generated microwave signal.

4.3.1 Implementation of a tuneable multimode source

As stated in section 2.2.4, the oscillation frequency and the passband of the MPF depend on the intermodal separation ($\delta\lambda$). Therefore, in order to tune the frequency, the intermodal separation must be modified. In this work, the tuneability of the OEO is achieved using a novel configuration that allows the generation of a multimode optical spectrum using two DFB lasers and an SOA. One of the lasers is discrete while the other one is tuneable. Therefore, we are going to see first the tuneable multimode source of which the setup is illustrated in Fig. 4.9. The generation of a multimode emission is supported by the FWM (Four-Wave Mixing) effect appearing in the SOA.

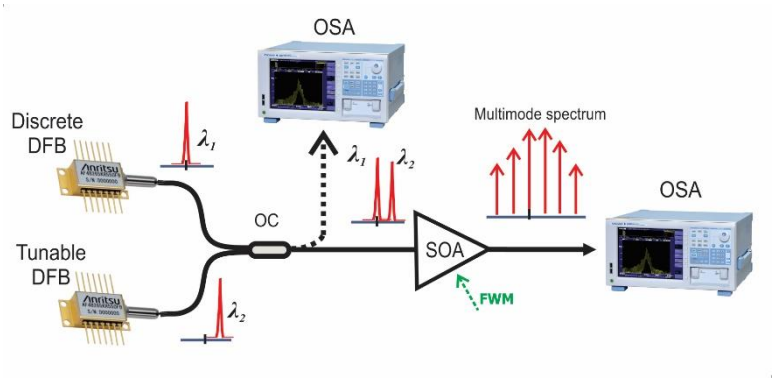

Figure 4.9 Experimental setup used to build a multimode optical source.

Two DFB modules (Anritsu MU952501A) mounted on driver equipment (Anritsu MT9810A Optical Test Set) are used. One DFB is fixed at the wavelength λ_1 = 1550.60 nm whereas the other is a tuneable DFB whose centre wavelength (λ_2) varies in the interval from 1549.70 nm to 1550.20 nm by means of the temperature. An optical spectrum composed of two modes is shown in Fig. 4.10 and the difference $|\lambda_1 - \lambda_2|$ goes from 0.40 nm to 0.90 nm. This optical spectrum is visualized by using an OSA at the output of the optical coupler (OC, 50:50).

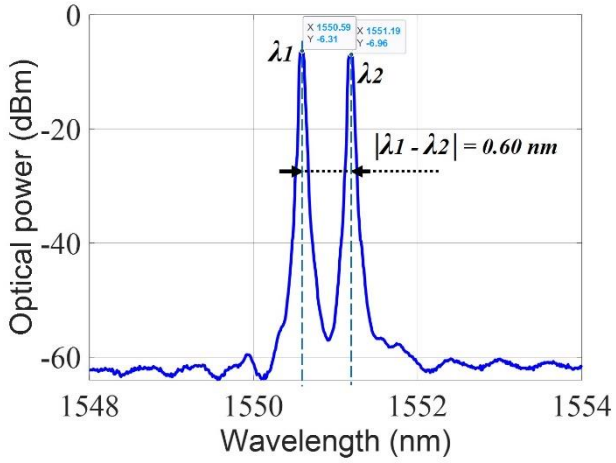

Figure 4.10 Combined light at the output of the optical coupler.

This optical signal is injected into the SOA (Alcatel 1901) driven by current and temperature controllers at 150 mA and 25^{0}C, respectively. At the output of the SOA, thanks to the FWM mechanism, a multimode optical spectrum characterized by a particular intermodal separation ($\delta\lambda$) is generated. The $\delta\lambda$ parameter can be adjusted in function of wavelength (λ_2) of the tuneable DFB. Figures 4.11 (a) and (b) show the multimode optical spectra that correspond to $|\lambda_1 - \lambda_2|$ = 0.90 ($\delta\lambda$ = 0.90 nm), and $|\lambda_1 - \lambda_2|$ = 0.40 nm ($\delta\lambda$ = 0.40 nm), respectively. Each optical spectrum exhibits a Gaussian envelope.

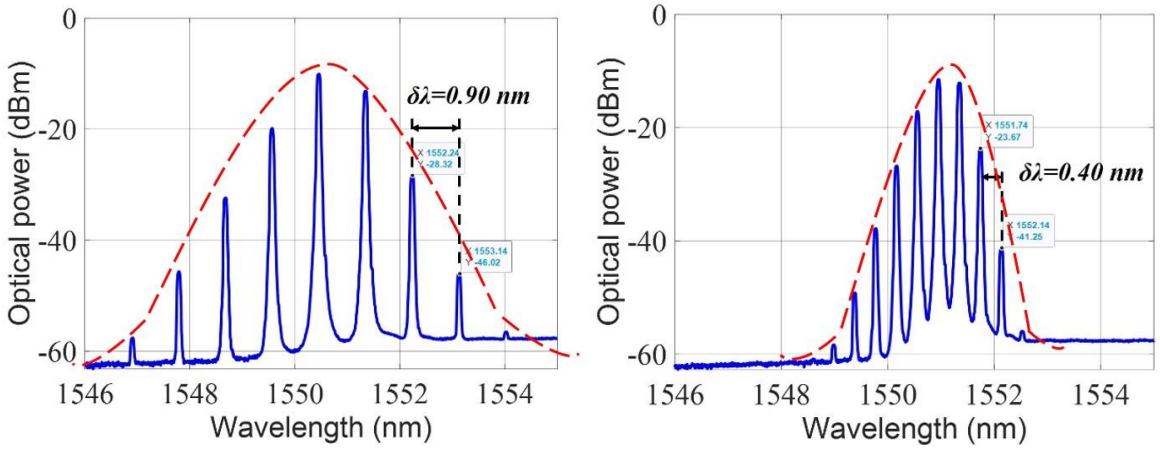

(a) (b)

Figure 4.11 Generated multimode spectra at (a) λ_2 = 1549.70 nm, (b) λ_2 = 1550.20 nm.

In summary, the generation of a multimode optical spectrum whose intermodal separation ($\delta\lambda$) can be tailored by adjusting λ_2, has been successfully demonstrated. This characteristic will be used for obtaining the tuneability of the OEO.

4.3.2 Tuneable optoelectronic oscillator

Figure 4.12 depicts the setup of the OEO where the discrete MLD is replaced by the implemented multimode emission source (arrangement enclosed in the dotted box) in order to demonstrate the tuneability of the OEO.

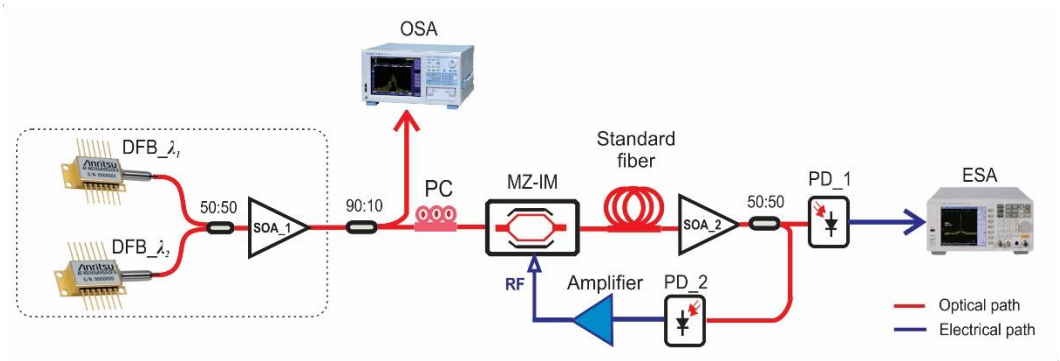

Figure 4.12 Experimental setup of the tuneable optoelectronic oscillator.

The setup is fully automated using the GPIB protocol between the PC and the equipment in order to draw spectrum maps. Figure 4.13 shows the interface to control the lasers and take readings of spectra from the OSA and ESA automatically. The wavelength λ_2 is varied from 193.39 THz (1550.19 nm) to 193.45 THz (1549.71 nm) at steps of 0.001 THz (299.79 nm). The delay time for tuning is set to 4 s. This automated interface allows the establishment of spectrum maps from the generated optical and electrical spectra.

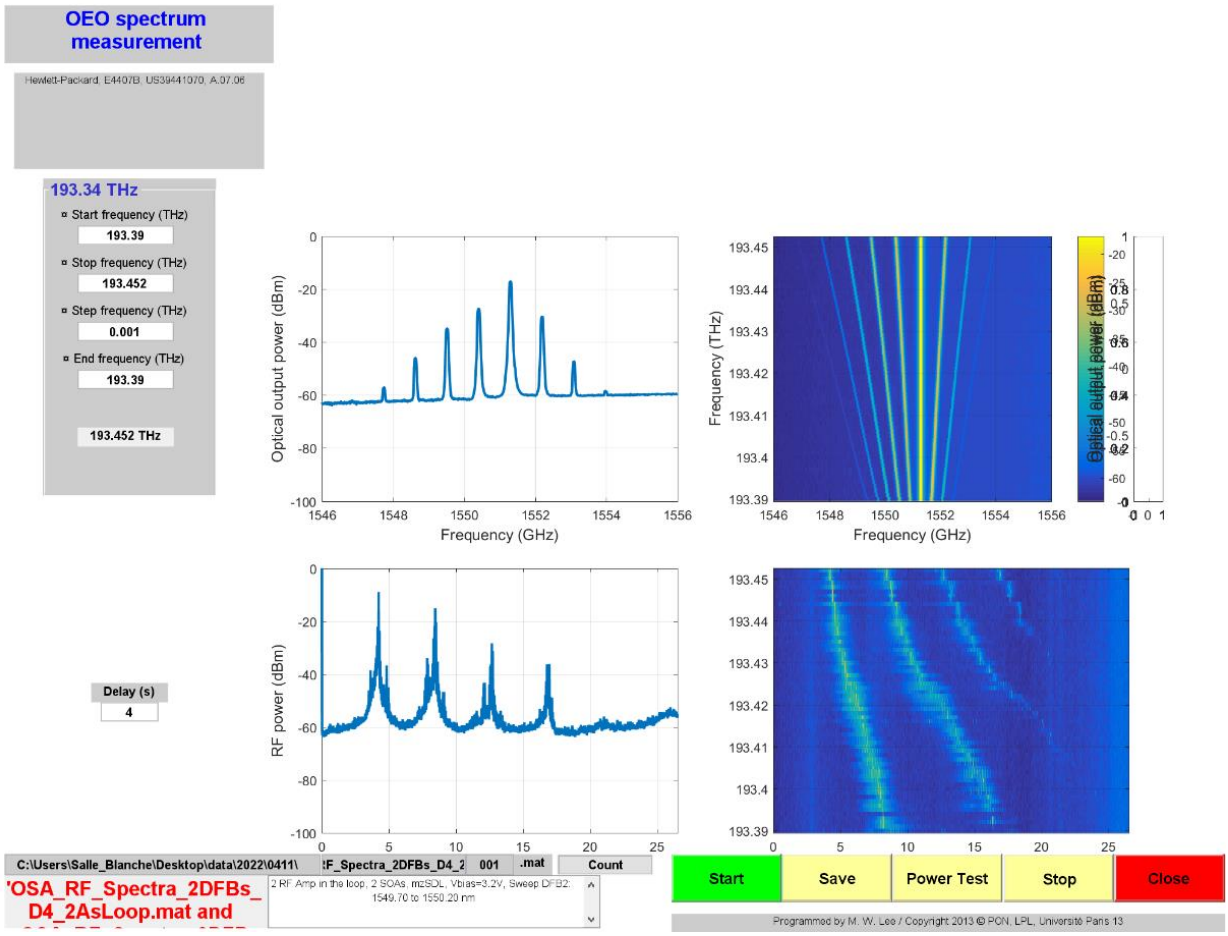

Figure 4.13 Interface of the automated setup.

Figures 4.14 (a) and (b) show optical spectrum and RF spectrum maps. We can see clearly from the maps the gradual variation of the intermodal separation of the optical spectrum and the tuning of the FSR of the RF spectrum. It is also noticed that the FSR decreases as increasing the intermodal separation as expected from Eq. (2.34). Respectively, the FSR varies from 8.35 to 3.87 GHz, when $\delta\lambda$ goes from 0.40 to 0.90 nm. The results show a clear demonstration of the tuneability of our OEO implementing a new multimode source.

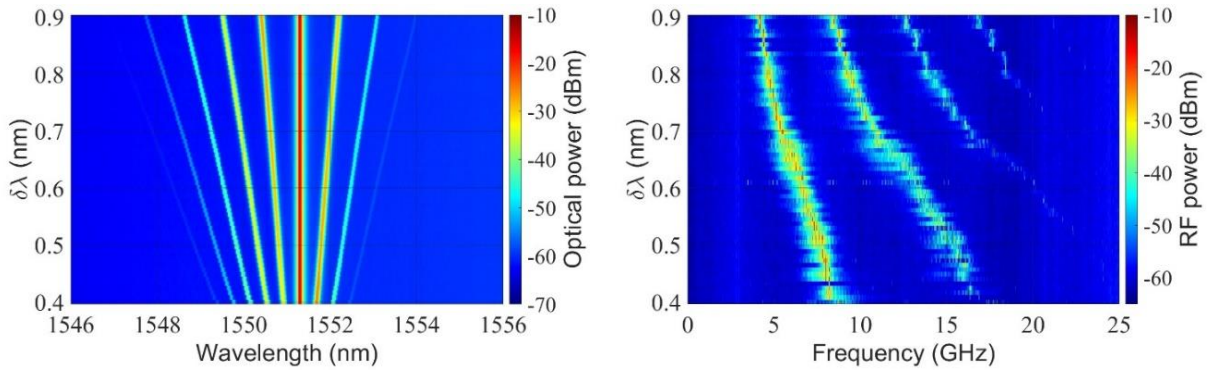

(a) (b)

Figure 4.14 (a) Optical spectrum map of the OEO varying $\delta\lambda$ from 0.40 nm to 0.90 nm, (b) RF spectrum map displaying the RF signal tuning according to $\delta\lambda$ variation.

In order to compare the results to those obtained using an MLD, the wavelength difference between the two DFB lasers is set to 0.60 nm. The newly-implemented source in turn produces a multimode emission of which the intermodal separation is similar to the one of the MLD ($\delta\lambda$ = 0.58 nm). Figures 4.15 (a) and (b) exhibit at $\delta\lambda$ = 0.60 nm the optical spectrum of the implemented multimode source and the electrical spectrum of the OEO, respectively. The FSR is measured as 6.39 GHz and the frequencies f_1, f_2, and f_3 are obtained as 6.41 GHz, 12.8 GHz, and 19.19 GHz, respectively.

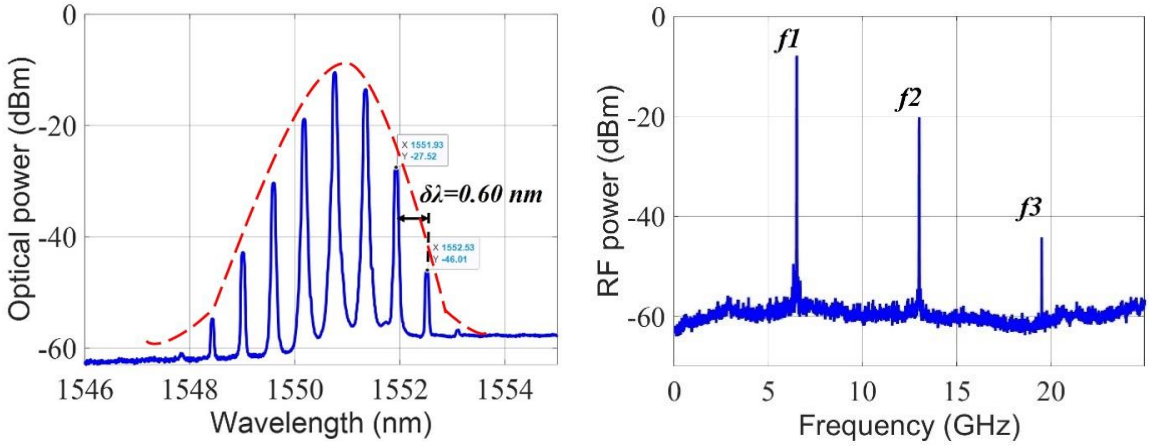

(a) (b)

Figure 4.15 (a) Optical spectrum of the new multimode source, (b) Generated RF spectrum.

It is seen that Figures 4.8 (b) and 4.15 (b) are similar to each other. Despite the available bandwidth of the photodiodes (12 GHz), a third oscillation signal still appears with a reduced power. The results are compared to the ones using the MLD in Table 4.3.

Table 4.3 Comparison of the obtained microwave signals.

OEO	f_1 (GHz)	f_2 (GHz)	f_3 (GHz)	FSR (GHz)	SNR_f_1 (dBm)
MLD	6.36	12.73	19.10	6.37	68
2DFBs-SOA	6.41	12.80	19.19	6.39	65

As seen in the table, the results from both the OEOs are very similar. This is a clear demonstration that our tuneable OEO operates like the one using the MLD.

In order to increase the RF output power of the OEO, the SOA and SOA_2 respectively in Figs. 4.7 and 4.12, are replaced by an Erbium-Doped Fibre Amplifier (EDFA) which has a higher gain and power. The first oscillations of the OEO driven by the conventional MLD and the implemented multimode source are registered, exhibiting powers of 11.93 dBm and 11.42 dBm as shown in Figs. 4.16 (a) and (b), respectively.

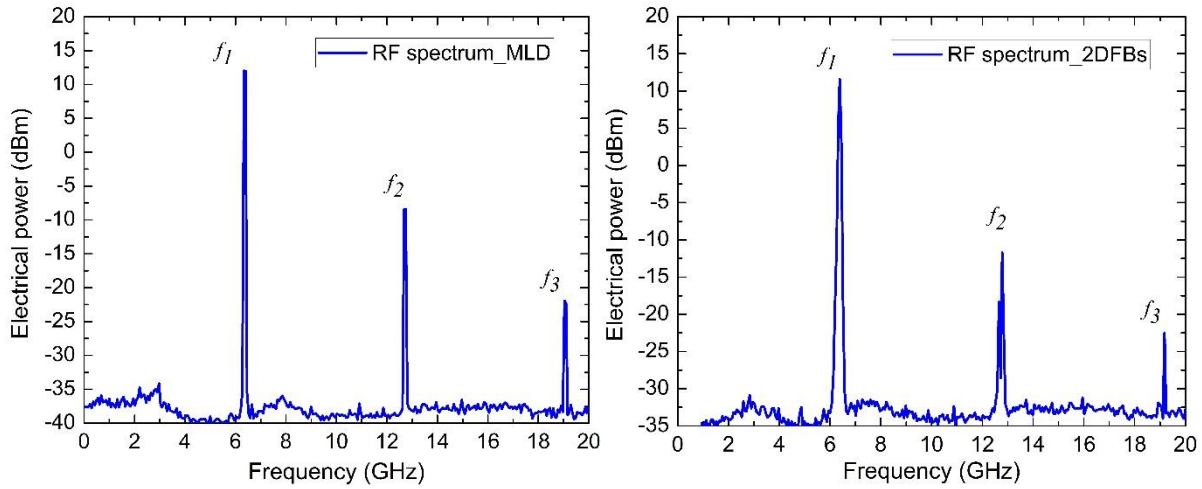

(a) (b)

Figure 4.16 OEO RF spectra using (a) the MLD, and (b) the implemented source.

One of the figures of merit of an OEO is the phase noise. We have measured the phase noise of the OEO using the procedure indicated in section 4.2.2. In this case, the used ESA (Agilent E4407) provides an RBW = 1000 KHz, therefore the normalization parameter is N = 10 log RBW(Hz) = 60 dB. The phase noise power Pn and the phase noise $\mathscr{L}(f)$ are computed respectively by using Eq. (2.37) and Eq. (2.38) at offset points of 10 KHz, 20 KHz, 30 KHz, and 40 KHz. Table 4.4 summarizes these results indicating the measured phase noise values.

Table 4.4 Computed phase noise values for the OEOs

Offset	$\mathscr{L}(f)$ (dBc/Hz)	
	Discrete MLD	**2 DFBs-SOA**
10 KHz	-91.61	-86.55
20 KHz	-97.72	-98.50
30 KHz	-101.99	-101.54
40 KHz	-105.74	-101.86

The obtained phase noise values for both cases are in good agreement and are similar to those reported in the literature [88,89].

In summary, the tuneability of our OEO has successfully been demonstrated. The experimental results are in good agreement with the theoretical values. The comparison of the frequency responses using the discrete MLD and the implemented multimode source reveals good agreement. The phase noise of the tuneable OEO also shows a very good performance.

4.3.3 Summary

In this chapter first, we have demonstrated experimentally the implementation of an MPF and an OEO using a discrete MLD source. The results have been compared to those obtained theoretically and their values are in good agreement. We have also demonstrated successfully the tuneable OEO using two DFB laser diodes and an SOA. The wavelength of one of the laser diodes was shifted by temperature variation through its temperature controller. Thanks to the FWM mechanism in the SOA, a tuneable multimode emission is obtained at the output of the SOA. Tuning the wavelength of that DFB allows the modification of $\delta\lambda$ in the interval from 0.40 nm to 0.90 nm, providing the microwave signal frequency tuning from 3.87 GHz to 8.35 GHz. Again, the experimental results are in good agreement with the theoretical values. In particular, for $\delta\lambda$ = 0.60 nm, the obtained results are again in good agreement with the ones presented using a discrete MLD with the same mode spacing. The phase noise measurement $\mathscr{L}(f)$ allowed to evaluate the system performance and based on published literature, the obtained values in this work are acceptable.

CHAPTER 5: CONCLUSION AND FUTURE WORK

This chapter presents firstly the research synthesis of this thesis work, subsequently, the conclusions obtained from simulated and experimental results, and finally, some suggestions for future work.

5.1 Research Synthesis

Lately, various techniques with interesting results in the implementation of tuneable MPFs and OEOs have been demonstrated. From the considered state of the art, they presented drawbacks such as the use of several devices, complexity of handling, or manual and static tuning. This thesis research is focused on the dynamic tuneability of a multiple bandpass MPF by using novel photonic techniques. The multiple bandpass MPF is composed of a multimode optical source, a Mach Zehnder Intensity Modulator, a long fibre spool, and a photodetector. Its frequency response is composed of multiple bandpass windows that depend on parameters such as the chromatic dispersion (D) and length (L) of the fibre, as well as, the FWHM ($\Delta\lambda$) and intermodal separation ($\delta\lambda$) of the optical source spectrum. Since the first two parameters are pre-established by the manufacturer, we have studied in this work the implementation of two photonic techniques to adjust the intermodal separation of the optical source in order to achieve the dynamic frequency tuning of the MPF. The first technique to obtain the tuneability of the system consisted of using a Fabry Perot Filter (FPF) in order to modify the $\delta\lambda$ parameter of a Multimode Laser Diode (MLD) spectrum. This goal was achieved by varying the Free Spectral Range (FSR) of the FPF which allows changing its selectivity. The second technique is focused on obtaining a multimode spectrum by the use of two Distributed Feedback (DFBs) laser and a Semiconductor Optical Amplifier (SOA). Thanks to FWM process, a multimode emission is obtained at the output of the SOA. In fact, the wavelength difference between the two DFBs corresponds to the intermodal separation of the multimode spectrum. By changing the wavelength of one of the DFBs, the $\delta\lambda$ parameter of the multimode spectrum is modified.

First, we have carried out simulations on the implementation of an MPF with these techniques. The simulations have been performed using VPIphotonics software. As the software lacks libraries for optical multimode sources, we have designed first on the software an MLD by combining

multiple single-mode sources. This newly-designed multimode source is used for other simulations as an MLD.

These techniques have been implemented in the MPF in the simulation for tunning purposes. In the first case, the FSR parameter of the FPF is varied on the software in order to adjust the intermodal separation δλ of the newly-designed MLD. In the second case, the wavelength of one of the DFB lasers is changed in order to modify δλ.

Using both techniques, the tuneability of the MPF system has been validated on the software. In the next step, the MPF response is injected into the modulator, forming a feedback loop that allows the implementation of an OEO. Its frequency is also tuned by the modification of the δλ parameter. It is found that the FSR of the OEO decreases as increasing δλ

After the simulations, the MPF and OEO were implemented experimentally using an MLD emitting at 1553 nm. The laser emission is affected by the dispersion of long fibres (13 km or 50 km). Thanks to the multimode emission and the fibre dispersion, frequency bandpass windows are created at the output of the MPF,

In the case of the second technique, a multimode emission is generated using two DFB lasers and an SOA. By changing the temperature of one of the lasers, we have also demonstrated a tuneable OEO. Besides, we have demonstrated dynamic tunning with frequency tunning mapping by automating the whole experimental setup.

Moreover, the reconfigurability of both the MPF and OEO systems was corroborated by changing the length of the fibre.

5.2 Results

In the following lines, the conclusions of the results obtained from the simulations and experiments are presented.

In the first step, the multiple bandpass MPF has been simulated using a combination of multiple single-mode sources, as well as, a set of two single-mode sources and an SOA, acting as multimode sources.

- From the first approach:

- The combination of multiple single-mode sources allows a well-formed multimode spectrum characterized by a δλ parameter. The multimode spectrum has been successful for the demonstration of the MPF.
- The tuneability of the multiple bandpass MPF is achieved by setting the FSR of the FPF at 90 GHz and 135 GHz, resulting in $\delta\lambda$ = 0.72 nm and $\delta\lambda$ = 1.08 nm, respectively.

- From the second approach:

- The set of two single-mode sources and an SOA allows also the generation of a multimode spectrum with δλ.
- By changing the wavelength of one of the single-mode sources, δλ is modified and consequently, the MPF tuneability was achieved.

In both approaches, the lengths of the optical fibres are 13 km and 50.28 km. These values have been chosen according to the availability of fibres in our laboratory.

In the second step, the MPF and OEO have been implemented experimentally. The MPF is controlled by the discrete MLD, whereas, the OEO is driven by either of the MLD source or a set of two DFBs and an SOA.

- Using the MLD source:

- It has been demonstrated that the MPF creates multiple frequency bandpass windows.
- The OEO has been implemented by forming a feedback loop in the MPF configuration.
- It has been manifested that by maintaining the same parameters (L and δλ), the centre frequencies of the bandpass windows of the MPF correspond to the oscillation frequencies of the OEO.
- With $\delta\lambda$ = 0.60 nm, the frequencies have successfully been generated at 3.49 GHz, 6.99 GHz, and 10.48 GHz using a fibre of 15.95 km.

- Using two DFBs and an SOA as a source:

- Thanks to FWM process put into play in the SOA, the generation of a multimode optical spectrum has been successfully demonstrated.
- The wavelength of one DFB is set to 1550.60 nm, whereas the other is varied from 1550.20 to 1549.70 nm, resulting in δλ from 0.40 to 0.90 nm, respectively.

- The implementation of the OEO driven by this source allows the successful generation of microwave signals. Dynamic tuneability has successfully been demonstrated with frequency tuning mapping thanks to the fully-automated experimental setup. By varying $\delta\lambda$ from 0.40 nm to 0.90 nm, the oscillation frequency is tuned from 8.35 GHz down to 3.87 GHz with a 15.95-km long fibre.
- In the case of $\delta\lambda$ = 0.60 nm, the OEO frequency response is very similar to the one using the MLD. The evaluation of their performances has been carried out by the phase noise measurement established at 10 KHz frequency offset. The phase noise obtained at 6.41 GHz is -86.55 dBc/Hz, which is comparable to -91.68 dBc/Hz obtained at 6.36 GHz using the MLD.

In summary, the system frequency response of the OEO is tuned dynamically using novel photonic technics. The results were presented by gradual tuning maps, demonstrating the efficiency of the system at any minimal variation of δλ. To our knowledge, this is the first work presenting the results in this way. The theoretical, simulated, and experimental results are in good agreement. The relevance of the obtained results reinforces the opinion that this thesis is a promising project in the field of optical communications systems.

5.3 Future work

Despite the interesting results obtained, this thesis project remains open to any suggestion that allows it to be improved or complemented in the future. Some suggestions about it can be:

- To demonstrate experimentally the dynamic tuneability of both the MPF and the OEO using a tuneable FPF device. As shown by simulations, the FPF modifies the MLD parameters and achieves systems tuneability to ensure interesting results with a simple configuration.
- To demonstrate signal transmissions on a bandpass window of the tuneable MPF. This will show the relevance of information selectivity in optical communications systems.
- To improve the performance of the tuneable OEO using a mode-locking technique. In the main configuration, implementing a phase control sub-system will stabilize the generated signals and that will provide a better PN of the system.

- To develop sensor applications of the tuneable OEO. Where the human presence for measurements is dangerous or impossible to accomplish, another alternative will be to achieve remote sensing. A physical element that can somehow modify one of the parameters of the equation. (2.34) will vary the output signal. The calibration of this variation makes possible the quantity measurement of that element.

LIST OF PUBLICATIONS

1) Journal Paper:

Blaise Tshibangu-Mbuebue, Min Won Lee, Roberto Rojas-Laguna, Jorge Rodríguez-Asomoza and Ignacio Enrique Zaldivar-Huerta, "*Numerical Study of a Reconfigurable Multiband Microwave Photonic Filter Using a Tuneable Fabry-Perot Filter*," Electronics 2021, 10(12), 1473. https://doi.org/10.3390/electronics10121473. ISNN: 2079-9292, Impact Factor: 2.397 (According to Journal Citation Reports 2020), Quartile: Q2.

2) Conference articles:

Blaise Tshibangu-Mbuebue, Min Won Lee, Roberto Rojas-Laguna and Ignacio Enrique Zaldivar-Huerta, "*Generating a tuneable multimode optical source from the use of two single-mode sources*," in Frontiers in Optics/Laser Science 2022. 16 to 20 October 2022, Rochester, New York, USA. https://doi.org/10.1364/FIO.2022.JW4A.42

Blaise Tshibangu-Mbuebue, Min Won Lee, Roberto Rojas-Laguna and Ignacio Enrique Zaldivar-Huerta, "*Generation of Microwave Signals by Optical Heterodyning Technique Using a Multimode Laser Diode and a Tuneable DFB Laser*," 2021 IEEE International Conference on Engineering Veracruz (ICEV), 25 to 28 October 2021, pp. 1-5, Veracruz, Mexico. https://ieeexplore.ieee.org/document/9632629

Blaise TSHIBANGU, Ignacio E. ZALDIVAR, Vincent RONCIN, Frédéric DU BURCK et Min Won LEE, "*Démonstration expérimentale d'un oscillateur opto-électronique accordable utilisant un amplificateur optique a semi-conducteur*", the 9ème Congrès de la Société Française d'Optique, 04 - 08 Juillet, 2022, Nice, France. https://www.sfoptique.org/medias/files/posters.pdf

Blaise TSHIBANGU, Min Won LEE, Ignacio E. ZALDIVAR, "*Proposition d'un réglage automatique de filtre micro-onde passe bande via un filtre optique*", 8ème Congrès de la Société Française d'Optique, 05 - 09 Juillet, 2021, Dijon, France.

BIBLIOGRAPHY

[1] Daniel Šmihula, *"Long waves of technological innovations"*, Studia politica Slovaca, 2/2011, Bratislava, ISSN 1337-8163, pp. 50-69.

[2] Schwab, Klaus. "The Fourth Industrial Revolution". Encyclopedia Britannica, 31 May. 2023, https://www.britannica.com/topic/The-Fourth-Industrial-Revolution-2119734. Accessed 27 September 2023.

[3] Bai, Chunguang; Dallasega, Patrick; Orzes, Guido; Sarkis, Joseph, "*Industry 4.0 technologies assessment: A sustainability perspective*," International Journal of Production Economics. 229: 107776, November 2020. DOI:10.1016/j.ijpe.2020.107776

[4] Jain, Rahul, "5G Applications on Various Areas: A Technical Report," March 2023. http://dx.doi.org/10.2139/ssrn.4400114

[5] Khan, Rabia; Kumar, Pardeep; Jayakody, Dush Nalin; Liyanage, Madhusanka "*A Survey on Security and Privacy of 5G Technologies: Potential Solutions, Recent Advancements and Future Directions*," IEEE Communications Surveys & Tutorials, July 2019. DOI:10.1109/COMST.2019.2933899

[6] J. Lytollis, *"Optical Communication Systems a Survey"*, Optics Technology, pp. 1-10, November 1968.

[7] Zmuda H, Toughlian E N, *"Photonic aspects of modern radar"*, Artech House, Inc., 1994.

[8] Li, M.; Hao, T.; Li, W.; Dai, Y. Tutorial on optoelectronic oscillators. APL Photon. 2021, 6, 061101.

[9] Jiang, F.; Wong, J.H.; Lam, H.Q.; Zhou, J.; Aditya, S.; Lim, P.H.; Lee, K.E.K.; Shum, P.P.; Zhang, X. An optically tuneable wideband optoelectronic oscillator based on a bandpass microwave photonic filter. Opt. Express 2013, 21, 16381–16389.

[10] Tang, H.; Yu, Y.; Wang, Z.; Xu, L.; Zhang, X. Wideband tuneable optoelectronic oscillator based on a microwave photonic filter with an ultra-narrow passband. Opt. Lett. 2018, 43, 2328–2331.

[11] Wang, L.; Xiao, X.; Xu, L.; Liu, Y.; Chen, Y.; Yu, Y.; Zhang, X. On-chip tuneable parity-time symmetric optoelectronic oscillator. Adv. Photon. Nexus 2023, 2, 016004.

[12] Hao, T.; Liu, Y.; Tang, J.; Cen, Q.; Li, W.; Zhu, N.; Dai, Y.; Capmany, J.; Yao, J.; Li, M. Recent advances in optoelectronic oscillators. Adv. Photon. 2020, 2, 044001.

[13] Wang, W.; Liu, J.; Sun, W.; Wang, W.; Wang, S.; Zhu, N. Widely tuneable single bandpass microwave photonic filter based on Brillouin-assisted optical carrier recovery. Opt. Express 2014, 22, 29304–29313.

[14] Song, M.; Long, C.; Wu, R.; Seo, D.; Leaird, E.; Weiner, A.M. Reconfigurable and Tuneable Flat-Top Microwave Photonic Filters Utilizing Optical Frequency Combs. IEEE Photon. Technol. Lett. 2011, 23, 1618–1620.

[15] J. Capmany, B. Ortega, D. Pastor, "*A tutorial on microwave photonic filters,*" *Journal of Lightwave Technology*, vol. 24, no. 1, pp. 201-229, Jan. 2006, **DOI:** 10.1109/JLT.2005.860478

[16] Marpaung, D.; Yao, J.; Capmany, J. Integrated microwave photonics. Nat. Photon. 2019, 13, 80–90.

[17] https://www.pcmag.com/encyclopedia/term/55527/fttx

[18] Tim Poulus, "*FTTH networking: Active Ethernet versus Passive Optical Networking and point-to-point vs. point-to-multipoint,*" Telecompaper, November 2010.

[19] K. Zhong, X. Zhou, J. Huo, C. Yu, C. Lu and A. P. T. Lau, "*Digital Signal Processing for Short-Reach Optical Communications: A Review of Current Technologies and Future Trends,*" in *Journal of Lightwave Technology*, vol. 36, no. 2, pp. 377-400, January 2018, **DOI:** 10.1109/JLT.2018.2793881

[20] Y. Zhou, L. Wang, Y. Liu, Y. Yu, X. Zhang, "*Microwave Photonic Filters and Applications,*" *Photonics*, 2023; 10(10):1110. https://doi.org/10.3390/photonics10101110

[21] L. Li, X. Yi, S. Song, SX. Chew, R. Minasian, L. Nguyen, "*Microwave Photonic Signal Processing and Sensing Based on Optical Filtering,*" *Applied Sciences*, 2019; 9(1):163. https://doi.org/10.3390/app9010163

[22] A.J. Seeds, "*Microwave Photonics. Microwave Theory and Techniques,*" IEEE Transactions on Microwave Theory and Techniques, Vol. 50, no. 3, pp. 877 – 887, April 2002, DOI:10.1109/22.989971

[23] J. Yao, *"Microwave Photonics,"* in Journal of Lightwave Technology, vol. 27, no. 3, pp. 314-335, Feb.1, 2009, DOI**:** 10.1109/JLT.2008.2009551.

[24] Bahaa E. A. Saleh, M. C. Teich "Fundamentals of Photonics", John Wiley and Sons, 1991

[25] K. C. Kao and G. A. Hockham, "*Dielectric-fibre surface waveguides for optical frequencies,*" Proc. Inst. Electr. Eng., vol. 133, no. 3, pp. 1151–1158, Jul. 1966.

[26] F. P. Kapron, D. B. Keck, and R. D. Maurer, "Radiation losses in glass optical waveguides," Appl. Phys. Lett., vol. 17, no. 10, pp. 423–425, Nov. 1970

[27] Rongqing Hui, "*Introduction to Fibre-Optic Communications,*" Academic Press, 1st Edition - June 12, 2019, Paperback ISBN: 9780128053454, eBook ISBN: 9780128092347

[28] A.M.J. Koonen, M. García Larrodé, "*Radio-over-MMF Techniques – Part 2: Microwave to Millimeter-Wave Systems,*" J. Lightw.Technol., Vol. 26, No. 15, Aug. 2008, pp. 2396-2408

[29] Khalida Sultana Shuravi, Afia Fairooz, "*Optical Fibre - Dispersion, Construction, Application, Technology, Future,*" March 2016. DOI: 10.13140/RG.2.1.4009.896e1

[30] Bahaa E.A. Saleh and Malvin Carl Teich, "Fundamentals of Photonics," 3rd Edition, Wiley-Interscience, February 2019, ISBN: 9781119506874

[31] A.M.J. Koonen, H.P.A. van den Boom, E. Tangdiongga, H.-D. Jung, P. Guignard, "*Designing In-Building Optical Fibre Networks,*" OSA / OFC/NFOEC, March 2010, DOI:10.1364/NFOEC.2010.JThA46

[32] Roger L. Freeman, *"Telecommunications Transmission Handbook,"* 4th Edition, April 1998, ISBN: 978-0-471-24018-1

[33] William Shieh, Ivan Djordjevic, *"Chapter 3 - Optical Communication Fundamentals,"* OFDM for Optical Communications, Academic Press, 2010, pp. 53-118, ISBN 9780123748799, https://doi.org/10.1016/B978-0-12-374879-9.00003-4.

[34] Gerd Keiser, *"Optical Fibre Communications,"* Third edition, McGraw-Hill, ISBN:0-07-232101-6.

[35] I. H. Malitson, *"Interspecimen Comparison of the Refractive Index of the Fused Silica,"* Journal of the Optical Society of America, Volume 55, number 10, October 1965.

[36] Mingchia Wu and W. I. Way, "Fibre nonlinearity limitations in ultra-dense WDM systems," in Journal of Lightwave Technology, vol. 22, no. 6, pp. 1483-1498, June 2004, DOI**:** 10.1109/JLT.2004.829222

[37] R. Boyed, Nonlinear Optics, Third Edition (New York, 2007).

[38] M. J. Weber, D. Milam, W. L. Smith, "Nonlinear Refractive Index of Glasses and Crystals," Opt. Eng. 17(5) 175463 (1 October 1978) https://doi.org/10.1117/12.7972266

[39] Ramaswami, R., Sivarajan, K., and Sasaki, G., "*Optical Networks: A Practical Perspective*," Third Edition, Elsevier Science, 2009, ISBN 9780080920726

[40] Kasap, S.O., and Sinha, R.K., "Optoelectronics and Photonics: Principles and Practices," International Edition, Pearson, 2012, ISBN: 9780273774174

[41] Rongging Hui, Maurice O'sullivan, "*Fibre-Optic Measurement Techniques,*" Second Edition, 2023, ISBN: 978-0-323-90957-0, DOI: https://doi.org/10.1016/C2020-0-02762-3

[42] L.Chunfei, "Nonlinear Opitcs. Principles and applications," First Edition (Shanghai jiao Tong University Press, 2017).

[43] Mary R. Phillips, Thomas E. Darcie, in Optical Fibre Telecommunications (Third Edition), Volume A, 1997.

[44] J. J. V. Olmos, T. Kuri, and K. Kitayama, "*Reconfigurable Radio-Over-Fibre networks: Multiple-access functionality directly over the optical layer,*" IEEE Trans. Microw. Theory Tech., vol. 58, no. 11, pp. 3001–3010, Nov. 2010.

[45] G. Aguayo, "Analysis and Modeling of an All-Photonic Microwave Filter in the Frequency Range of 0.001-15 GHz," PhD Thesis, INAOE, 2011.

[46] Chengji Lin, Yibei Wang, Yalan Wang, Dangwei Wang, Feng Xiong, Depei Zhang, Jin Zhang, Anle Wang, Pengfei Du, Xiaoniu Peng, **"***Multi-carrier broadband signal generation based on a mutually dual-domain mode-locked optoelectronic oscillator*," Optics Communications, Optics Communications, Volume 529, 2023, 129094, https://doi.org/10.1016/j.optcom.2022.129094

[47] Tongtong Xie, Weiyu Dai, Shichen Zheng, Haoran Wang, Mengyuan Wu, Chaohong Huang, Hongyan Fu, "*A flexibly frequency switchable active mode-locking optoelectronic oscillator with supermode noise suppression*," Optics & Laser Technology, Volume 163, 2023, 109354, https://doi.org/10.1016/j.optlastec.2023.109354

[48] Jianghai Wo, Jin Zhang, Yalan Wang, "*Actively mode-locked optoelectronic oscillator for microwave pulse generation*," Optics & Laser Technology, Volume 146, 2022, 107563, https://doi.org/10.1016/j.optlastec.2021.107563

[49] M. Li, T. Hao, W. Li, Y. Dai, "*Tutorial on optoelectronic oscillators,*" APL Photonics, 6(6), 2021, 061101. https://doi.org/10.1063/5.0050311

[50] Haitao Tang, Yuan Yu, Ziwei Wang, Lu Xu, and Xinliang Zhang,"*Wideband tuneable optoelectronic oscillator based on a microwave photonic filter with an ultra-narrow passband,*" Opt. Lett. 43, 2328-2331 (2018) https://opg.optica.org/ol/abstract.cfm?URI=ol-43-10-2328

[51] Madjar Asher, Berceli Tibor, "Microwave Generation by Optical Techniques - A Review," Proceedings of the 36th European Microwave Conference, EuMC 2006. 1099 – 1102, 2006. DOI:10.1109/EUMC.2006.281126

[52] Tian Cui, Dapeng Liu, Fengyuan Liu, Zhijian Zhang, Zhenzhou Tang, Naidi Cui, Shilong Pan, "*Tuneable optoelectronic oscillator based on a high-Q microring resonator*," Optics Communications, Volume 536, 2023, 129299, https://doi.org/10.1016/j.optcom.2023.129299

[53] https://www.youtube.com/watch?v=hfgaEjf1154

[54] H. Kogelnik and C. V. Shank, "Coupled-wave theory of distributed feedback lasers", J. Appl. Phys.43 (5), 2327 (1972), DOI:10.1063/1.1661499

[55] P. Dekker, M. Ams, T. Calmano, S. Gross, C. Kränkel, G. Huber, and M. J. Withford "Spectral narrowing of Yb:YAG waveguide lasers through hybrid integration with ultrafast laser written Bragg gratings," Optics Express, 23(15):20195-20202, September 2015, DOI:10.1364/OE.23.020195

[56] G. Hernandez, *"Fabry-Perot Interferometers,"* Cambridge University Press, Cambridge, 1988.

[57] El-S. A. El-Badawy, Mohamed H. Mabrouk, *"Tuneable Liquid-Crystal Fabry-Perot Filters for Fibre-Optic and OCDMA Systems,"* the 11th World Multi-conference on systemics, cybernetics, and informatics (WMSCI 2007), Vol. X, pp. 100-105, Orlando, Florida, USA, July 2007.

[58] Herbert Venghaus, *"Wavelength Filters in Fibre Optics,"* Springer, 2006

[59] Nakamura, Kiyoshi, Kurosawa, Yoko, Ishikawa, Kazuo, *"Tuneable Optical Filters Using a LiNbO3 Torsional Actuator with a Fabery-Perot Etalon,"* Applied Physics Letters, vol.68, pp. 2799-2800, May 1996.

[60] N. K. Reay, J. Ring, and R. J. Scaddan, *"A Tuneable Fabry-Perot Filter for the Visible,"* Journal of Physics E, vol 7, August 1974.

[61] N. A. Olsson, "*Lightwave systems with optical amplifiers*", IEEE J. Lightwave Technol. 7 (7), 1071 (1989), DOI:10.1109/50.29634

[62] M. J. Conelly, "*Semiconductor Optical Amplifiers*," Springer, 1st edition., 2002

[63] N.A. Olsson, "*Semiconductor optical amplifiers*," IEEE Proc., 80, 375-382 (1992)

[64] R. Stolen and J. Bjorkholm, "*Parametric amplification and frequency conversion in optical fibres*," in IEEE Journal of Quantum Electronics, vol. 18, no. 7, pp. 1062-1072, July 1982. DOI: 10.1109/JQE.1982.1071660

[65] W. Zhang and J. Yao, "On-chip silicon photonic integrated frequency-tuneable bandpass microwave photonic filter," *Opt. Lett.*, vol. 43, no. 15, pp. 3622–3625, Aug. 2018. https://doi.org/10.1364/OL.43.003622

[66] Hua Shun Wen, Ming Li, Wei Li, and Ning Hua Zhu, "Ultrahigh-Q and tuneable single-passband microwave photonic filter based on stimulated Brillouin scattering and a fibre ring resonator," Opt. Lett. 43, 4659-4662 (2018). https://doi.org/10.1364/OL.43.004659

[67] Liang Huo, Can Zhao, Hao Wu, Ming Tang, *"A Reconfigurable microwave photonic Based on Multicores* Fibres Incorporating a TOAD Switch", Asia Communications and Photonics Conference 2020, ISBN: 978-1-943580-82-8, https://doi.org/10.1364/ACPC.2020.M4A.339

[68] Daniel Nuño, Maria C. Santos, *"Optical phase effects in reconfigurable microwave photonic filters with multiple wavelength input"*, Optics & Laser Technology 143, 2021, https://doi.org/10.1016/j.optlastec.2021.107272

[69] Zhi-yong, Yau, Yu-Gang Shee, Lim Eng-Hock, and Mohd. Adzir Mahdi, "*Wide Tuneability Microwave Photonic Filter Based on Brillouin-Raman Fibre Laser: A Modeling Study*," Proceedings of the Multimedia University Engineering Conference (MECON 2022), pp. 174-182, Atlantis Press, 2022. https://doi.org/10.2991/978-94-6463-082-4_18

[70] W. Zhang and J.Yao, "*Silicon photonic integrated optoelectronic oscillator for frequency-tuneable microwave generation*," *J. Lightw. Technol.*, vol. 36, no. 19, pp. 4655–4663, Oct. 2018. DOI: 10.1109/JLT.2018.2829823

[71] Z. Fan, W. Zhang, Q. Qiu, and J. Yao, "*Hybrid frequency-tuneable parity time-symmetric optoelectronic oscillator*," *J. Lightw. Technol.*, vol. 38, no. 8, pp. 2127–2133, Apr. 2020. DOI: 10.1109/JLT.2019.2962508

[72] Zerong Jia, Jiamin Chen, Yongqiu Zheng, Chen Chen, Liyun Wu, Jiandong Bai, Chenyang Xue, "*High-finesse frequency tuneability of optoelectronic oscillator based on SiO2 optical waveguide ring resonator with the frequency locking technology*," Optics Communications, Volume 498, 2021, https://doi.org/10.1016/j.optcom.2021.127236.

[73] Tian Cui, Dapeng Liu, Fengyuan Liu, Zhijian Zhang, Zhenzhou Tang, Naidi Cui, Shilong Pan, *"Tuneable optoelectronic oscillator based on a high-Q microring resonator,"* Optics Communications, Volume 536, 2023, https://doi.org/10.1016/j.optcom.2023.129299

[74] Leidy Johana Quintero-Rodríguez, Min Won Lee, Jorge Rodríguez-Asomoza, Ignacio Enrique Zaldívar-Huerta, *"Performance improvement of an optoelectronic oscillator by modifying the optical characteristics of a multimode laser diode"*, Optics and Laser Technology 128, 2020, https://doi.org/10.1016/j.optlastec.2020.106263

[75] https://www.analog.com/en/design-center/design-tools-and-calculators/ltspice-simulator.html

[76] https://www.multisim.com/features/

[77] https://www.circuitworkbench.com/

[78] https://optisystem.software.informer.com/

[79] https://www.vpiphotonics.com/index.php

[80] R.E. Shannon, Systems Simulation: The Art and Science, Prentice Hall, New Jersey, 1975

[81] J. P. Goedgebuer, H. Porte, A. Hamel, "*Electrooptic modulation of multi longitudinal mode laser diodes: demonstration at 850 nm with simultaneous data transmission by data coherence multiplexing*," J. Quant. Electron. 23 (7) (July 1987) 1135–1144, https://doi.org/10.1109/JQE.1987.1073476

[82] Farah Diana Mahad, Abu Sahmah M. Supa'at, Sevia Mahdaliza Idrus, David Forsyth, "*Analyses of semiconductor optical amplifier (SOA) four-wave mixing (FWM) for future all-optical wavelength conversion,*" Optik, Vol. 124, Issue 1, 2013, https://doi.org/10.1016/j.ijleo.2011.11.024.

[83] L. A. González-Mondragón, L. J. Quintero-Rodríguez, A. García-Juárez, A. Vera-Marquina, I. E. Zaldívar-Huerta, "*Multiple passband microwave photonic filter with adjustable bandwidth,*" Optics & Laser Technology, Volume 126, 2020, https://doi.org/10.1016/j.optlastec.2020.106133

[84] Tshibangu-Mbuebue, B., Rojas Laguna, R., Lee, M. W., Rodríguez-Asomoza, J., & Zaldívar-Huerta, I. E., "*Numerical Study of a Reconfigurable Multiband Microwave Photonic Filter Using a Tuneable Fabry-Perot Filter,*" *Electronics* 2021, *10*(12), 1473. https://doi.org/10.3390/electronics10121473

[85] G. Aguayo, “Analysis and Modeling of an All-Photonic Microwave Filter in the Frequency Range of 0.001–15 GHz”, PhD Thesis, INAOE, 2011.

[86] ROHDE & SCHWARZ, https://www.youtube.com/watch?v=hfgaEjf1154

[87] S Römisch, J. Kithcing, E. Ferre-Pikal, L. Hollberg, F.L. Walls, “performance evaluation of optoelectronic oscillators”, 1999 Joint Meeting EFTF-IEEE IFCS.

[88] S. Pyshkin, Ed., Optoelectronics - Advanced Materials and Devices. InTech, 2013. doi: 10.5772/3463.

[89] D. Eliyahu, D. Seidel and L. Maleki, "Phase noise of a high performance OEO and an ultra-low noise floor cross-correlation microwave photonic homodyne system," *2008 IEEE International Frequency Control Symposium*, Honolulu, HI, USA, 2008, pp. 811-814, doi: 10.1109/FREQ.2008.4623111.